U. S. Army Research Office grant No. DAAL03-86-K-0175
Los Alamos National Laboratory contract No. 9-XC2X8187-1

# LARGE EDDY SIMULATIONS OF THE ATMOSPHERIC BOUNDARY LAYER EAST OF THE COLORADO ROCKIES

by Keeley R. Costigan



William R. Cotton, P.I.

Colorado State University

# DEPARTMENT OF ATMOSPHERIC SCIENCE

PAPER NO. 511

LARGE EDDY SIMULATIONS OF THE ATMOSPHERIC

BOUNDARY LAYER EAST OF THE COLORADO ROCKIES

by

**Keeley R. Costigan**

Department of Atmospheric Science

Colorado State University

Fort Collins, CO 80523

Research Supported by

**U. S. Army Research Office**

**under Grant grant No. DAAL03-86-K-0175**

and

**Los Alamos National Laboratory**

**under Contract No. 9-XC2X8187-1**

October 22, 1992

Atmospheric Science Paper No. 511

# ABSTRACT


## LARGE EDDY SIMULATIONS OF THE ATMOSPHERIC BOUNDARY LAYER EAST OF THE COLORADO ROCKIES

Large eddy simulation, LES, has often been carried out for the idealized situation of a simple convective boundary layer. Studies of dual Doppler radar and aircraft data from the Phoenix II experiment indicate that the boundary layer of the Colorado High Plains is not a purely convective boundary layer and it is influenced by the mountains to the west. The purpose of this study is to investigate the atmospheric boundary layer on one particular day on the Colorado High Plains. This research applies a LES nested within larger grids, which contain realistic topography and can simulate the larger-scale circulations initiated by the presence of the mountain barrier. How and to what extent the atmospheric boundary layer of the Colorado High Plains is influenced by larger scale circulations and other phenomena associated with the mountain barrier to the west is investigated.

Comparison of the model produced fields and turbulence statistics to the observations of the Phoenix II experiment shows that the nested grid LES reproduces the characteristics of the atmosphere for the case study day reasonably well. Further comparison of the model results to other LES for a purely convective, horizontally homogeneous boundary layer indicates that the mountains influence the atmospheric boundary layer over the plains to the east in several ways. The mountains contribute to the vertical shear of the horizontal winds through the thermally-induced mountain-plains circulation. As a consequence of the wind shear, the boundary layer that develops over the mountains is advected eastward over the top of the plains boundary layer, which is developing separately. This layer is marked by a mixture of gravity waves and turbulence and is atypical of a purely convective boundary layer. Just below this layer, the capping inversion of the plains boundary layer is weak and poorly defined compared to the inversions capping purely convective boundary layers. Gravity waves, triggered by the obstacle of the Rocky Mountains and by convection in the mountain boundary layer, also influence the atmosphere above the Colorado High Plains. These influences are found to have significant effects on the turbulence statistics and the energy spectra.

Keeley R. Costigan
Department of Atmospheric Science
Colorado State University
Fort Collins, Colorado 80523
Fall 1992

ACKNOWLEDGEMENTS

This work was completed with the valuable assistance of many people. I would first like to thank my advisor Dr. William R. Cotton, who introduced me to Large Eddy Simulation and provided support and important guidance in this research. I would also like to thank the other members of my committee, Dr. Roger A. Pielke, Dr. Thomas B. McKee, and Dr. Jane H. Davidson, who contributed helpful insights and edited the manuscript.

I would also like to thank Dr. Douglas Lilly and Dr. Jeanne Schneider for sharing their analysis of the Phoenix II data set. Jeanne's enthusiastic discussions of the atmospheric boundary layer on 22 June 1984 and her encouragement were invaluable.

I am grateful to Dr. Robert Walko for his patient assistance with the RAMS code and its application to LES. Dr. Craig Tremback also answered questions regarding RAMS.

Many helpful discussions with colleagues helped me in this effort. Dr. Mark Hadfield helped me get started using RAMS for LES. Discussions with Dr. Jerome Schmidt, Dr. Michael Weissbluth, Dr. Piotr Flatau, Dr. Tsengdar Lee, Mr. Michael Moran, Dr. Paul Wolyn, Dr. James Bossert, Dr. Jenifer Cram, Dr. Johannes Verlinde, Mr. Jeff Copeland, Dr. Douglas Wesley, and Mr. Michael Meyers contributed to the completions of this work.

I would also like to thank Ms. Brenda Thompson for her work in preparing the manuscript and Ms. Lucy McCall and Ms. Judy Sorbie-Dunn for their drafting and preparation the figures.

This work is dedicated to my family. My husband Steve made many sacrifices so that the work could be completed and gave helpful advice about the presentation of the results. I am very grateful to him and to my daughters Adele and Gwen who also gave in their own way. Other friends and family members have offered encouragement throughout my studies.

This research is supported by the U. S. Army Research Office grant No. DAAL03-86-K-0175 and by Los Alamos National Laboratory contract No 9-XC2X8187-1. Some three dimensional simulations were carried out at the Numerical Aerodynamic Simulation (NAS) Systems Division of the NASA Ames Research Center.

TABLE OF CONTENTS

# Chapter 1

# INTRODUCTION

The Large Eddy Simulation (LES) has been used for two decades to study the atmospheric boundary layer. The use of a numerical model with fine enough resolution to explicitly simulate the largest eddies of the boundary layer was originated by Deardorff (1970, 1974) in the early nineteen seventies. Since that time, LES has contributed much to the understanding of the characteristics and physical processes in the atmospheric boundary layer. Most of the LES's of the past have been used to research the purely convective daytime boundary layer, where winds are light and clear and dry conditions lead to a high surface heat flux. These LES's were initialized with horizontally homogeneous conditions and flat terrain. This is a simple and logical early approach. Several observational data sets have been used for comparison to the LES results, including the Wangara (Clark et al., 1971) and Minnesota (Kaimal et al., 1976) data sets. But, in general, such simplified conditions exist in the real atmosphere only occasionally. More recent studies involving LES have included somewhat more complicated scenarios of horizontally inhomogeneous topography (Walko et al., 1992) or surface heating (Hadfield, 1988; Hadfield et al., 1991 and 1992; Hechtel et al., 1990) and sloping terrain (Schumann, 1990 ).

The purpose of this study is to investigate the atmospheric boundary layer on one particular day on the Colorado High Plains. It is motivated by the desire to apply LES to a real and typical atmospheric situation and by the results of colleagues (Schneider, 1991; Lilly and Schneider, 1990 ) in their analysis of observations of the convective boundary layer near the Boulder Atmospheric Observatory (BAO) from the Phoenix II experiment. Analysis of dual Doppler radar and aircraft data from that experiment indicated that the boundary layer is not a purely convective boundary layer and it is influenced by the mountains to the west.

In addition, Lilly and Mason (1990) performed a LES to make comparisons to the observations of Phoenix II. In order to most closely agree with the observational statistics, they needed to include artificial mean field forcing by adjusting the horizontally-averaged velocity and potential temperature profiles to remain approximately as observed. Their results with these forcings were dramatically different from those obtained with forcing only from surface heating and drag. In their conclusions, they linked the heat source of the Rocky Mountains and the eastward advection of this heat to some of the observed features of the boundary layer.

These results lead to the following questions, which this study will address:

1. How and to what extent is the atmospheric boundary layer of the Colorado high plains influenced by larger scale circulations and other phenomena associated with the mountain barrier to the west? The thermally induced mountain-plains circulation is well documented in this area and gravity waves are also often present. Do they affect the size, shape, position, or strength of the large eddies?

2. How do these influences affect the turbulent statistics of the boundary layer? Are the vertical profiles of heat and momentum fluxes, for example, significantly different from the simple convective boundary layer?

Although these questions are specific to the area of the Phoenix II experiment, the answers to the questions will be relevant to many areas in proximity to mountainous terrain. The answers to these questions will also shed light on the relative efficiency with which the eddies in the boundary layer of the High Plains disperse moisture, aerosols, and pollutants.

For this study, the Regional Atmospheric Modeling System (RAMS), developed at Colorado State University, is employed to investigate the above questions thoroughly. Its two way, interactive, nested-grid capability allows a LES model to be nested within larger grids which contain realistic topography and can simulate the mesoscale circulations. Turbulent statistics similar to other studies are carried out also. The results are then compared to the data collected in the area of the BAO during the Phoenix II boundary layer field experiment and to previous results of other LES studies.

A more in depth background of LES work is presented in Chapter 2. The Phoenix II experiment and results of some analysis of the observations are described in Chapter 3. The RAMS and how it is applied to this research is outlined in Chapter 4. A discussion of the results of two dimensional simulations where the LES grid is contained within two larger grids is given in Chapter 5. This simulation helps to show that the advection of the mountain boundary layer eastward and gravity waves induced by the convection over the mountains play an important role in influencing the large eddies of the plains. The full three dimensional simulation, with three nested grids, is described in Chapter 6, with both the qualitative and statistical results compared to the Phoenix II observations and to LES of purely convective boundary layers. Finally, the results of this study are summarized and suggestions for continuation of this research are given in Chapter 7.

# Chapter 2

# BACKGROUND

As mentioned in the previous chapter, Large Eddy Simulation (LES) has been in use for several decades. It was brought into existence to study the convective boundary layer in closer detail than were possible with prior theoretical studies of the atmosphere. The higher resolution of the LES allows for the actual simulation of the largest eddies of the boundary layer, while the subgrid parameterization still models the energy cascade to smaller scales and dissipation of energy. Also, LES provides simultaneous data in all three spatial dimensions while giving the evolution with time. This chapter presents a brief background on what is known, from both observational and modeling studies, about the convective boundary layer under horizontally homogeneous conditions and non-homogeneous conditions. The reader is referred to Stull (1988) and Caughey (1982) for excellent and more detailed descriptions.

## 2.1 The Horizontally Homogeneous Convective Boundary Layer

Under the conditions of uniform heating of the ground surface and calm winds, the atmospheric boundary layer, above the shallow surface layer, is dominated by convection. The large eddies and the turbulence of this somewhat simplified boundary layer are driven by the convection and the influence of shear is generally neglected. Figure 2.1, from McBean et al. (1979), is a simple schematic diagram of the convective boundary layer under these conditions. The eddies are illustrated in a boundary layer that is well mixed with an overlying, capping inversion which is the transition to the free atmosphere. This inversion is entrained by the large eddies below. Near the surface, are convective plumes and some of these plumes reach to the top of the boundary layer.

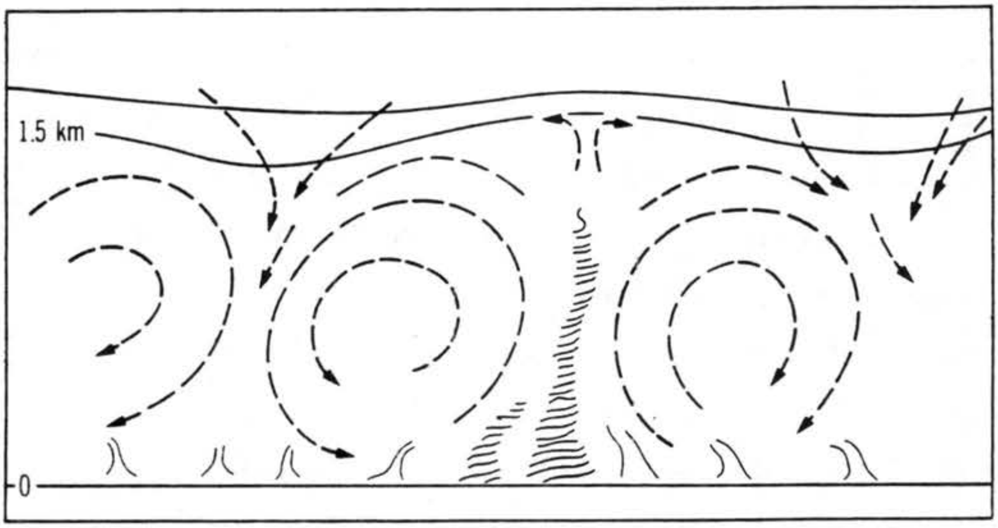


Figure 2.1: A schematic diagram of the structure of the convective boundary layer. From McBean (1979).

Deardorff (1970) introduced mixed layer scaling, which is used to present data from many different observational and numerical experiments in a format where vertical profiles of turbulence statistics can easily be compared. Young (1986) and Stull (1988) discuss the Buckingham Pi theorem of dimensional analysis which contends that when turbulence statistics from different conditions can be nondimensionalized by the controlling parameters, the statistics are functions only of the nondimensional products of the controlling parameters. Mixed layer similarity uses the controlling parameters of $z$ (height), $z_i$ (height of the potential temperature inversion which caps the mixed layer), $\overline{w'\theta'_0}$ (the surface heat flux), and $\frac{g}{\theta_0}$ (where $\theta_0$ is the surface potential temperature). Mixed layer scaling is valid from about 0.1 $z_i$ to the height where entrainment across the capping inversion is important. The scaling parameters in the mixed layer that are generally used are $\frac{z}{z_i}$, $w_* = (\overline{w'\theta'_0} z_i \frac{g}{\theta_0})^{\frac{1}{3}}$ (the convective scaling velocity), $\theta_* = \frac{\overline{w'\theta'_0}}{w_*}$, and $z_i$. Using these scaling parameters will make the turbulence statistics functions only of $\frac{z}{z_i}$. Mixed layer scaling is used in many of the papers discussed below.

### 2.1.1 Observations

Observations of the convective boundary layer include some often sited field studies. These 'classic' observational programs include the Wangara Experiment (Clarke, et al.,

1971) which took place at Hay, New South Wales, Australia in July and August, 1967. The observational data from this experiment included micrometeorological measurements of mast winds, potential temperature, net radiation and heat flux along with pilot balloon winds up to 2 km and radiosonde temperatures and mixing ratios. These data are often used to compare with model predictions of boundary layer development under horizontally homogeneous lower boundary conditions.

The Minnesota experiment was designed to specifically look at the convective elements through the entire depth of the boundary layer. The observations included profile and turbulence sensors mounted on a 32 m tower and probes at five different heights on the tethering cable of a kite balloon. The lower surface was relatively flat and homogeneous and a distinctive inversion marked the top of the boundary layer. Analysis of these data was carried out by Kaimal, et al. (1976) where the data were found to scale well using mixed layer similarity and some of today's generally accepted concepts of the convective boundary layer were presented (see Figure 2.2). From the spectra of velocity components (see Figure 2.3), they found the energy in the inertial subrange to be nearly constant with height and the spectral peaks of the horizontal winds tend to be invariant with height both in their intensities and frequency. The characteristic wavelength of the vertical velocity approaches the same limiting value as the horizontal winds in the upper half of the boundary layer. This characteristic wavelength in the mixed layer was found to be $1.5z_i$ and corresponds to the length scale of the large eddies which typically extend to the top of the boundary layer.

Another measurement program took place at Ashchurch, Worcestershire, England during July 1976. The area near the experiment is not as flat as the area of the Minnesota experiment, with mixed farming and the topography rises to the southeast. Analysis of these data by Caughey and Palmer (1979), however, showed no systematic differences with the Minnesota data due to the different surface characteristics.

Figure 2.4 and figure 2.5 are from Caughey and Palmer (1979) and show the profiles of wind velocity variance and temperature variance using the data of both the Minnesota and Ashchurch experiments, scaled using mixed layer scaling. The vertical

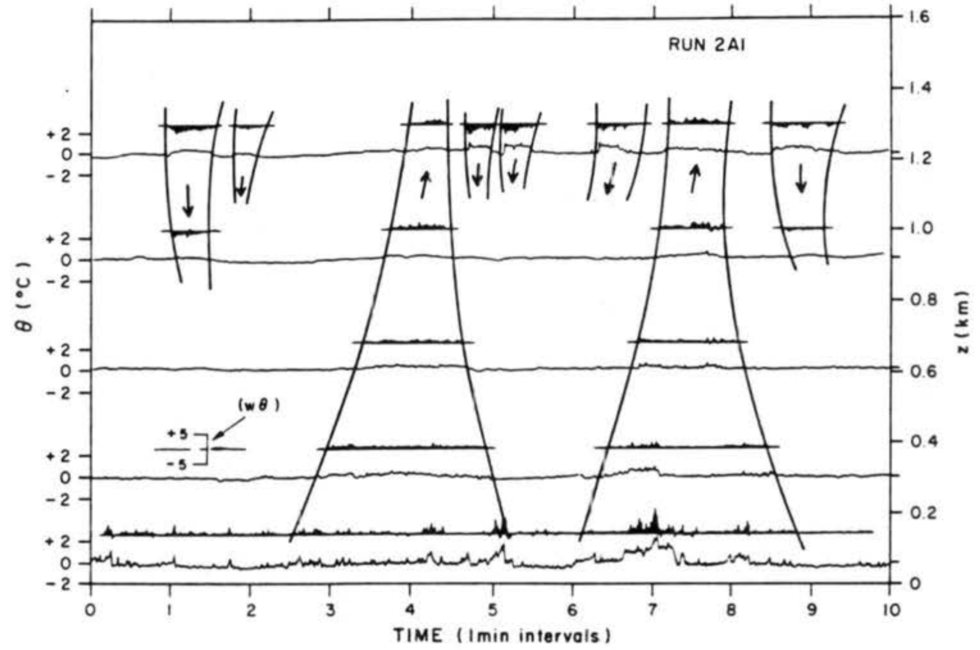


Figure 2.2: Heat flux traces at different heights in the atmospheric boundary layer. The top of the figure represents the inversion base and areas of upward and downward fluxes are marked. From Kaimal et al. (1976).

velocity variance reaches a maximum in the observations of about $0.44w_*$ near $0.5z_i$ to $0.6z_i$ and drops to very small values above the inversion. Horizontal velocity variance also decreases above $z_i$ but not as dramatically as the vertical velocity variance. In the stable air above the inversion, the circulations are more horizontally two dimensional leading to the larger horizontal wind variances compared to vertical wind variances. However, the vertical velocity variance is still non-zero due to entrainment and internal gravity waves, particularly at higher levels. The temperature variance profile shows maximum at the surface, where the heating is strong, and at the inversion. The maximum at the temperature inversion base is associated with entrainment and may be dependent on the strength of the inversion. It therefore cannot be scaled well with $\theta_*^2$.

The convective boundary layer has also been observed using aircraft. These observations are reported in Telford and Warner (1964) , and Lenschow (1970,1974) . Young (1986, 1988) discusses aircraft observations during the original Phoenix experiment over the Colorado High Plains in the fall of 1978. The flight legs analyzed for his study were

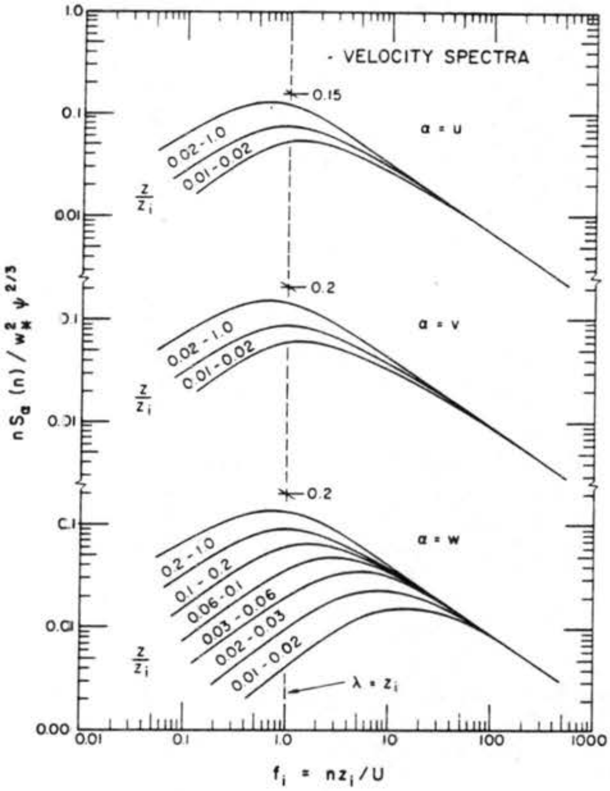


Figure 2.3: Velocity spectra made non-dimensional by using mixed layer scaling. From Kaimal et al. (1976).

all flown in clear skies in scattered cumulus conditions. The wind speeds were light. Intercomparisons of the profiles of turbulence statistics for the entire convective boundary layer from Phoenix 78 and previous experiments indicated that the rolling terrain around the BAO site did not alter the turbulence structure from that observed over more uniform terrain.

### 2.1.2 Laboratory studies

Because the results of the observational studies and model simulations indicate that many occasions exist when the atmospheric boundary layer is in a state of free convection, laboratory studies on the turbulence in the mixed layer were undertaken (Deardorff et al., 1969;; Willis and Deardorff, 1974; and Deardorff and Willis, 1985). The laboratory model provided no mean wind and consisted of penetrative convection of a fluid layer heated from below into an overlying stable region. The fluid used was water and the aspect

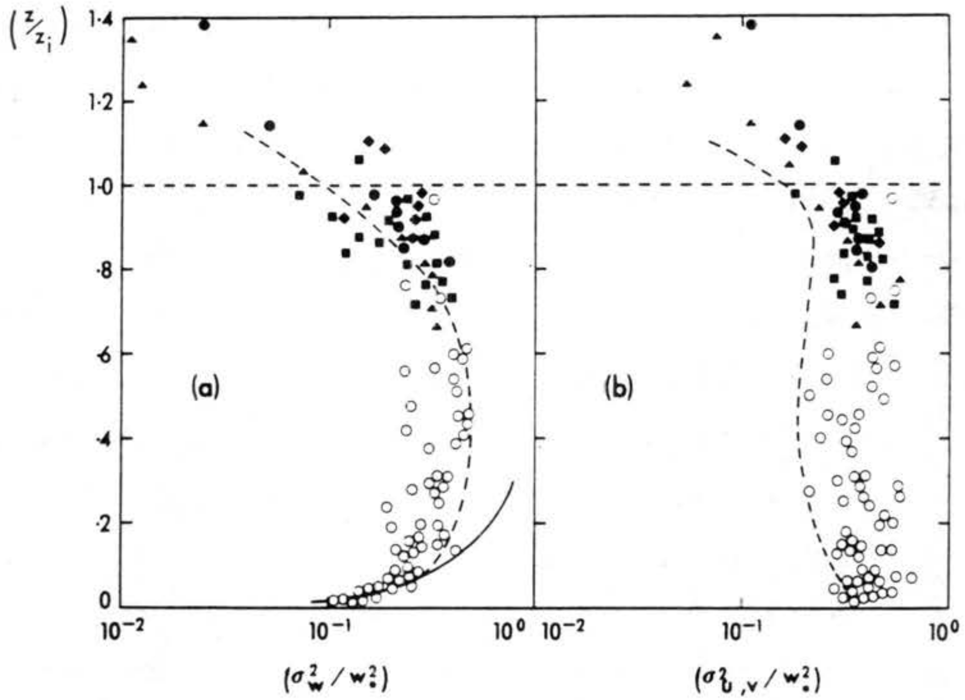


Figure 2.4: Vertical velocity variance (a), and the average of the horizontal velocity variances (b) normalized by $w_*^2$. The solid line is the free convection prediction and the dashed lines represent fluid tank data from Willis and Deardorff (1974). From Caughy and Palmer 1979.

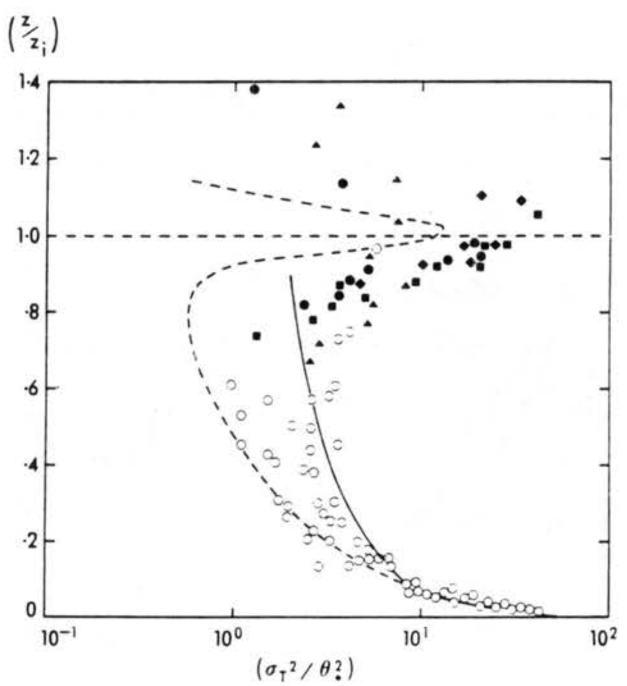


Figure 2.5: Temperature variance normalized by $\theta_*^2$. The solid line is the free convection prediction and the dashed line represent fluid tank data from Willis and Deardorf (1974). From Caughy and Palmer (1979).

ratio of width to height of the convective layer was about 2. The bottom of the fluid was evenly heated to represent the heating of the surface of the atmospheric boundary layer under horizontally homogeneous conditions. Good agreement was found by Willis and Deardorff (1974) in the time evolution of the mean temperature and heat flux profiles between the model measurements and atmospheric observations when the variables were scaled using mixed layer scaling. Caughey and Palmer (1979) compared their field data to the tank data of Willis and Deardorff (1974) and found that the laboratory vertical velocity variance agreed well with the field data but the horizontal velocity variances were too small. The smaller horizontal velocity variances are believed to be due to the small aspect ratio of the tank, which is one limitation of the tank studies. Also, the size of the tank means that the Reynolds number is not very large in the tank experiments (the atmosphere is a high Reynolds number flow) and viscosity will cause the tank flow to be different from the atmospheric flow. The laboratory model is also used for diffusion experiments.

### 2.1.3 Large Eddy Simulations

In the above studies, stationary observing systems were employed to obtain a time series of measurements. With aircraft, a spatial series of the data were obtained. The time series requires the assumptions involved in Taylor's hypothesis to arrive at a concept of the boundary layer. Taylor's hypothesis proposes that turbulence may be thought of as 'frozen' as it advects past a sensor. With this hypothesis, measurements as a function of time can be translated, using the mean wind speed, to their measurements in space. Although data collected from aircraft give a spatial series, all the data points are not collected at the same instant. In arriving at typical characteristics of the boundary layer with this spatial series of data, the assumptions that the boundary layer, as an ensemble of eddies, is steady state over the averaging period of the observations and is relatively homogeneous in the horizontal are made. Numerical model simulations of the boundary layer, using LES, avoid these assumptions by providing three dimensional data at a particular instant in time. Of course, with a LES, the assumption made is that the model adequately represents the physical processes of the atmosphere.

Deardorff in the 1970's began using a numerical model to simulate the atmospheric boundary layer. He used the model to duplicate the observations obtained during the Wangara field experiment. The results of the simulation in Deardorff (1974) compared more favorably to observations than Deardorff (1972) because the original simulation had a shallower domain and was not capable of representing the stable layer above the mixed layer and the entrainment processes across that capping inversion. The increased depth also indicated the the momentum flux within most of the mixed layer was determined by the winds just above the top on the mixed layer and the entrainment rate.

Since the time of Deardorff's early work, several models have been employed to carry out LES. The work of Moeng (1984), and Moeng and Wyngaard (1984,1988,1989) uses one of these models. The pseudo-spectral finite-difference model is described in Moeng (1984), where she also compares her results for a simulation of the boundary layer observed during the Wangara experiment to observations and Deardorff's results. By presenting the resolved and subgrid (parameterized) scale heat flux (see Figure 2.6) she shows that the resolvable-scale eddies contain more turbulent energy and transfer more heat than do the subgrid-scale eddies, lending credibility to the LES approach to studying the atmospheric boundary layer.

Mason (1989) performed a series of LES numerical experiments to test the dependence of the results upon the subgrid model, the domain size, and the mesh resolution. Although the gross features of the boundary layer were not sensitive to the details of the simulations, he discusses a number of factors that he considers important. Near the surface, the subgrid diffusivity needed to be larger than normally had been supposed, in order for the vertical velocity skewness ($\frac{\overline{w'w'w'}}{(\overline{w'w'})^{\frac{3}{2}}}$), which indicates the relative amount of area covered by upward or downward motion) to have the correct sign. Previous LES's had predicted negative skewness near the surface that was inconsistent with observations. The observations show a significant positive skewness throughout the depth of the boundary layer, indicating that areas of upward motion are stronger and narrower than areas of weaker downdrafts. He also found that it was important for the domain size and grid spacings to be set appropriately to allow resolution of the main, freely occurring scales of

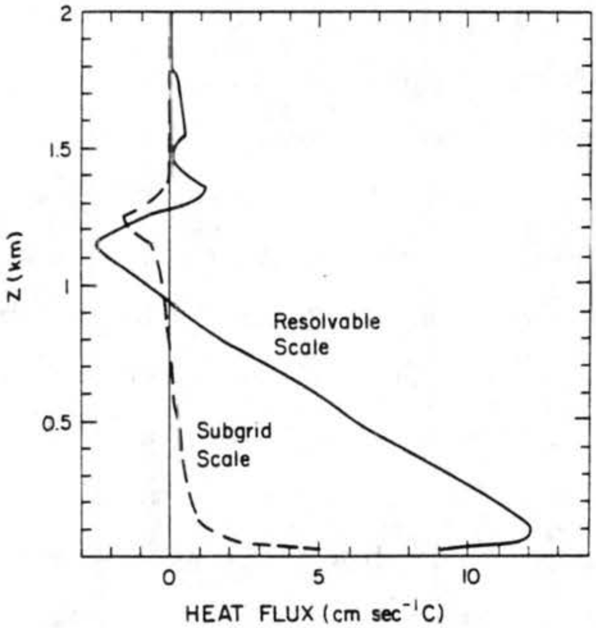


Figure 2.6: Resolved and subgrid scale heat flux of a LES simulation. From Moeng (1984).

motion. His plots of the flow fields indicate that, near the surface, the flow converges into smaller areas of long narrow updrafts. The plumes which penetrate through the depth of the boundary layer to the inversion mainly occur where these long narrow updrafts at the surface intersect.

Schumann et al. (1987) and Schmidt and Schumann (1989) use the MESOSCOP model to carry out LES. Schmidt and Schumann (1989) confirm the findings of Mason (1989) about the structure of the flow field for a horizontally homogeneous convective boundary layer without a mean wind. Figure 2.7 of the instantaneous flow field from their paper shows a spoke pattern in the lower portions of the boundary layer which feeds the large-scale updrafts. The polygonal pattern near the surface is induced by wide downdrafts which suppress upward motions and drive the surface flow radially away from the center of the downdrafts. Warm air tends to flow towards the spikes, then along the spikes towards the hubs of the spoke pattern and then upwards. Large thermals formed within the updrafts penetrate into the stable layer capping the convective boundary layer. Schumann et al. (1989) go on to use the LES to study pollutant diffusion.

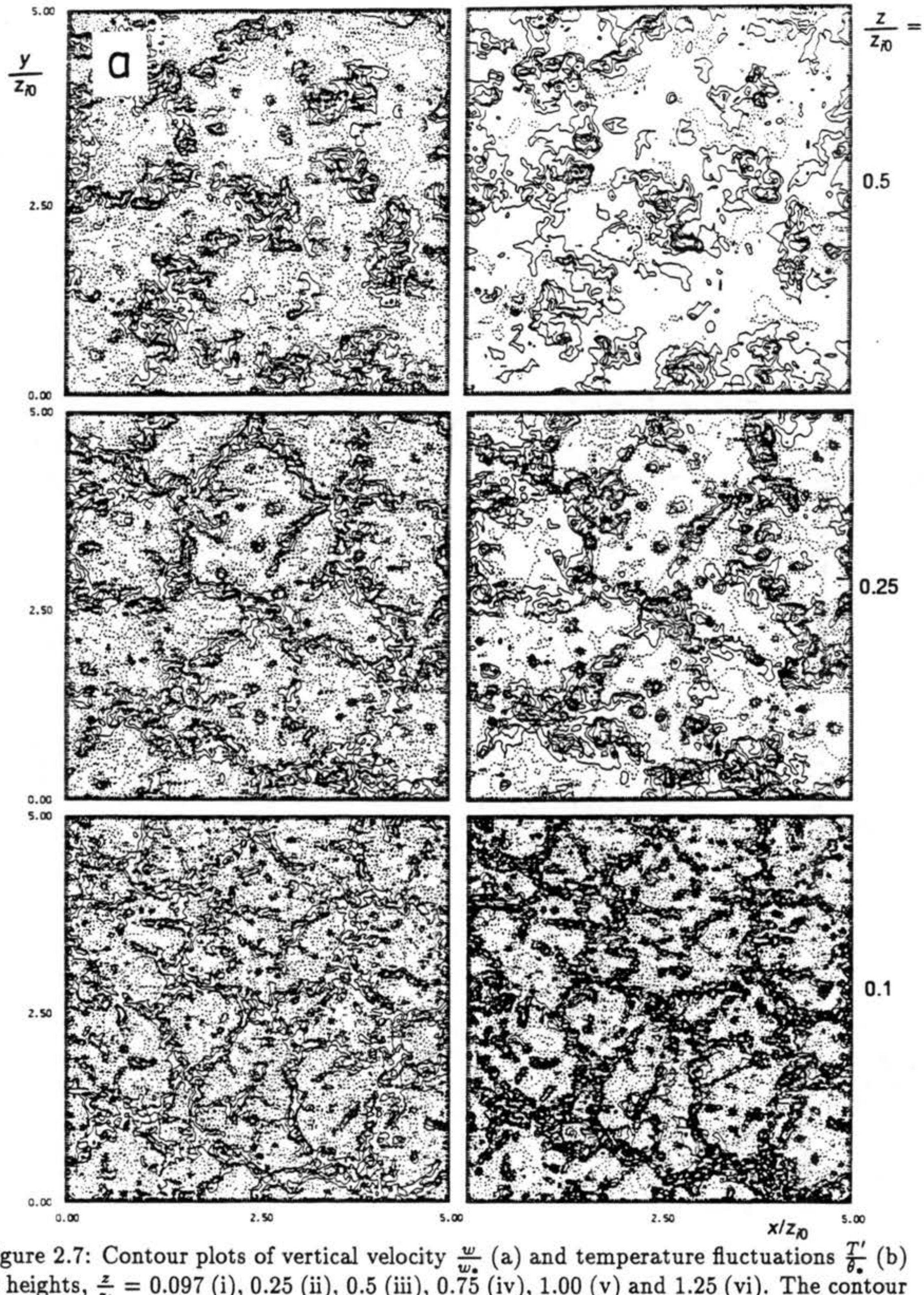


Figure 2.7: Contour plots of vertical velocity $\frac{w}{w_*}$ (a) and temperature fluctuations $\frac{T'}{\theta_*}$ (b) at heights, $\frac{z}{z_i}$ = 0.097 (i), 0.25 (ii), 0.5 (iii), 0.75 (iv), 1.00 (v) and 1.25 (vi). The contour intervals are 0.4 in (a) and 1.0 in (b) with dashed curves representing negative contour values. From Schmidt and Schumann (1989).

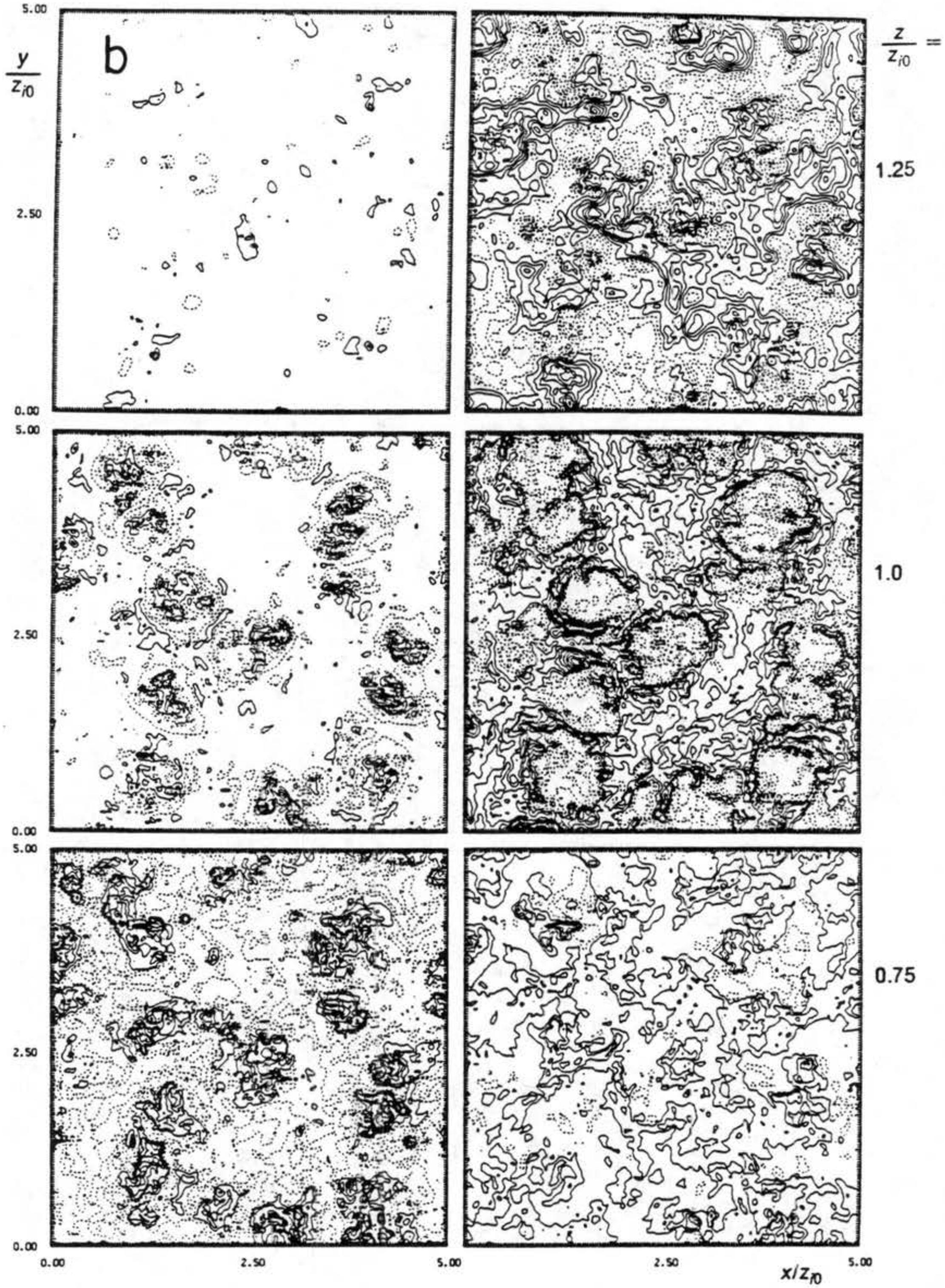


Figure 2.7: Continued.

Nieuwstadt and de Valk (1987) and Van Haren and Nieuwstadt (1989) also use LES to study passive and buoyant plume behavior. Nieuwstadt and Brost (1986) abruptly turn off the surface heating in a LES of the convective boundary layer to study the decay of turbulence. They found that the entrainment process at the capping inversion played an important role in the decay of convective turbulence.

A comparison of the four LES models used by Nieuwstadt, Mason, Moeng, and Schumann is discussed in Nieuwstadt et al. (1991). The purpose of the study was to find out if a large eddy simulation is sensitive to modeling details such as numerical scheme, boundary conditions, and in particular, the subgrid model. The four research groups tested their respective large eddy models on a simulation of the convective boundary layer. Each code is different in many ways. The most important difference between the models was in the subgrid model, where Mason's model had a larger value of $C_s$. In other words, his mixing length is larger with respect to the grid spacing, giving more filtering of variance at higher wave numbers than the other models. Their comparison showed that LES lead to a generally consistent picture of convective turbulence.

## 2.2 The Horizontally Non-Homogeneous Convective Boundary Layer

The horizontally homogeneous convective boundary layer exists only occasionally in the real atmosphere. It would be far beyond the scope of this paper to discuss all the ways the atmospheric boundary layer differs from this idealized situation, but there have been observations of conditions which are relevant to the current case study. Aside from the obvious conditions of strong synoptic influences in the area of the Phoenix II boundary layer experiment, several factors may influence the convective boundary layer in that area. These factors include the effects of topography, wind shear, and gravity waves.

### 2.2.1 Observations

The role of mild topographical variations on the turbulent spectra of the convective boundary layer has been investigated by Kaimal et al. (1982) and Young (1988). Kaimal et al. (1982) looked at Boulder Atmospheric Observatory tower and aircraft observations in the rolling terrain in eastern Colorado. Their analysis of spectra of velocity and temperature from the tower and along wind and crosswind legs of aircraft observations showed few differences with observations over flat uniform terrain. Their analysis involved data from several different days in April with significant winds in the boundary layer. As mentioned earlier, Young (1988) concluded from intercomparisons of the profiles of turbulence statistics from Phoenix 78 and previous field and laboratory experiments that the rolling terrain around the BAO site did not alter the turbulence structure away from that observed over more uniform terrain. The observations were taken in September with light ambient winds.

Grant and Mason (1990) examine observations of turbulence data in an area of complex terrain, where the topography is a series of three valleys that provide a nearly two dimensional ridge-valley system, using instrument packages attached to a balloon tether cable. Non-dimensionalized turbulence data were compared with data obtained over the sea. They also used a numerical model to validate their use of single point observations over complex terrain. The model results indicated that horizontal variations in the turbulence fields were restricted to levels close to the top of the hills. The turbulence statistics and spectra obtained from the observations in this area of quasi-periodic topography were found to be very similar to those obtained from data collected over flat homogeneous surfaces.

Topography on larger scales is known to induce mesoscale circulations. Papers by Dirks (1969), Toth and Johnson (1985) , Wolyn (1992), Abbs and Pielke (1986) , and Tripoli and Cotton (1989) document the pressure-induced circulation along the Front Range of the Colorado Rockies as a response to the mountain heat source. Basically, the strong daytime heating on the mountain barrier leads to relatively warmer air over the higher terrain and reduced pressure. This induces an easterly flow near the surface and up the slope. A return flow of westerlies near the ridge top or ambient westerly winds in the atmosphere above the barrier may also be present. There is evidence that elevated mixed layers, originating over the higher terrain and advected in the upper level westerly flow, are linked to this mesoscale circulation (Wilczak and Christian, 1990). Numerical simulations by Arritt and Young (1990) and Wolyn and McKee (1990) collaborate the advection of the upper level mixed layer within the westerlies.

Clark et al. (1986) and Kuettner et al. (1987) describe how convection can be a source of gravity waves. LeMone (1990) gives an explanation for the differences between LES and observations in the skewness profiles. Figure 2.8 from Moeng and Rotunno (1990) illustrates how LES results generally give much higher values of positive skewness in the upper portion of the boundary layer compared to observations. LeMone states that the observations are influenced by gravity waves that have wavelengths on the order of 10 km. The sinusoidal waves have near zero skewness and their inclusion in the observations will lower the observed overall skewness The small domain and periodic boundary conditions in most studies with LES cannot resolve gravity waves of this scale.

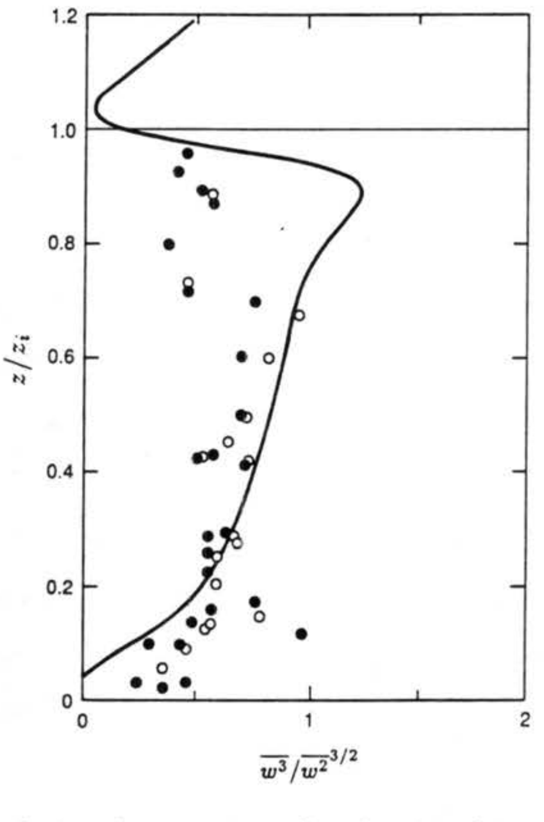


Figure 2.8: The vertical velocity skewness in surface heating driven boundary layers as a function of height. The solid curve is from the large eddy simulation of Moeng and Wyngaard (1988) , and the open circles are from observations of Lenschow et al. (1980) . From Moeng and Rotunno (1990).

### 2.2.2 LES

The Large Eddy Simulation has begun to be applied to conditions which are horizontally non-homogeneous. The models have the advantage of allowing small departures from homogeneous so that the isolated effects of the changes can be studied. Hadfield (1988) and Hadfield et al. (1991,1992) investigated the response of the atmospheric boundary layer to simple sinusoidal variations in surface heat flux. Simulations with no mean winds and with very light mean winds were made. Turbulence was found to be stronger above or downwind of the heat flux maximum, particularly for the wavelength of the surface heat flux variation that was equal to 3.8 times the boundary layer depth. The profiles of horizontally averaged statistics were affected somewhat by the surface heat-flux perturbation but the effects were small and probably would be undetectable in the atmosphere.

Walko et al. (1992) investigated the effects of sinusoidally varying hilly surfaces compared to flat surfaces in LES without mean winds. Thermally direct valley to hill circulations were induced by the uneven terrain and the probability of upward eddy motion increased significantly over the hilltops. The horizontal spectra of vertical motion were strongly biased toward the scales of the terrain. Vertical profiles of the horizontally averaged variables did not show significant differences between hilly and flat terrain surfaces.

Krettenauer and Schumann (1992) also investigated wavy topography in a LES. Their results agree with Walko et al. (1992) . They found that the motion structures are persistent over longer time periods in the presence of irregular topography. Maximum amplitude of the coherent motions in their LES was found for a critical wavelength of the topography of $4z_i$. But the effects of wavy terrain were rather small on the mean turbulence profiles.

The effect of non-homogeneous surface fluxes has been investigated by Hechtel et al. (1990). Instead of sinusoidal variations, quasi-random variations were implemented which were of similar scale and amplitude to those observed near Chickasha, Oklahoma during the Boundary Layer Experiment 1983 (Stull and Eloranta, 1984). A simulation was run and compared with the observations, while a second simulation with homogeneous surface fluxes was also run. They found that the two runs did not show significant differences in the horizontally averaged statistics and speculated that the thermals did not preferentially form over certain surface features due to the presence of a mean wind.

Lilly and Mason (1990) applied Mason's model to the convective boundary layer observed during Phoenix II. As explained in chapter 1, their simulation required mean field forcing of velocity and temperature profiles because the horizontally periodic model domain could not simulate these processes. They found that shear-induced energy generation was important. The large eddy structure of the simulations appeared somewhat chaotic instead of the ring structure of a purely convective boundary layer. They speculated that the tendency to develop downshear rolls conflicted with the tendency to produce cross-shear Kelvin-Helmhotz waves.

Large eddy simulations of free and sheared convective flow between moving flat plates were carried out by Sykes and Henn (1989) . They found that the ratio of friction velocity to the convective velocity scale, $\frac{u_*}{w_*}$, to be a parameter determining the formation of longitudinal rolls in sheared convective flow, instead of the ring structure of the purely convective large eddy field.

Mason (1992) investigated the dispersion characteristics of the atmospheric boundary layer with a series of runs using LES, with a small surface heat flux and different geostrophic wind speeds. He found that the flow fields progress from the characteristic cellular pattern of free convection through organized rolls to irregular, elongated structures typical of a neutral static stability boundary layer as the wind speed is increased. The profiles of vertical velocity variance remained close to free convection values while the friction velocity was less that half the convective velocity scale. The skewness profiles showed a more systematic dependence on the ratio of friction velocity to convective velocity scale, and decreased from free convection values.

# Chapter 3

## DESCRIPTION OF THE PHOENIX II OBSERVATIONAL PROGRAM

One of the motivations for this research is to use LES to study an actual atmospheric boundary layer, not just an idealized one. To allow comparisons to real observations, which will lend credibility to the model results, the scenario for the LES is chosen to coincide with the Phoenix II field operation. A case study is performed for one particular day during the program, where the RAMS model is used for the LES. The following sections describe, in greater detail, the Phoenix II observational program.

The Phoenix II field experiment took place at the time of the summer solstice in 1984 to document the atmospheric boundary layer when the boundary layer experienced strong, positive heat fluxes and was relatively deep. The program was supported by the National Science Foundation, the National Center for Atmospheric Research (NCAR), the Wave Propagation Laboratory of the Environmental Research Laboratories of the National Oceanographic and Atmospheric Administration (NOAA), and the Army Research Office. It took place on the Colorado High Plains approximately 20 km east of Boulder and the Front Range of the Rocky Mountains, in the same area where Phoenix I was held in September, 1978. The immediate surroundings of the observational area are relatively flat. The terrain varies in height by plus or minus 50 m from an average height of about 1600 m above sea level. In general, the area slopes gently toward the South Platte Valley, northeast of the site. The region is agricultural, having alternating ground cover of wheat or other crop fields, fallow strips, and pastures. Some fields are irrigated periodically and there are some ponds, a stream valley, paved roads and a small town. In contrast, the highest portions on the Colorado Rocky Mountains are aligned essentially as a north-south barrier, about 50 km west of the study area. Topography heights reach over 3540 m above sea level there.

The model runs are intended to simulate 22 June 1984, a day with fairly complete observational results and analyzed by Schneider (1991), in the area of the Boulder Atmospheric Observatory (BAO) tower. The weather conditions for that day can be summarized as basically sunny skies with relatively dry conditions and strong solar heating. Schneider (1991) points out that the temperature soundings from aircraft and rawinsonde data lack a well-defined inversion to mark the top of the mixed layer. The mixed layer appeared to lie beneath a transition layer of generally weak to imperceptible static stability and significant shear. Light easterly winds were maintained in the lowest levels while much stronger westerlies were present above the top of the mountain barrier. Cumulus clouds developed over the mountains and advected over the Phoenix area in the afternoon. Their bases were above and apparently had little contact with the mixed layer until downbursts from those clouds extended into the boundary layer in the late afternoon. To simplify the study, this work will focus on the morning and afternoon development of the boundary layer, before the downbursts from clouds affected the boundary layer.

## 3.1 Experimental setup of the observing systems

Much of the focus of the Phoenix II experiment was on measuring the motion fields of the atmospheric boundary layer with Doppler radar. Five Doppler radars were used, two X-band (3 cm), two C-band (5 cm), and one K-band (1 cm). The scanning modes for the X-band and C-band radar pairs were pre-calculated, coordinated, dual volume scans. Clear air reflectivity was enhanced with chaff dispensed by a small aircraft into the boundary layer. Schneider (1991) chose to analyze the data from the NOAA X-band radar pair because the data were relatively free of ground clutter contamination. A schematic diagram, from Schneider (1991), of the Doppler radar placement is given in Figure 3.1. These radars recorded radial velocity, velocity variance of samples within a pulse volume, reflectivity, and a correlation (between pulses) coefficient. Both radars observed a 60 degree segment of space and were centered on the same point. The minimum range recorded was at 4.313 km and the maximum range was 14.841 km and the gate spacing was 0.112 km. The mean volume sampled in each range gate was $\sim (140m)^3$.

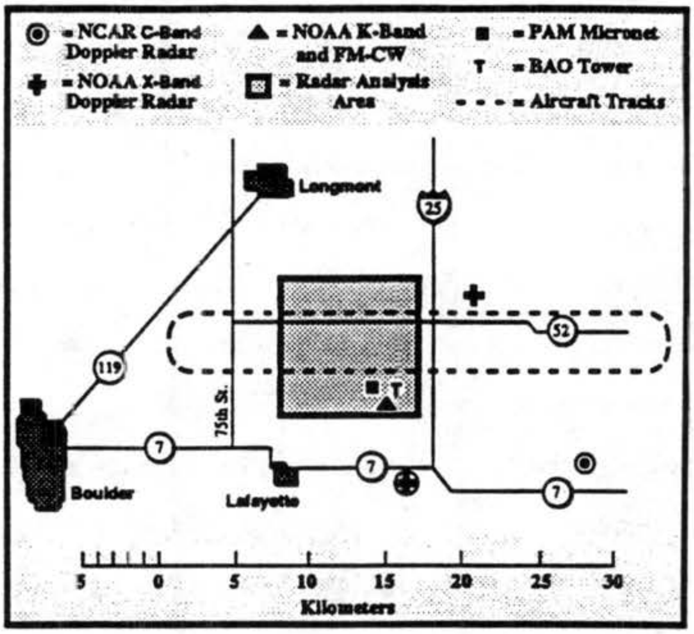


Figure 3.1: Doppler radar configuration for Phoenix II. From Schneider (1991).

The editing of the radar data is described in Schneider (1991) along with the interpolation in space and time and the synthesis between radars. She also discusses the method used to integrate vertical velocity from the radar data. Using $\sim 0.1ms^{-1}$ as an estimate of the accuracy of the radial velocity field and between 0.5 and 20 percent as an estimate of the fraction of radial velocity variance that is noise, she investigates the propagation of error in the derived vertical velocity fields. One of her estimates of error in the values of vertical velocity was an upper bound in accumulated error of 0.5 $\mathrm{ms}^{-1}$ by 3.3 km AGL. She also performed a conservative propagation of error analysis on the vertical velocity variance which indicated the error variance increases almost exponentially above a certain critical elevation angle. The most confidence was thus in the measurements below 2 or 3 km AGL. A thermodynamic recovery technique which produces an approximation to the horizontal perturbation pressure and buoyancy fields was also employed. However, weak fluctuations probably cannot be recovered with this technique.

The radar data were supplemented by observations from several other measurement systems. A diagram of the placement of the measuring systems is given in Figure 3.2. NCAR's King Air instrumented aircraft made flights through the boundary layer. Flight patterns consisted of soundings (flown in a box type pattern) and an east-west racetrack pattern for the horizontal flight legs. Air motion, air velocity, air temperature dew point and relative humidity were measured at a rate of 20 Hz. Surface temperature was measured with a radiometer at a rate of 1 Hz. Further discussion of the aircraft data is given in Lin (1988). He estimates the air velocity measurement errors to be within 0.1 $ms^{-1}$.

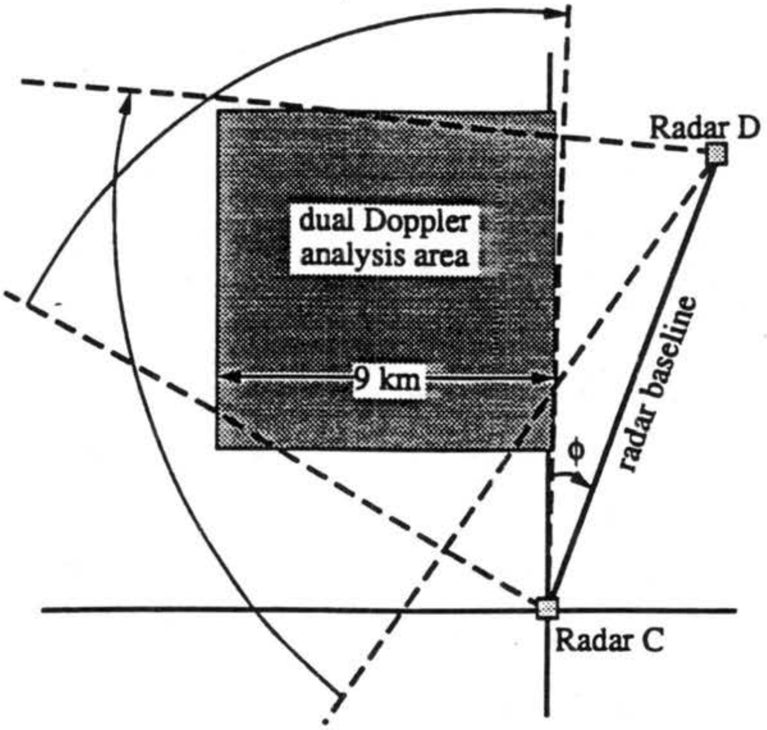


Figure 3.2: Map of the Phoenix II observational site with instrument locations. The radar analysis area refers to the X-band observations. From Schneider (1991).

The program incorporated the Boulder Atmospheric Observatory (BAO) tower in the middle of the study area. The tower had instrumentation at heights of 10, 22, 50, 100, 150, 200, 250, and 300 m. The instruments on booms included a three-axis sonic anemometer, a fast response platinum wire thermometer, a slow response thermometer, a propeller vane anemometer, and a cooled-mirror hygrometer. Additionally, ground instruments located mear the tower included a pyranometer, an absolute pressure sensor, an optical triangle, and microbarographs (Schneider et al., 1984 .

A portable automated mesonet (PAM) network was located about 1.8 km west and 0.5 km north of the BAO tower (see Figure 3.2). The PAM stations recorded pressure, temperature, wet-bulb temperature, rain rate and accumulation, wind speed and direction, and the wind maximum.

Additional data were also available from soundings acquired near the BAO tower from the Atmospheric Instrumentation Research, Inc.'s Automatic Atmospheric Data Acquisition System and Airsonde System. Pressure, temperature, and wet-bulb temperature were measured.

For the purposes of this study, the Doppler radar data were primarily what will be compared to the LES simulations, because the data are available in the three spatial dimensions and in time. The other forms of data are useful for validation of the radar data and the LES results but are not as comprehensive.

## 3.2 Analysis results of observations

Analysis of the Phoenix II data set performed by Schneider (1991) and Lin (1988) indicate that the presence of the Rocky Mountains to the west of the site had a significant effect on the convective boundary layer of the Colorado High Plains during the observational period. They expected to observe a convective boundary layer similar to the idealized convective boundary layers of LES and earlier field studies described in Chapter 2. Their study was complicated by the absence of a sharp capping inversion and the presence instead of a weakly stable layer of mixed turbulence and waves that warmed independently of the local surface heating. There are suggestions that this layer is the result of the advection of the boundary layer that develops over the mountains by the ambient winds (similar to that described in Arritt and Young, 1990 or Wolyn and McKee, 1990).

Vertical shear of the horizontal winds was continuously maintained during the observational period. The presence of shear allows turbulence to be generated by mechanical forcing, sometimes neglected in LES studies, along with the strong buoyant production of turbulent kinetic energy normally found in studies of the convective boundary layer.

Low-level easterlies in conjunction with westerlies above the mountain barrier are commonly observed along the Colorado Front Range and are attributed to the mountain plains circulation that develops as a response to the Rocky Mountain heat source (see Dirks, 1969 and Tripoli and Cotton, 1989).

Their study was further complicated by gravity waves above the locally-generated boundary layer. They speculated that the gravity waves were partially produced by the mountains. Convection in the area may also be a source of gravity waves as in Clark et al. (1986) and Kuettner et al. (1987). LaMone (1990) explores the possible role of gravity waves in influencing the observed boundary layers, giving different skewness profiles in the observations than found in LES.

Associated with these phenomena related to the existence of the mountain barrier up-shear of the site are differences in the turbulent statistics derived from the radar data. One difference already mentioned is the lack of a well defined top to the boundary layer. They also stated that the large eddies themselves are not isotropic but longer in the north-south direction than in the east-west direction, probably due to the observed wind shear. These and other differences will be discussed later as they relate to the results of the current study.

## Chapter 4

# DESCRIPTION OF THE LARGE EDDY SIMULATIONS

The large eddy simulations of this study utilize the Regional Atmospheric Modeling System (RAMS), developed at Colorado State University, configured with fine enough grid spacing to resolve the large eddies of the atmospheric boundary layer. The RAMS model has been proven capable of performing LES in previous studies by Hadfield et al. (1991, 1992) and Walko et al. (1992). Furthermore, Bossert (1990) has adapted the nested-grid version of RAMS to the simulation of the diurnally varying mountain wind systems observed over Colorado. His simulations demonstrated that RAMS is quite capable of realistically simulating both regional and mesoscale circulations over complex terrain. In this study, the mesoscale modeling capabilities of RAMS are combined with its LES capability.

The capability of RAMS to incorporate nested grids makes it particularly suited to carry out a case study of one of the Phoenix II observational days. The LES grid is nested within two larger grids, which have large enough extent to simulate the larger scale flows that influence the real atmospheric boundary layer. The LES is shown to reproduce the general features observed on the case study day. However, the LES is not expected to exactly reproduce the evolution of each of the eddies observed. The emphasis in most LES is on the net effect of a great number (or ensemble) of eddies, rather than the realizations of individual eddies. It is the over-all, ensemble averaged, effects of the larger circulations on the eddies that are considered in this study.

The date chosen for this study is 22 June 1984. This is one of the two days studied in Schneider (1991) and the results are then relatively easily compared to her data analysis. This study will make use of two main simulations. The first simulation is run in two dimensions and is discussed for the general features that are simulated. In two dimensions these features are easier to recognize and can give clues to interpreting the results of the three dimensional simulation. The main emphasis of this research, however, is the three dimensional simulation. The large eddies and turbulence of the atmospheric boundary layer are known to be three dimensional and a three dimensional simulation, which allows stretching and energy to exchange between all three spatial dimensions, is required for a detailed study. Included in the analysis of the three dimensional simulation is a comparison of these results to previous LES studies and observations which are also three dimensional.

A description of the RAMS model and how it is applied to this study follows.

## 4.1 Model Description of RAMS

The Regional Atmospheric Modeling System (RAMS) has continued to be developed after its creation from the merger of a non-hydrostatic cloud model (Tripoli and Cotton, 1980) and a hydrostatic mesoscale model (Maher and Pielke, 1977). A description of earlier versions of these models are given in Tripoli and Cotton (1982), Cotton et al. (1982), Tremback et al (1985), Arritt (1985), McNider (1981), and Tripoli (1986). More recent descriptions of RAMS are given in Tremback (1990), Cram et al. (1992), Bossert (1990), Pielke et al. (1992), and Walko et al. (1992). Basically, the model predicts on ice-liquid water potential temperature $\theta_{il}$, $u$, $v$, and $w$ wind components, perturbation Exner function $\pi = (\frac{p}{p_0})^{\frac{R}{c_p}}$, and mixing ratio, using the primitive equations. The model consists of numerous modules and allows for many possible configurations of features. For the simulations in this study, the model was run as nonhydrostatic and included a terrain following coordinate system (after Clark, 1977). A second order advection scheme is used. A leap-frog time differencing scheme is also employed with time-splitting so that a long time-step can be used for advective processes and a shorter timestep for terms involving the propagation of sound waves. The ratio between the effective speed of sound which the model uses in simulating the propagation of sound waves, and the physical speed of sound was set to 0.26. This was done to allow for a longer timestep and increase the efficiency of the simulation and, according to previous studies (Droegemeier and Wilhelmson, 1985; Tripoli, 1986; and Cotton and Anthes, 1990), has little impact on the meteorological solutions. Hadfield (1988)also reduced the effective speed of sound for his LES simulations and found large computational savings at very little deterioration in model accuracy. The effects of the Coriolis force are included in these simulations.

The parameterization of radiative processes chosen is described in Chen and Cotton (1983). Absorption, scattering, transmission, and emission in the atmosphere are included. Soil temperature and moisture are represented at 11 levels as part of the surface temperature and moisture parameterization of Tremback and Kessler (1985). A surface energy budget is calculated that includes fluxes of shortwave and longwave radiation, latent and sensible heat and conduction to and from the soil. The surface layer is parameterized by the surface layer similarity theory equations specified in Louis (1979).

To reduce the cost of these simulations and because the interest is primarily in the dry circulations of the boundary layer, the model option to treat water vapor as a passive tracer was chosen. Thus condensation and clouds are not modeled in these simulations and the only source or sink of atmospheric moisture is at the soil surface, due to evaporation or dew formation. The simulations make use of the two way interactive nested grids. The scheme for grid nesting in RAMS follows Clark and Farley (1984).

### 4.2 Grid Configurations

Both of the simulations require the use of three nested grids. Figure 4.1 is a schematic diagram of the grid structure of three grids nested, where the grid spacing decreases by a factor of four with successively smaller grids. This schematic figure also shows the vertical grid spacing in the shaded area. Figure 4.2 illustrates the actual locations of the grids used for this study. The smallest grid is the LES. Its western boundary is located just west of the Colorado Front Range of the Rocky Mountains and it extends eastward for more than 46 km, well on to the Great Plains, and includes the site of the Phoenix II boundary layer experiment. The horizontal grid spacing on the LES grid is 191.25 m and the number of grid points in the east-west direction is 242. This resolution is somewhat coarse for LES, which typically have 50 to 100 m grid spacing. But it can be justified by the deep boundary layer (Schneider, 1991) and larger than typical eddies on this day near the summer solstice. Some might call this a 'very large eddy simulation'. The long timestep on this grid is 3 seconds.

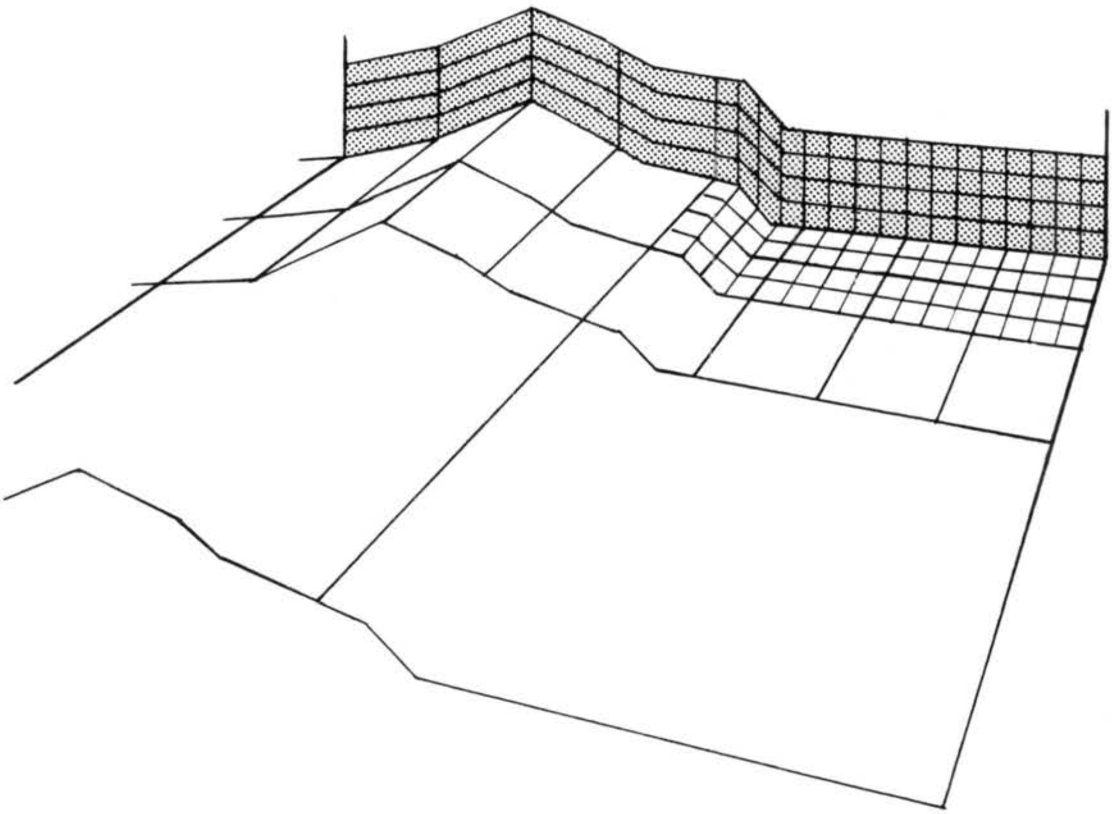

Figure 4.1: Illustration of the nested configuration of the three model grids.

The middle-sized grid begins west of the continental divide and reaches eastward just beyond the LES grid. This grid is large enough to capture the larger scale flows associated with the topography of the Front Range. The horizontal grid spacing is 765 m and the number of grid points is 134. The long timestep on the middle grid is 12 seconds. The topography for this grid and the LES grid was obtained from 30 sec data and was interpolated to the grids using the silhouette averaging scheme described by Bossert (1990) . This type of averaging allows for the maintenance of the barrier height while preserving the mass of the topography.

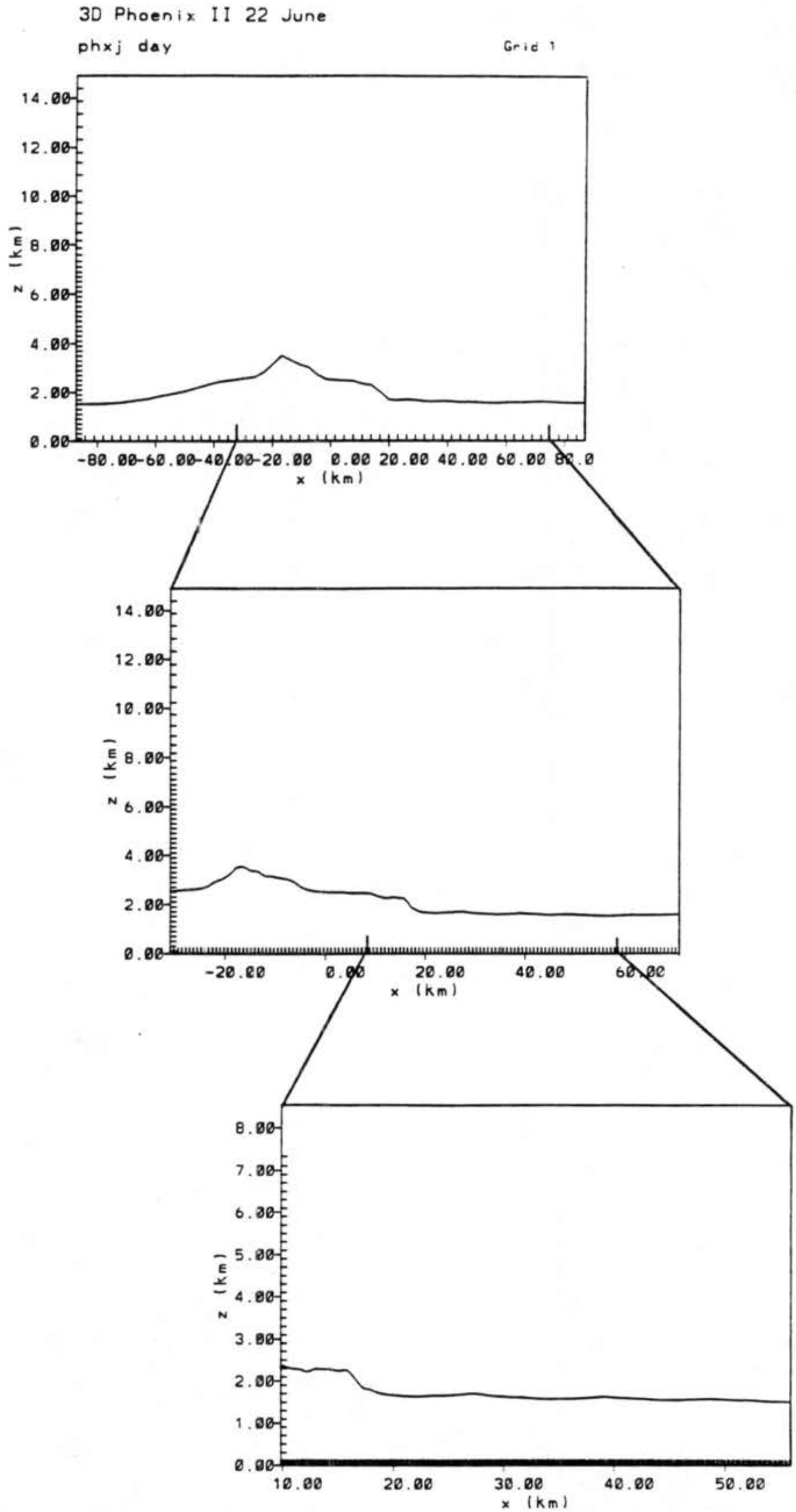


Figure 4.2: Illustration of the nested configuration of the three model grids.

The largest grid was included in the simulation to avoid problems on the lateral boundaries of the smaller grids. It extends over 177 km westward of the middle grid and eastward to include the two smaller grids. The grid has 58 grid points in the east-west direction, spaced 3060 m apart. The long timestep on this grid is 24 seconds with the ratio of long to short timestep on all the grids being 6. The topography for this grid was averaged from the middle grid topography where it coincided with the middle grid. West of there the topography is fictitious and was designed to bring the topography on the western boundary to the same height above sea level as the eastern boundary. The shape of the fictitious western slope somewhat mimics the eastern slope and avoids dramatic changes in slope for convenience. It is desirable to have the topography height the same on both boundaries because the model is initialized horizontally homogeneously and the initial wind profile should reach through the same depth of the domain at both the inflow and outflow boundaries. This avoids anomalous pressure fields associated with the boundaries.

All three grids have the same grid structure in the vertical direction that consist of 55 grid points. Through the lowest 7 km of the atmosphere, a constant grid spacing of 200 m is specified to better facilitate averaging of model results for analysis. Above 7 km the grid is stretched to a maximum grid spacing of 519 m and the top of the grid is over 15 km above the surface.

For the three dimensional simulation, the north-south direction is included. Adding the third dimension makes the simulations very computationally expensive and, in an effort to control these costs, a type of 'channel' simulation is designed. The simulation is like a channel simulation in the sense that the east-west dimension of each of the grids is much greater than the north-south dimension. However, instead of using a wall as a boundary on the north and south, cyclic boundary conditions are used. The idea is that this design allows the eddies to be three dimensional while maintaining a simulation with manageable memory and CPU requirements. The grid spacing used is the same as in the east-west direction with 18 points on the largest grid, 10 points on the middle grid, and 38 points on the LES grid. The topography heights are held constant in the y direction.

### 4.3 Parameterization of Subgrid Turbulent Kinetic Energy

The LES work of Hadfield (1988) and Walko et al. (1992) with RAMS used the Deardorff (1980) one and a half order closure for the parameterization of the subgrid turbulent kinetic energy. This parameterization was developed for some of Deardorff's LES work and proved effective when used for that purpose in RAMS. Unfortunately, the scheme does not apply well to mesoscale simulations which are included in the larger grids of this study because the turbulence scheme on the mesoscale must parameterize the effects of all eddies or be an ensemble-averaged scheme rather than a sub-grid scale scheme. The Mellor and Yamada (1982) Level 2.5 scheme is an ensemble-averaged scheme and has been added to the current RAMS code for these simulations and is used for vertical turbulent transport on the larger grids. A modification of the level 2.5 scheme is used and follows the method proposed by Helfand and Labraga (1988). The modification lets the model run with the level 2 parameterization for growing turbulence and level 2.5 for decaying turbulence. In the horizontal, a first order closer scheme with a deformation based mixing coefficient is used (see Tripoli, 1986). Thus, the Mellor and Yamada scheme is used to predict ensemble average TKE and vertical eddy fluxes on grids one and two, while the Deardorff scheme is used to predict subgrid turbulence transports on grid 3, the LES grid.

Even if the same parameterization were used on all grids, it would not be appropriate to feed subgrid TKE between grids in the same manner as the other variables predicted in the model. What is subgrid scale on one of the larger grids may be resolved on the LES grid with some circulations still being smaller than can be resolved by the LES grid. An example of circulations that are not resolved on the larger grids are the large eddies that are resolved on the LES and the focus of this study. For this research, the communication of subgrid TKE between grids is completely shut off, including no advection into the smaller grids. Two dimensional numerical experiments with this approach indicate that TKE will adjust rather quickly to local conditions in a convective boundary layer only a short distance from the nested boundaries.

### 4.4 Initial and Boundary Conditions

As stated above, these simulations make full use of RAMS nested grid capabilities. This allows circulations to advect into and out of the inner grids. The lateral boundary conditions in the east-west direction thus apply to the largest grid, where a Klemp-Wilhelmson boundary condition is used for the normal velocity and a zero gradient inflow and outflow was assumed for other variables. For the three dimensional simulation, cyclic boundary conditions are applied in the north-south direction on each of the grids. Modifications to the RAMS code were made for the specific grid configurations of this simulation to ensure that the number of overlapping grid points is consistent from one grid to the other.

The top boundary is a wall with a Raleigh friction layer ten grid points deep. The lower boundary conditions are specified by the topography and surface parameterizations described in Section 4.2.

The model is initialized horizontally homogeneously at 0000 UTC (1700 MST) for both the two and three dimensional simulations. At that time, only the two largest grids are initialized and the simulation is run through the night to establish a realistic night time boundary layer by sunrise. At 1200 UTC (0500 MST and near sunrise), the LES grid is added to allow explicit representation of the largest turbulent eddies during the development of the daytime boundary layer.

The initial temperature and moisture profile is taken from the 0000 UTC rawinsonde sounding for 22 June 1984 at Denver. The wind structure used the same sounding but was modified somewhat to agree better with the rawinsonde observed winds at 1200 UTC. Apparently, some large scale forcings, beyond the range of the model domain, had influenced the winds over night. Figure 4.3 shows the initial fields. The potential temperature field indicates a very deep boundary layer that is well mixed, extending beyond 5 km MSL or 3.5 km above the surface of the Great Plains. This is not an unusual observation in this area late on a summer afternoon. The mixing ratio decreases with height, with very little moisture above 6 km MSL. The initial wind field already has wind shear with height that is typical of the mountain plains circulation observed along the Colorado Front Range on summer afternoons. While the light easterly winds of about 2 $ms^{-1}$ at low levels combined with the stronger westerly winds aloft, up to 16 $ms^{-1}$ are common along the Colorado Front Range, the horizontally homogeneous initialization also places the same wind profile over the western slope of the Rockies. The mountain plains circulation on the west side of the barrier would call for low level westerly winds during the day. This points to one of the limitations of the horizontally homogeneous initialization and is the reason the model is allowed to run for 12 hours before the time of interest for this study and the time when the LES grid is added. The model then has time to develop a realistic night time boundary layer throughout the domain.

These conditions are typical of the Phoenix II study area but are substantially different than most LES studies, especially the presence of wind shear.

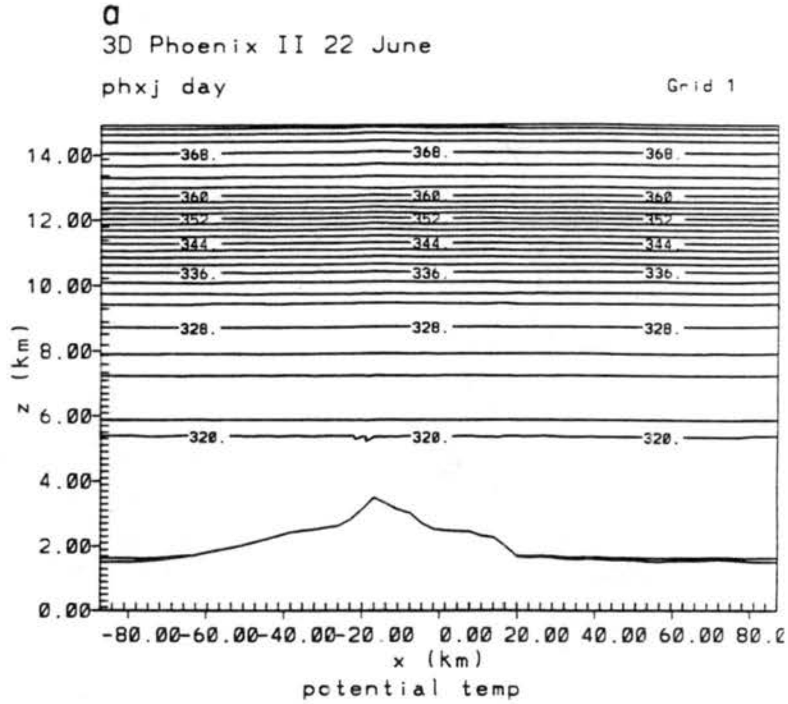


Figure 4.3: Vertical x-z cross sections of potential temperature (a), u-component of the wind (b), v-component of the wind (c), and total water vapor mixing ratio (d) on grid 1 used to initialize the model. The contour intervals are 2.0 K in (a), 2 $ms^{-1}$ in (b), 2 $ms^{-1}$ in (c), and 0.5 $gkg^{-1}$ in (d).

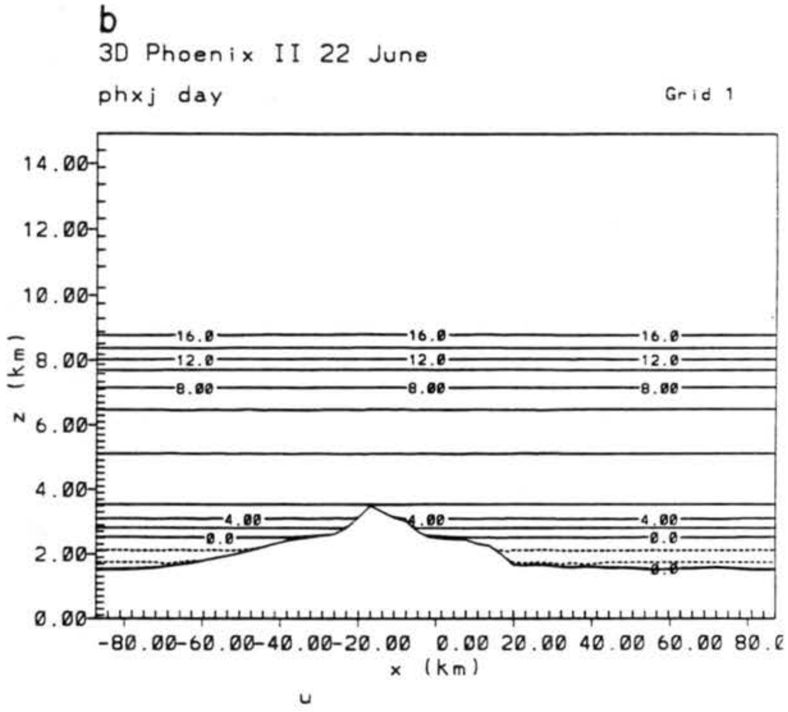


Figure 4.3: Continued.

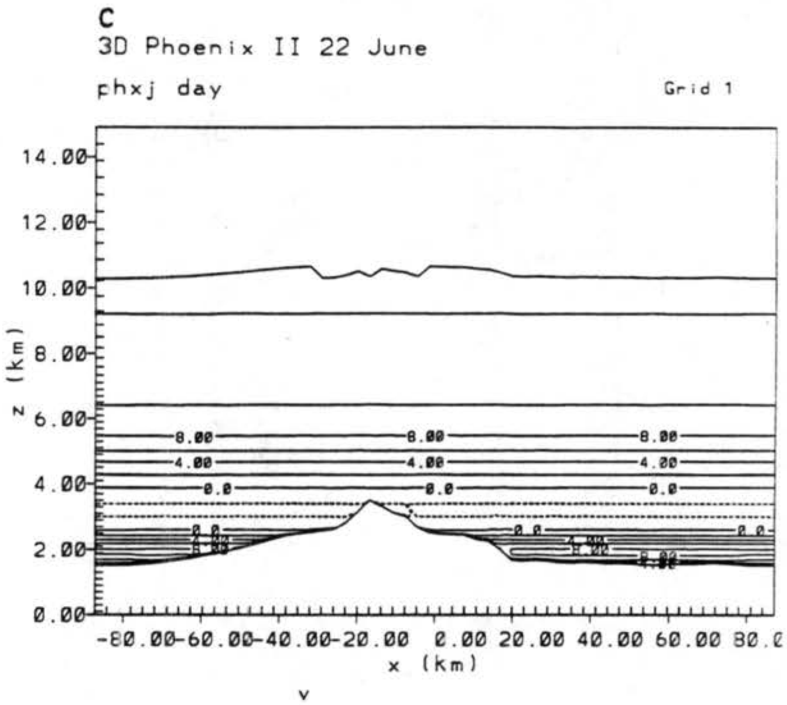


Figure 4.3: Continued.

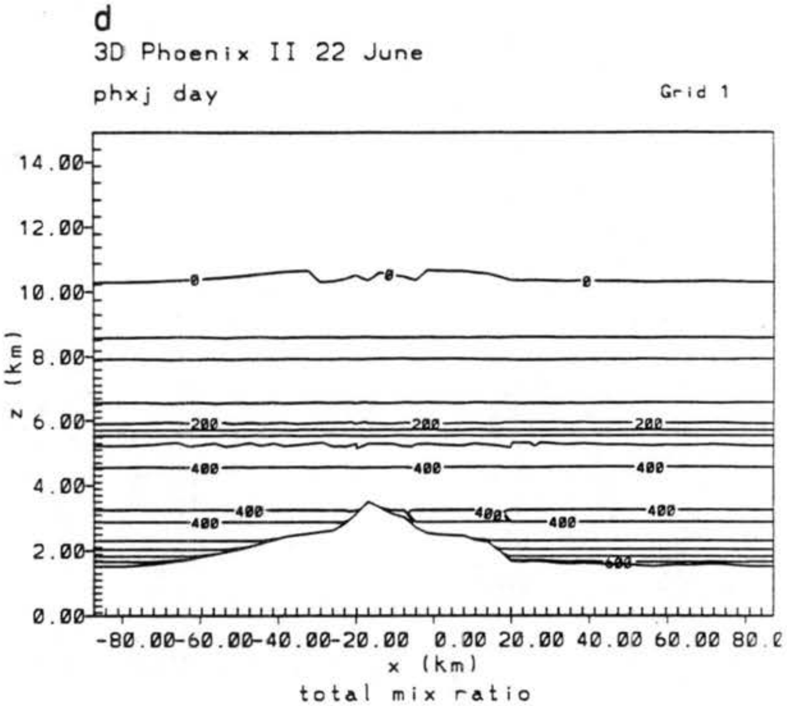


Figure 4.3: Continued.

## Chapter 5

# THE TWO-DIMENSIONAL SIMULATION

A two-dimensional simulation is carried out first to test the model in the configuration described in chapter 4 before running the expensive three-dimensional simulation. The results are analyzed primarily in a qualitative manner on both the LES grid and the larger grids, looking for realistic fields that are typical of this area at this time of year and roughly compare to the observed conditions on 22 June 1984. Some valuable insights are learned from these two-dimensional simulations in the process.

After initializing the model horizontally homogeneously at 0000 UTC (1700 MST), the simulation is allowed to run for twelve hours with the larger two grids. The model then has time to develop a realistic night time boundary layer throughout the domain before the LES grid is added for the time of interest of this study.

The temperature and wind fields which develop in the two-dimensional simulation by 1200 UTC (0500 MST) are shown in Figure 5.1. Because the vertical resolution of the model grids is rather course near the surface for a stable simulation at night, the surface inversion is not expected to be simulated very well. A surface temperature inversion has developed over the plains and high valleys while just above ridgetop the stability remains relatively weak. The lowest potential temperature at this time is 294 K next to the surface at the eastern edge of the domain. This is where the topography is lowest. Along the Front Range, the cool temperatures near the surface are approximately 302 K, the value of the potential temperature of the lowest level in the Denver rawinsonde sounding at this time.

A hint of the low level easterly winds that are used to initialize the model remain but downslope westerlies are evident near the surface east of the continental divide and

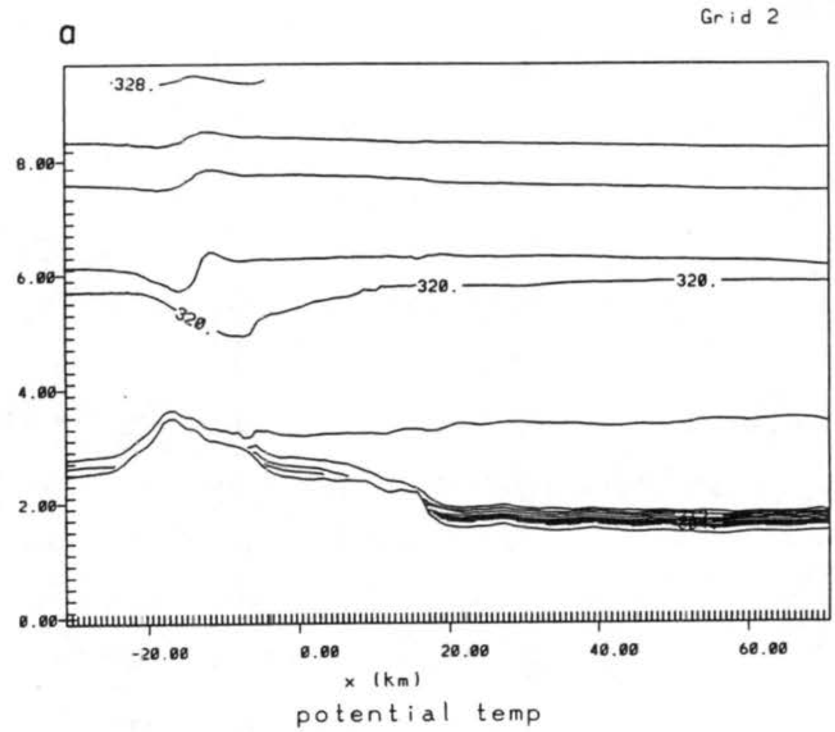


Figure 5.1: Two-dimensional fields of potential temperature (a) and u-component of the wind (b) on grid 2 at 1200 UTC (0500 MST). The contour intervals are 2.0 K in (a) and 2 $ms^{-1}$ in (b).

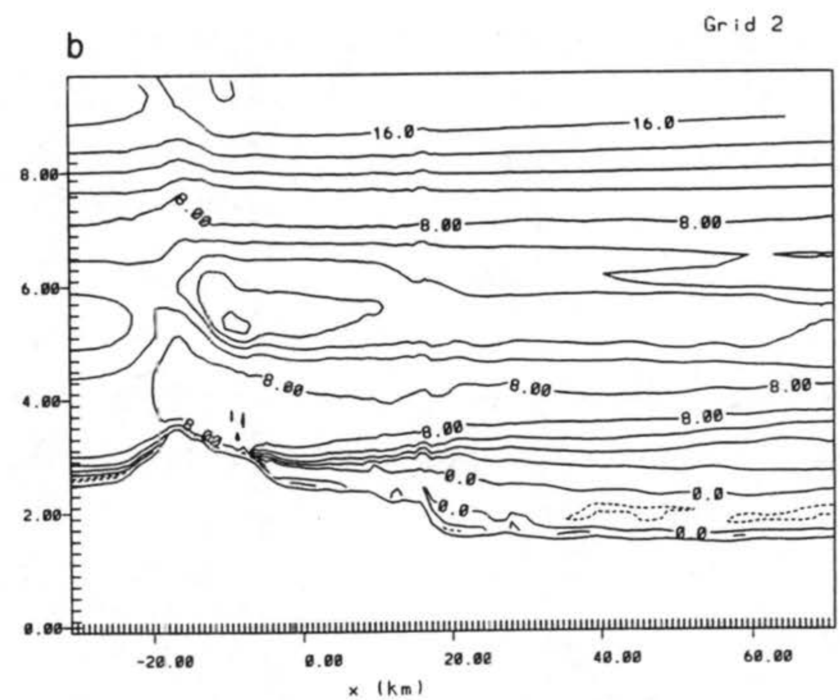


Figure 5.1: Continued.

downslope easterlies are found west of the continental divide. This is generally expected at night under weak synoptic conditions. At about 6 km MSL and east of the mountain barrier, there is evidence of a mountain induced wave in both fields. The wave can be seen in the 320 K and 322 K contours and at higher levels in the potential temperature field and in the local minimum of velocity at mid-levels in the u field. Wolyn (1992) discusses similar fields in his two-dimensional, mesoscale simulation along the Colorado Front Range.

The LES grid is added at this time, which is close to sunrise for this day, and the simulation is restarted and run throughout the morning and afternoon hours. As solar heating at the surface increases through the morning, eddies develop first over the highest terrain, where the surface inversion is most shallow. Later eddies also develop over the plains with the 'youngest' eddies on the eastern plains. Because of the wind shear present on this day, the elevated boundary layer is advected eastward over the growing boundary layer of the plains. This is in agreement with two dimensional mesoscale simulations of Wolyn and McKee (1990) and Arritt and Young (1990) that indicate warm air advecting off higher terrain when there are significant winds just above the higher terrain.

Figure 5.2 presents the potential temperature, u-component of the wind, and the vertical wind component fields on the LES grid, and Figure 5.3 presents the potential temperature field, the u-component of the wind, the vertical wind field, and the water vapor mixing ratio on grid 2 at 1720 UTC (1020 MST). By this time, the mountain induced wave has moved somewhat eastward, similar to the movement of the dip in isentropes discussed in Wolyn (1992) . The major updraft of 5 $ms^{-1}$ is coincident with the large, upward bulge in the isentropes. It is located where the upslope easterlies converge with the ambient westerlies, the lee side convergence zone investigated by Banta and Cotton (1981) and Banta (1984). The fields are also under the influence of gravity waves that appear to be triggered by the convection over the plains. The significant potential temperature and mixing ratio gradients above about 5.5 km MSL along with the approximately 8 $ms^{-1}$ winds are favorable conditions for convectively-induced gravity waves.

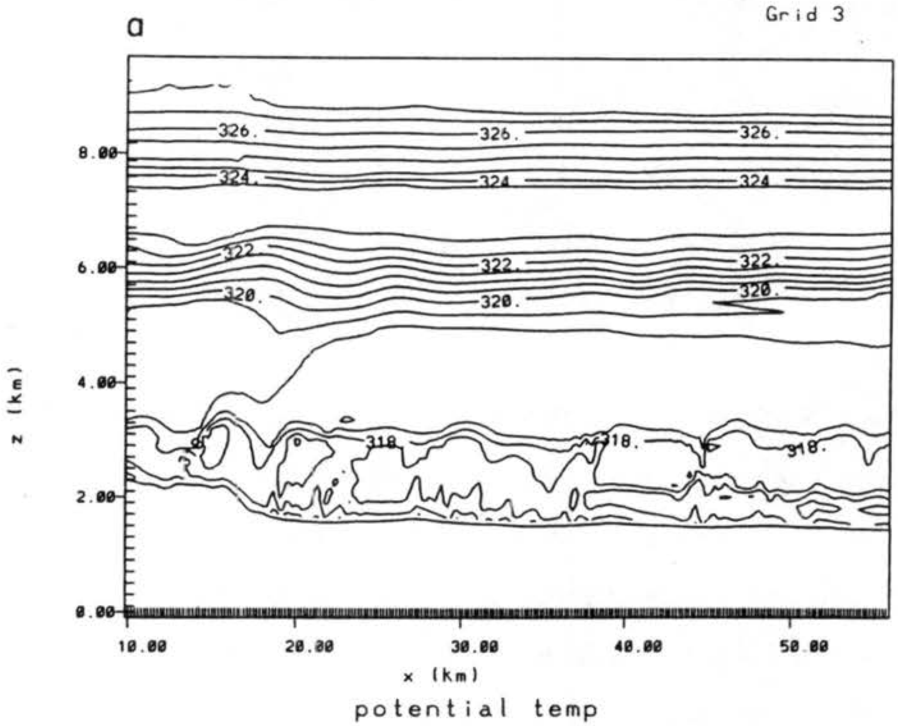


Figure 5.2: Two-dimensional fields of potential temperature (a), u-component of the wind (b), and vertical wind (c) on the LES grid at 1720 UTC (1020 MST). The contour intervals are 0.5 K in (a), 2 $ms^{-1}$ in (b), and 1 $ms^{-1}$ in (c).

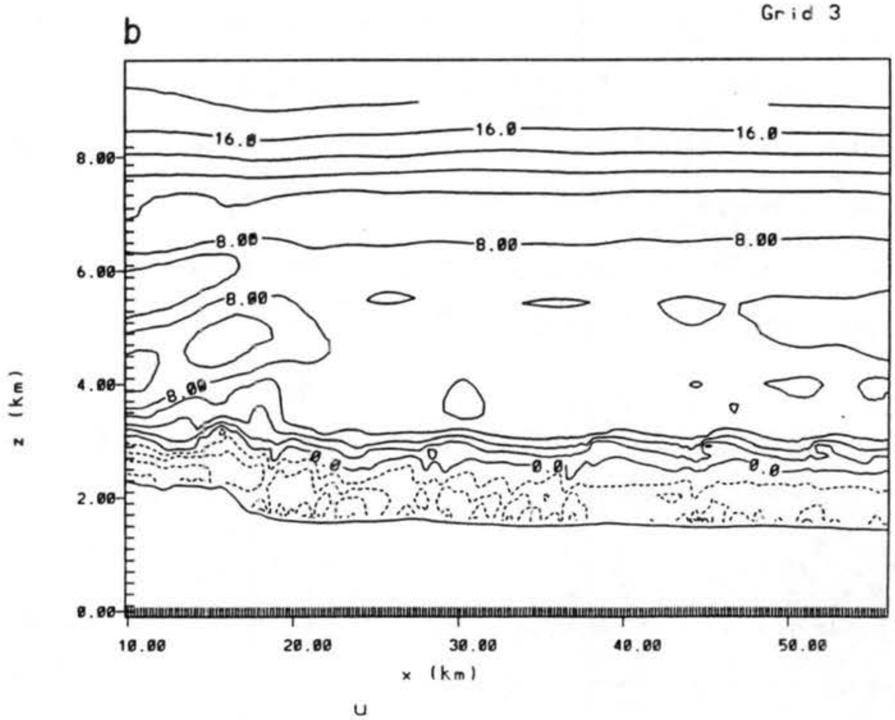


Figure 5.2: Continued.

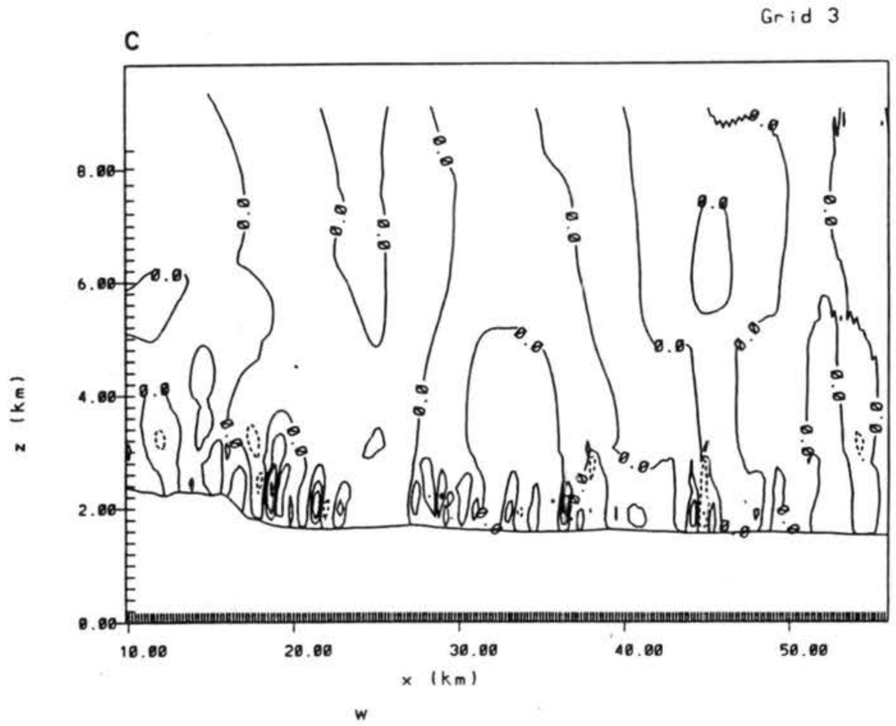


Figure 5.2: Continued.

There is evidence of the developing eddies of the growing plains boundary layer. Note the 319.0 K contour line in the potential temperature field of Figure 5.2. It indicates the advection of the warm air from the elevated boundary layer above the western end of the Colorado High Plains. The u-component of the wind at this time shows a distinctive mountain plains circulation on the eastern slope. There is a well developed layer of easterlies near the surface; however, the magnitude of the low level easterlies varies by as much as 4 $ms^{-1}$ in the horizontal direction, indicating the presence of the eddies. The narrow updraft portions of the large eddies are evident in the vertical wind component field.

It is interesting to examine the water vapor mixing ratio field because water vapor is a passive tracer (except for its source due to evaporation near the surface). The large size and deep extent of the circulations in the mountain boundary layer can be seen (Figure 5.3) with some evidence in the 3.5 $gkg^{-1}$ contour line of these circulations being advected eastward. The separate development of the plains boundary layer is also notable with the western part of the plains boundary layer having the largest eddies.

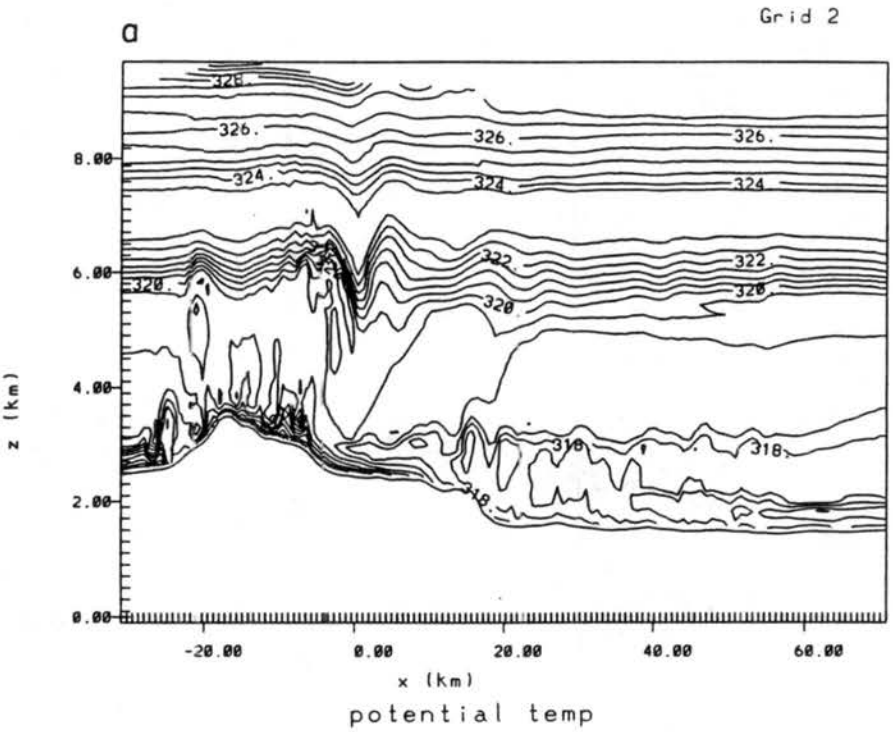


Figure 5.3: Two-dimensional fields of potential temperature (a), u-component of the wind (b), vertical wind (c), and total water vapor mixing ratio (d) on grid 2 at 1720 UTC (1020 MST). The contour intervals are 0.5 K in (a), 2 $ms^{-1}$ in (b), 1 $ms^{-1}$ in (c), and 0.5 $gkg^{-1}$ in (d).

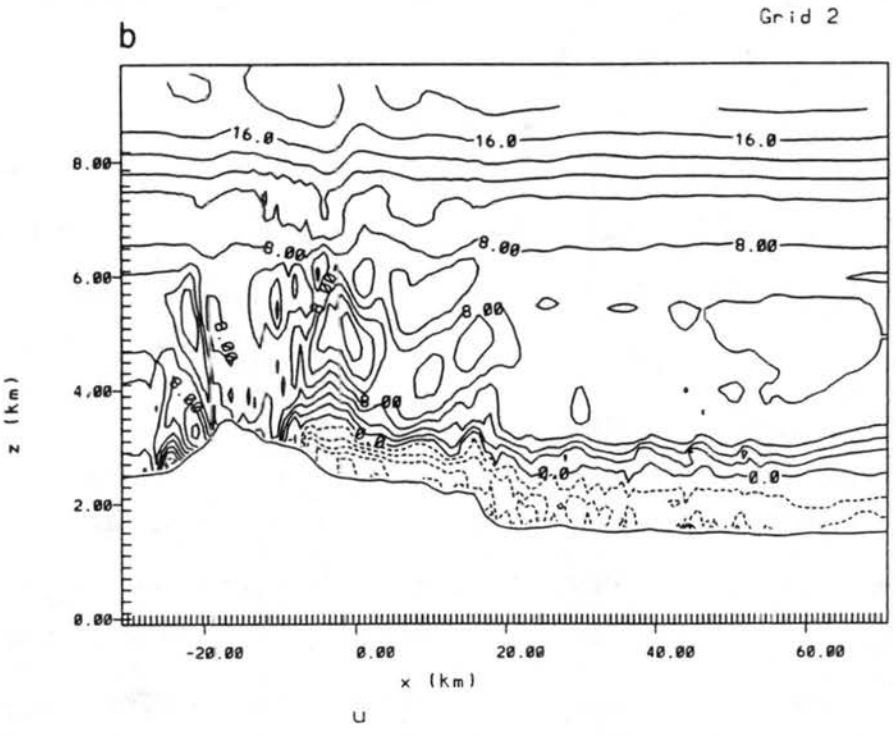


Figure 5.3: Continued.

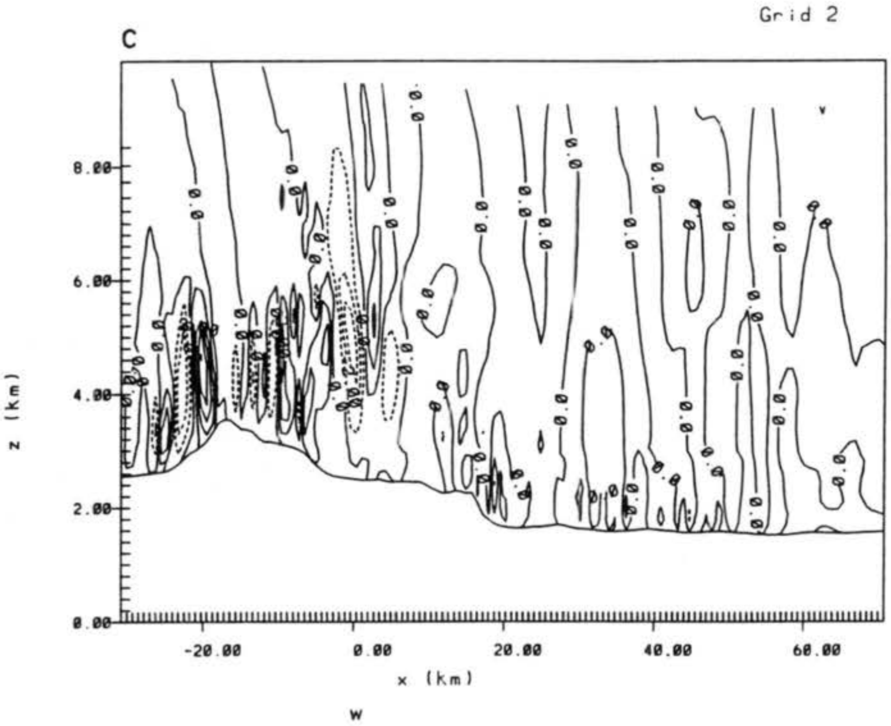


Figure 5.3: Continued.

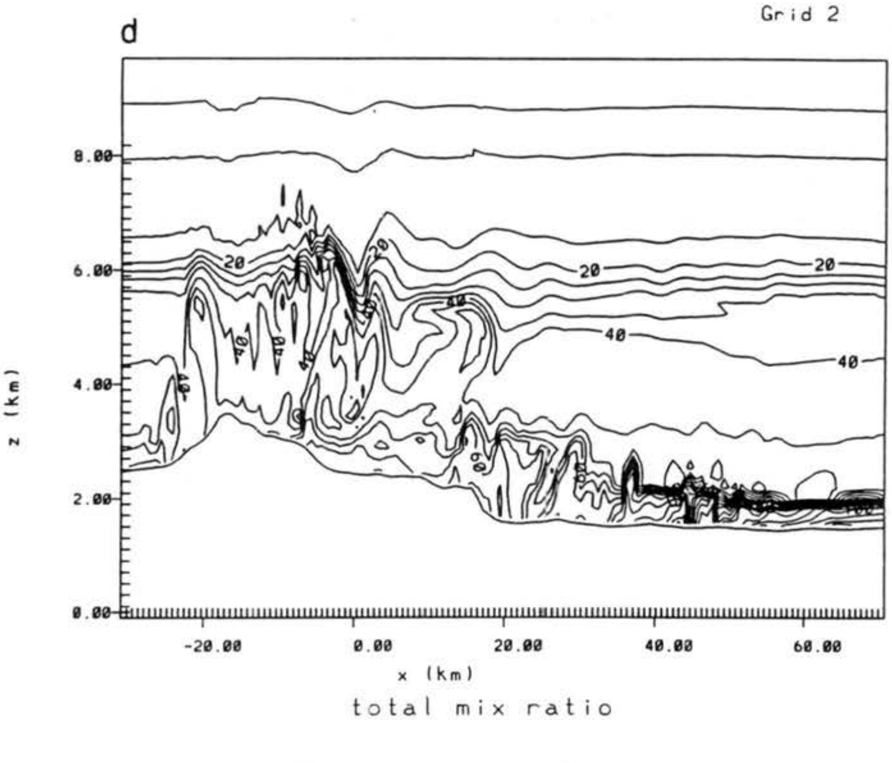


Figure 5.3: Continued.

Figure 5.4 is a time series of the water vapor mixing ratio field at 30 minute intervals. Eddies on the western end of the Great Plains are evident at 1650 UTC (0950 MST), with very little convection in the east. At 1720 UTC (1020 MST) the moisture associated with the elevated boundary layer is beginning to move eastward. The circulations seem to weaken as they move away from their source, the elevated terrain. With time, the plains boundary layer continues to grow deeper, and the eddies within it grow larger. At the same time, the upper level moisture from the mountain boundary layer continues to advect eastward. Note the 3.5 $gkg^{-1}$ contour at 1750 UTC (1050 MST). The wave-like appearance in the moisture field again suggests the presence of gravity waves.

By 1820 UTC (1120 MST), the plains boundary layer has grown deep enough to interact with the upper level boundary layer. The eddies of the plains boundary layer are nearly 10 km across in this two dimensional simulation. Although the eddies in the simulation are similar in character to the observed eddies, they are much larger. The observations from Phoenix II indicated that the eddies were less than half this size. The depth of the boundary layer is also significantly deeper than the observed maximum depth of the boundary layer of about 3.5 km, despite initialization with very moist soil to encourage evaporation and decrease sensible heating. It will be shown in Chapter 6 that the eddies in the three dimensional simulation do not grow to be as large because the circulations can be three dimensional and allow energy to cascade down scale to smaller circulations and eventually to dissipation at much smaller scales.

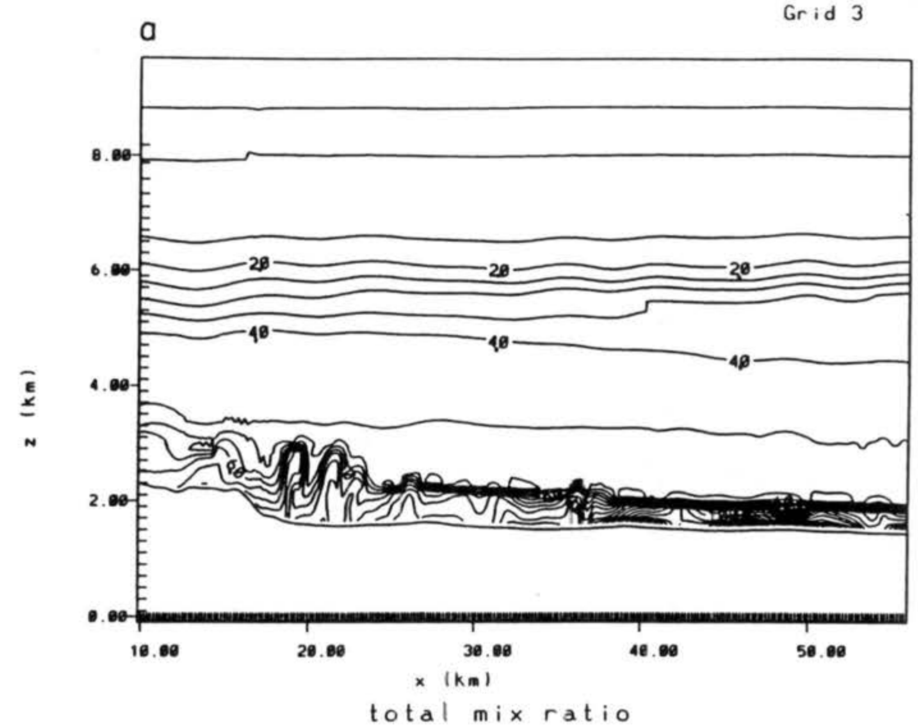


Figure 5.4: Two-dimensional fields of total water vapor mixing ratio on the LES grid at 1650 UTC (0950 MST) (a), 1720 UTC (1020 MST) (b), 1750 UTC (1050 MST) (c), and 1820 UTC (1120 MST) (d). The contour interval is 0.5 $gkg^{-1}$.

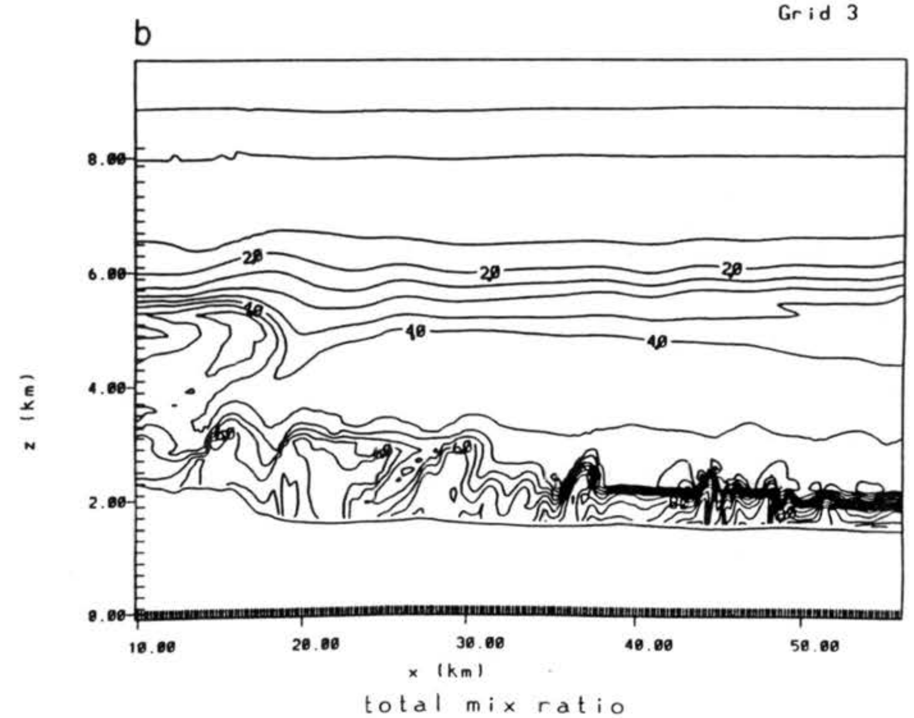


Figure 5.4: Continued.

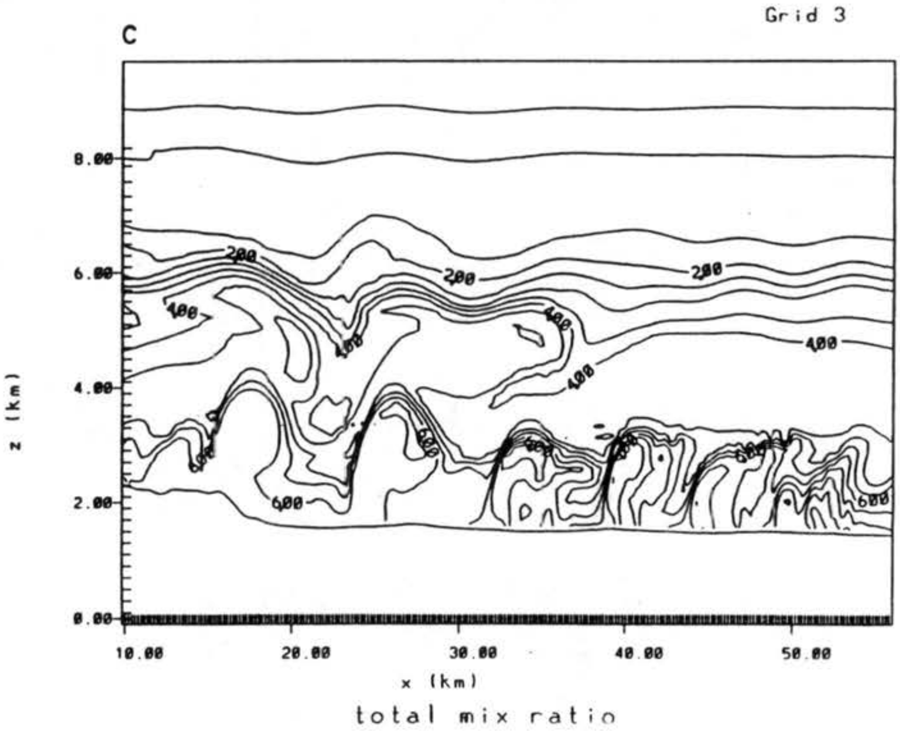


Figure 5.4: Continued.

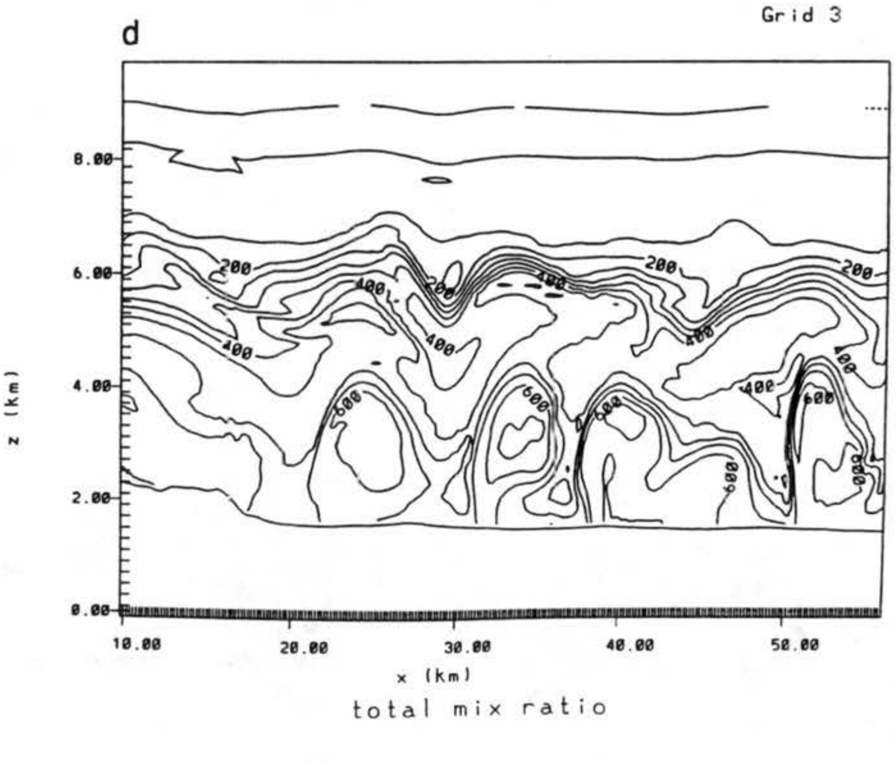


Figure 5.4: Continued.

## Chapter 6

# THE THREE-DIMENSIONAL 'CHANNEL' SIMULATION

The three-dimensional simulation is carried out to model the atmospheric boundary layer on 22 June 1984. Because the simulation is three-dimensional, the eddies are more realistic and the modeled circulations more closely resemble those actually observed during Phoenix II. The analysis in this chapter can therefore be more extensive. Direct comparisons to the observations include the field plots of two-dimensional slabs through the domain as were presented in Chapter 5 along with vertical profiles of the turbulent statistics. Spectral analysis is also performed. These comparisons establish that the model reproduces the observations reasonably well. Comparisons to previous LES's for horizontally homogeneous conditions indicate how the boundary layer observed during Phoenix II differs from the horizontally homogeneous boundary layer and the influence of the mountain barrier to the west is determined.

The vertical profiles are obtained by averaging the model predictions in space and time. The data are averaged in the horizontal and the horizontal means are performed for a 20 minute time period. In computing the horizontal average, only data from grid points over the plains portion of the LES grid are used. This method of averaging is the same approach used by Schneider (1991). The 20 minute time period is approximately the time period that she used and is typical of the convective time scale for this day. Table 1 lists the blocks of data used by Schneider and the times they were obtained, along with the corresponding time over which the model results were averaged.

## 6.1 Evolution of the Model-Predicted Fields

As in the two-dimensional simulation, the three-dimensional simulation is initialized at 0000 UTC (1700 MST 21 June) with just the largest two grids. The simulation runs 12 hours, through the night, to develop a reasonable night time boundary layer. Figure 6.1 shows the fields at 1200 UTC (0500 MST) in a two-dimensional slab through the domain. The fields are similar to the two-dimensional simulation at this time, except that the surface potential temperature inversion is not as strong, probably due to the use of the Louis (1979) surface layer parameterization, the only one available in the newer version of RAMS, in the three-dimensional simulation instead of the Businger et al. (1971) scheme, which was used for the two-dimensional run. Also, the water vapor mixing ratios near the surface are not as high in the three-dimensional simulation. The lower mixing ratios are the result of lower, more realistic, initial soil moisture and less evaporation very early in the simulation.

### 6.1.1 Comparison to two-dimensional simulation

Again the LES grid is added at 1200 UTC (0500 MST), which is near sunrise, and the model is run through the morning and afternoon hours. The boundary layer growth is not as rapid in this three-dimensional simulation as it was in the two-dimensional simulation. Figure 6.2 gives two-dimensional plots of the three-dimensional run at 1820 UTC (1120 MST). This is one hour later than shown in Figure 5.2 for the two-dimensional simulation. The presence of large eddies in the plains boundary layer is seen and an indication of the upper level advection of warm air is given by the 318.5 K contour line. The u-component of the wind also shows the maintenance of the upper level westerlies along with the lower level easterly winds of a few meters per second. The v-component of the wind shows that there is a light southerly component to the wind up to about 5.7 km MSL. The southerly winds increase somewhat above this level, but the shear is not as strong as in the u-component of the wind. It is located significantly higher than the plains boundary layer depth, at the base of the stronger inversion and above the mountain boundary layer.

Again the vertical velocity field contains relatively narrow, concentrated updrafts amidst weaker downdrafts in the plains boundary layer. The maximum updraft speed is 4 $ms^{-1}$ compared to $3ms^{-1}$ found an hour earlier in the two-dimensional run. Above the plains boundary layer, the vertical motion is quite a bit weaker and the areas of updrafts

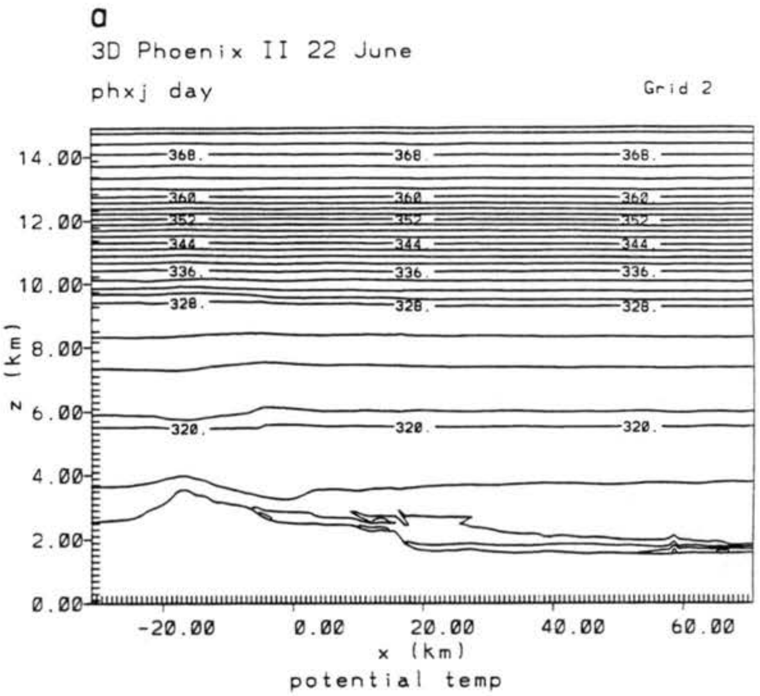


Figure 6.1: Vertical x-z cross sections of potential temperature (a), u-component of the wind (b), v-component of the wind (c), and total water vapor mixing ratio (d) on grid 2 at 1200 UTC (0500 MST). The contour intervals are 2.0 K in (a), 2 $ms^{-1}$ in (b), 2 $ms^{-1}$ in (c), and 0.5 $gkg^{-1}$ in (d).

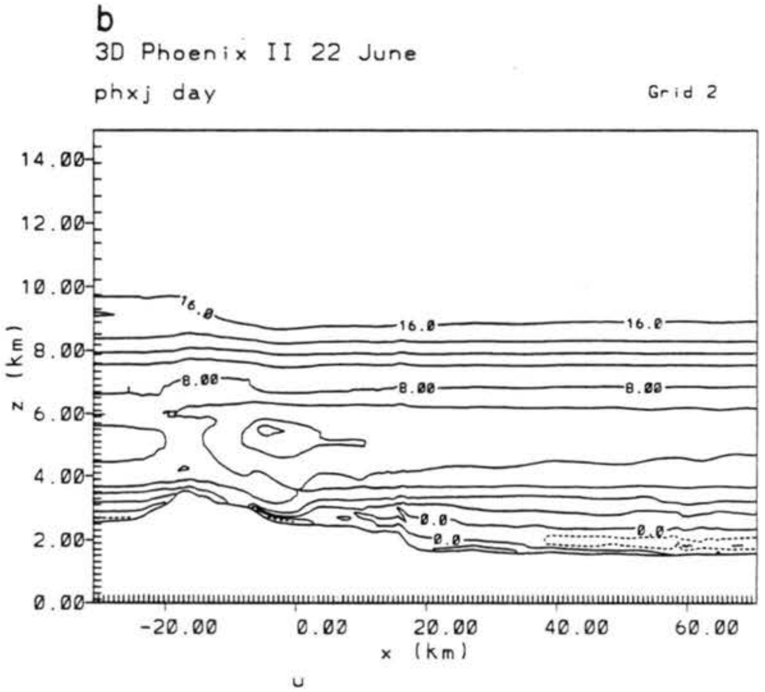


Figure 6.1: Continued.

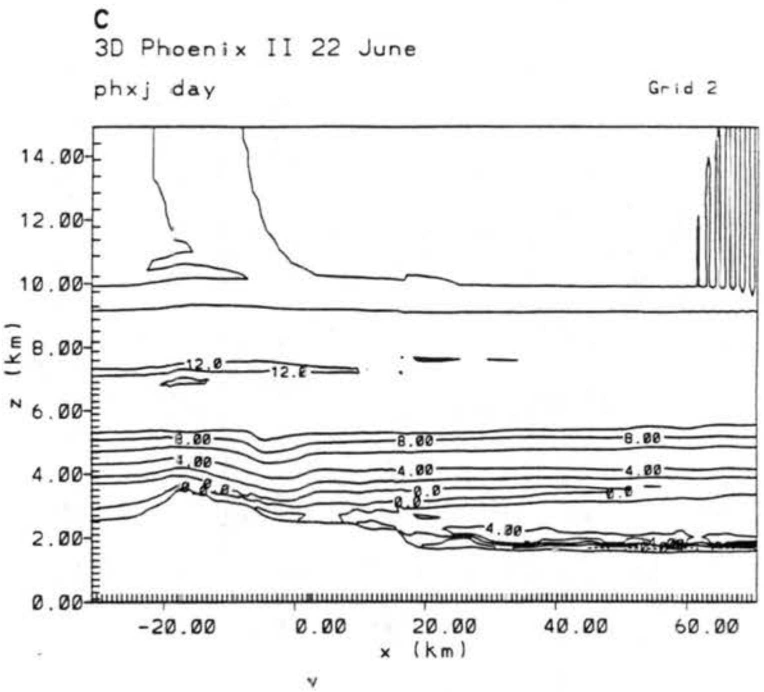


Figure 6.1: Continued.

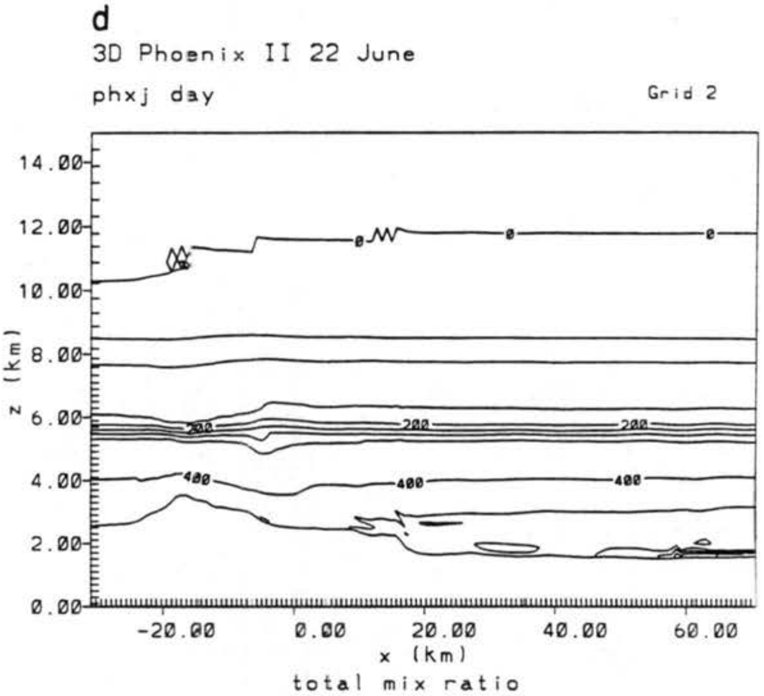


Figure 6.1: Continued.

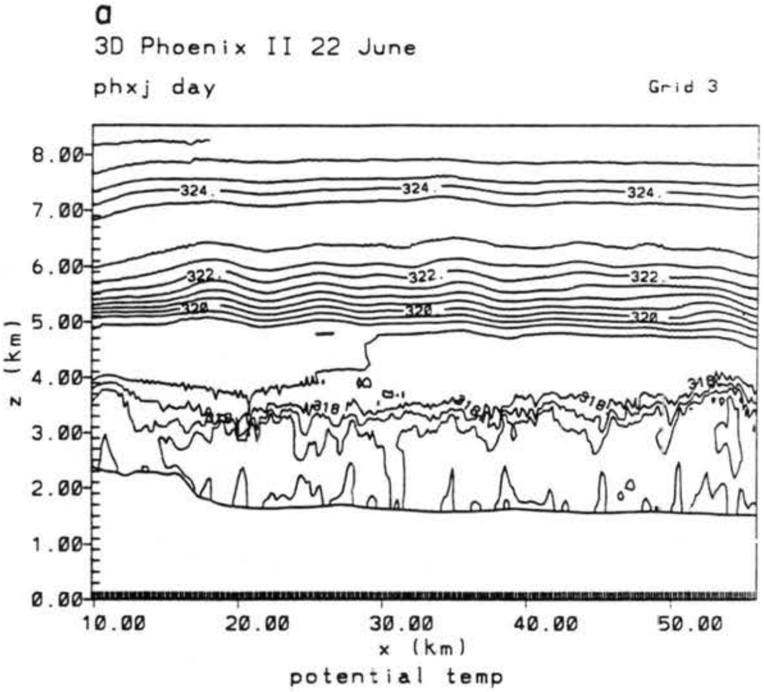


Figure 6.2: Vertical x-z cross sections of potential temperature (a), u-component of the wind (b), v-component of the wind (c), vertical wind speed (d), total water vapor mixing ratio (e), and subgrid turbulent kinetic energy (f) on the LES grid at 1820 UTC (1120 MST). The contour intervals are 0.5 K in (a), 2 $ms^{-1}$ in (b), 2 $ms^{-1}$ in (c), 1 $ms^{-1}$ in (d), and 0.2 $gkg^{-1}$ in (e), and 0.5 $m^2s^{-2}$ in (f).

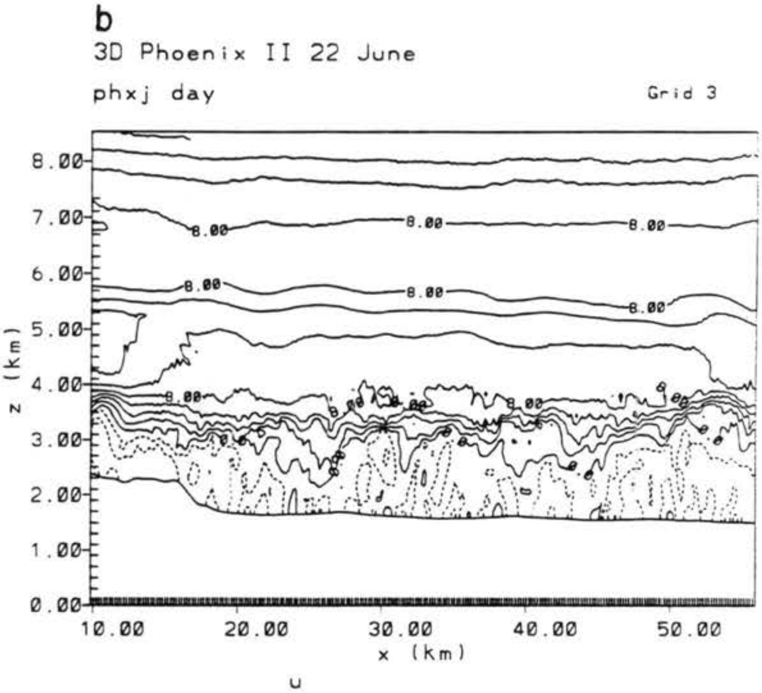


Figure 6.2: Continued.

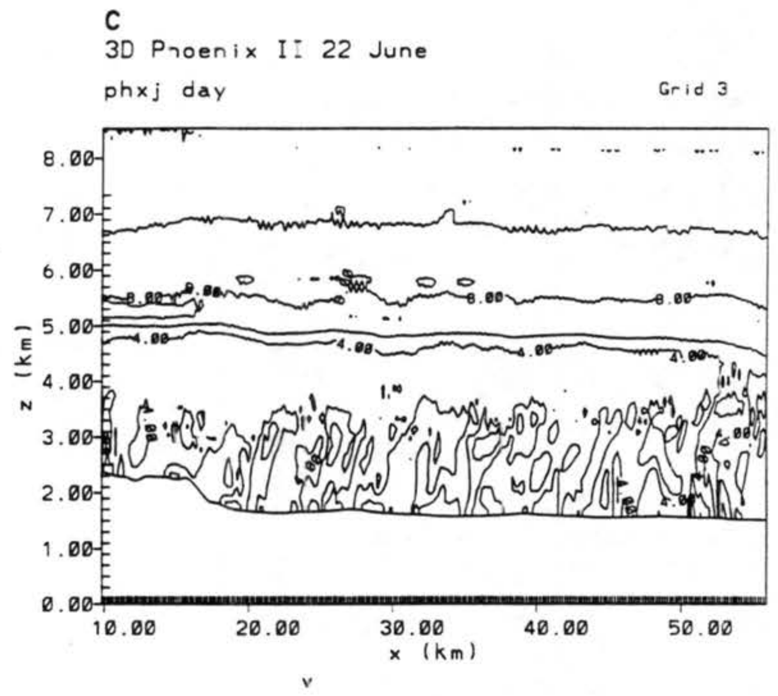


Figure 6.2: Continued.

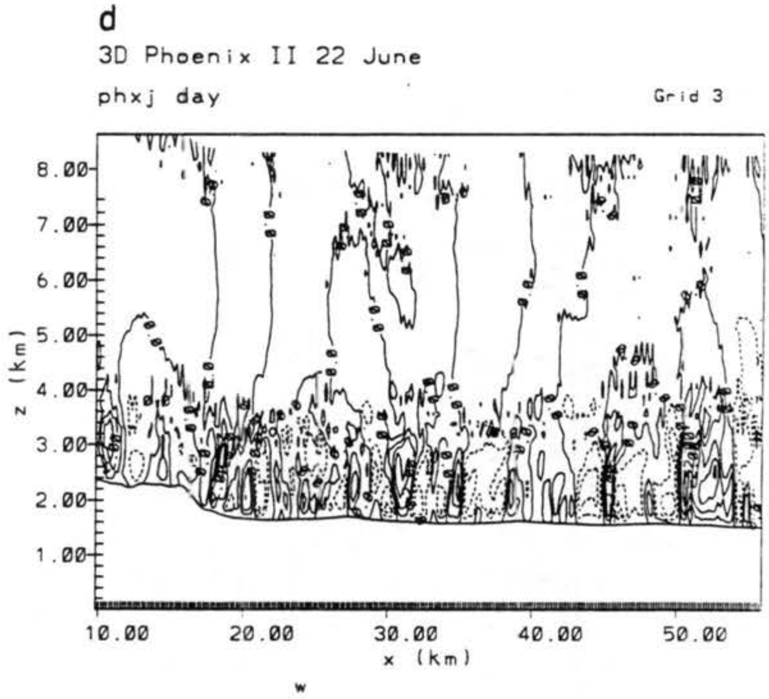


Figure 6.2: Continued.

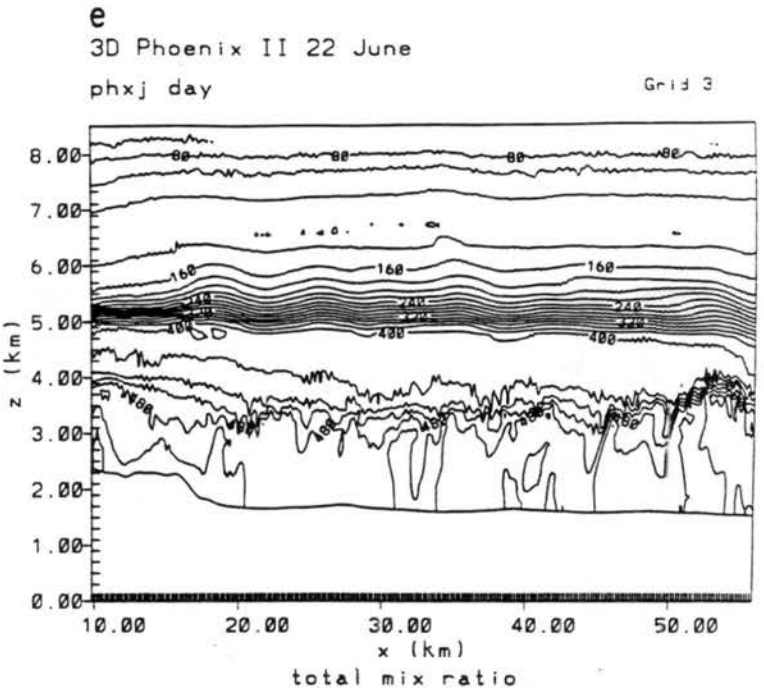


Figure 6.2: Continued.

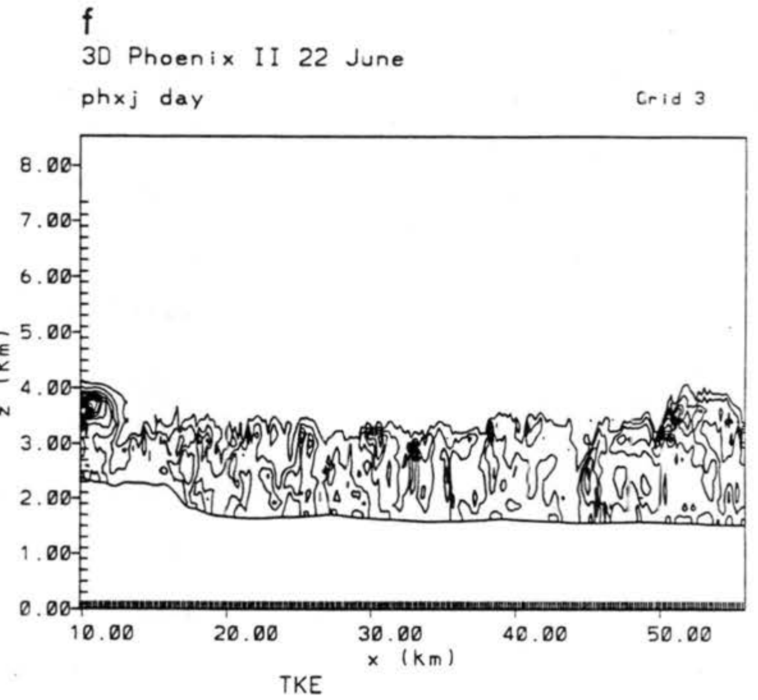


Figure 6.2: Continued.

and downdrafts occupy more comparable size areas. The size of the circulations also seem to be larger above the plains boundary layer. This is not a pattern expected in a boundary layer dominated by large eddies but more a pattern expected in the presence of gravity waves.

The water vapor mixing ratio field no longer shows the dramatic wave- like advection of the moisture as in the two-dimensional simulation. In general, the advection of the mountain boundary layer is not as obvious in the three-dimensional simulation. Advection is not confined to the east-west direction in a three-dimensional simulation, and because the energy can cascade to smaller scaled circulations in three dimensions, smaller scale eddies play more of a role. The net effect is a more mixed moisture field. The subgrid turbulent kinetic energy field shows the turbulent kinetic energy predicted at scales smaller than the grid resolution and indicates the intensity of the eddies.

Each of these plots shows some degree of noise in the fields. The noise is generally features of the size of 2 $\Delta x$ and should not be treated as credible as they represent the inability of the Deardorff (1980) subgrid parameterization to remove all subgrid scale turbulence. In areas of static stability, subgrid diffusion is suppressed in Deardorff's scheme, and the noise is, for the most part, confined to the stable regions. Any adjustments of the subgrid parameterization to correct for noise would be artificial and might adversely affect its performance in the convective regions. So, for this study, the noise is just ignored.

Figure 6.3 shows vertical cross sections of the same fields in the y direction at the same time. In general, these fields are smoother than in the east-west direction. They appear smoother partly due to the scaling of the plots.

Figures 6.4 and 6.5 give the cross sections of the fields one hour and 20 min later at 1940 UTC (1240 MST). The potential temperature field shows that the plains boundary layer continues to warm and grow deeper to over 4 km MSL. However, the boundary layer is not as deep as predicted in the two-dimensional simulation, which indicated the merging of the plains and mountain boundary layers by 2000 UTC (1200 MST) and their combined depth was about 7 km. The 319.0 and 319.5 K potential temperature contours continue to suggest advection of warm air eastward from the mountain boundary layer.

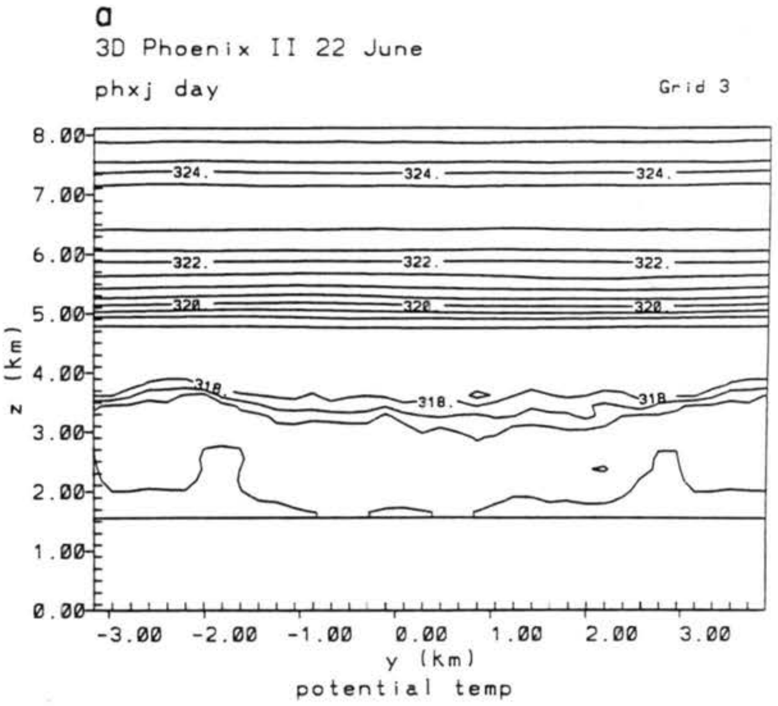


Figure 6.3: Vertical y-z cross sections of potential temperature (a), u-component of the wind (b), v-component of the wind (c), vertical wind speed (d), total water vapor mixing ratio (e), and subgrid turbulent kinetic energy (f) on the LES grid at 1820 UTC (1120 MST). The contour intervals are 0.5 K in (a), 2 $ms^{-1}$ in (b), 2 $ms^{-1}$ in (c), 1 $ms^{-1}$ in (d), and 0.2 $gkg^{-1}$ in (e), and 0.5 $m^2s^{-2}$ in (f).

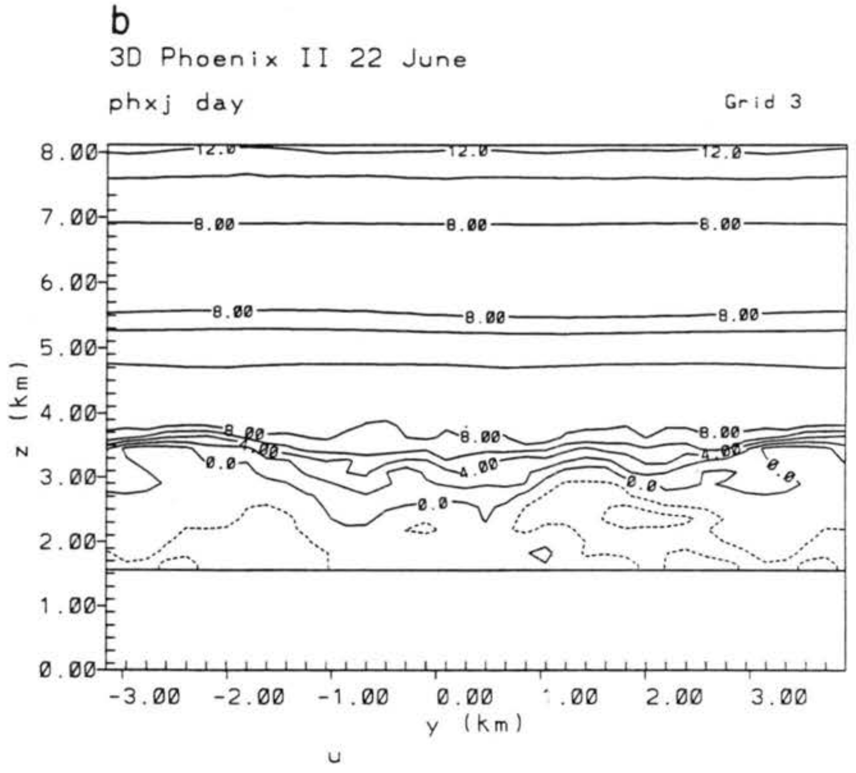


Figure 6.3: Continued.

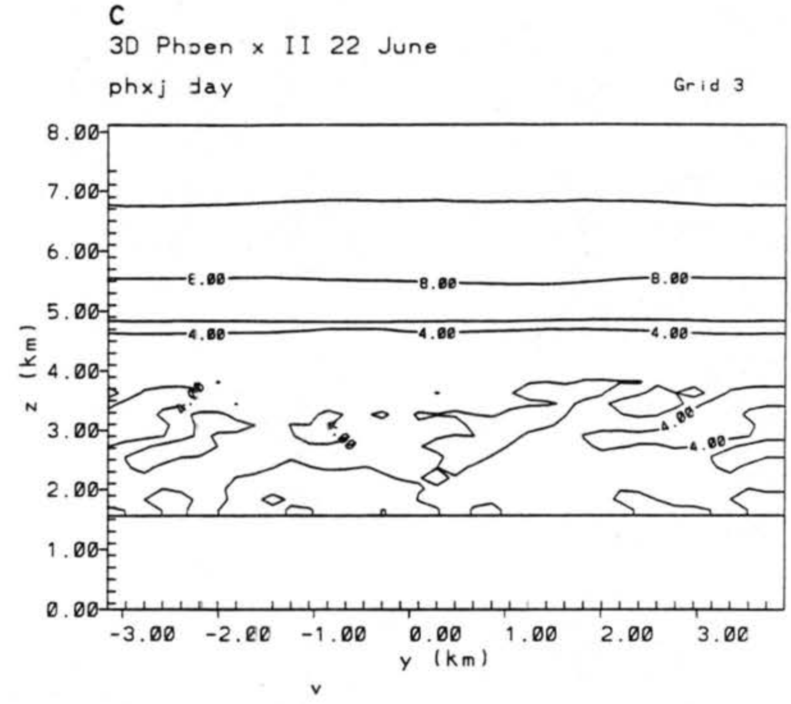


Figure 6.3: Continued.

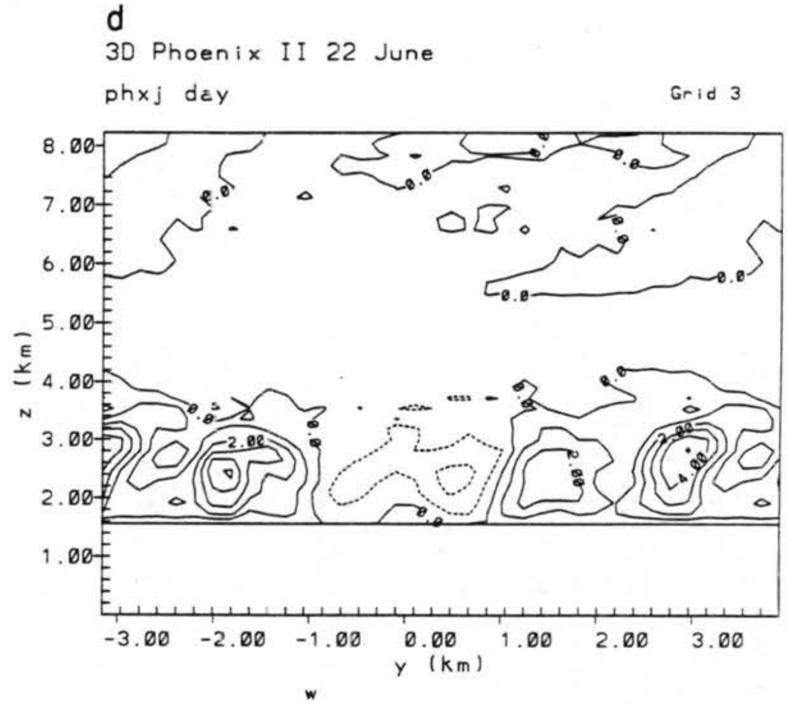


Figure 6.3: Continued.

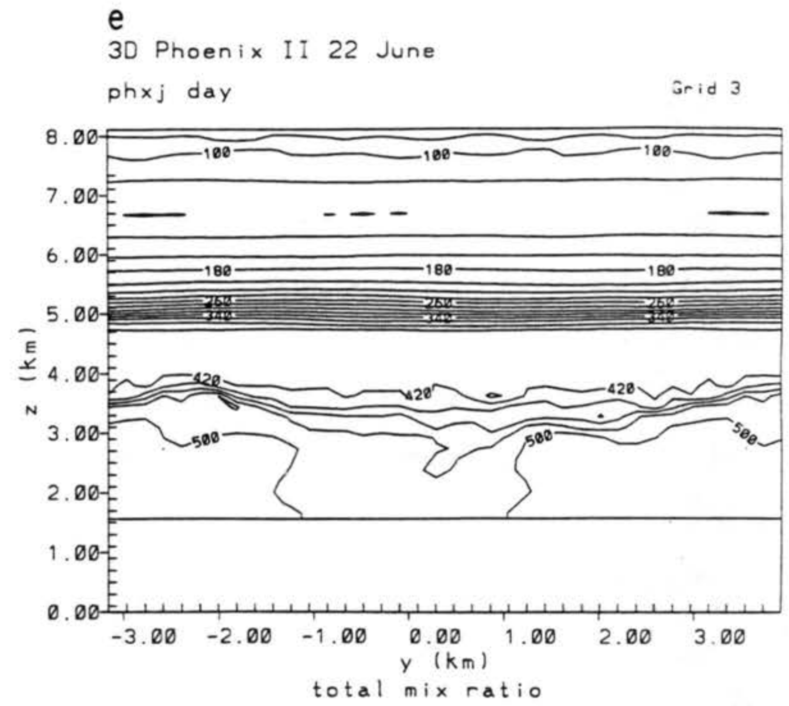


Figure 6.3: Continued.

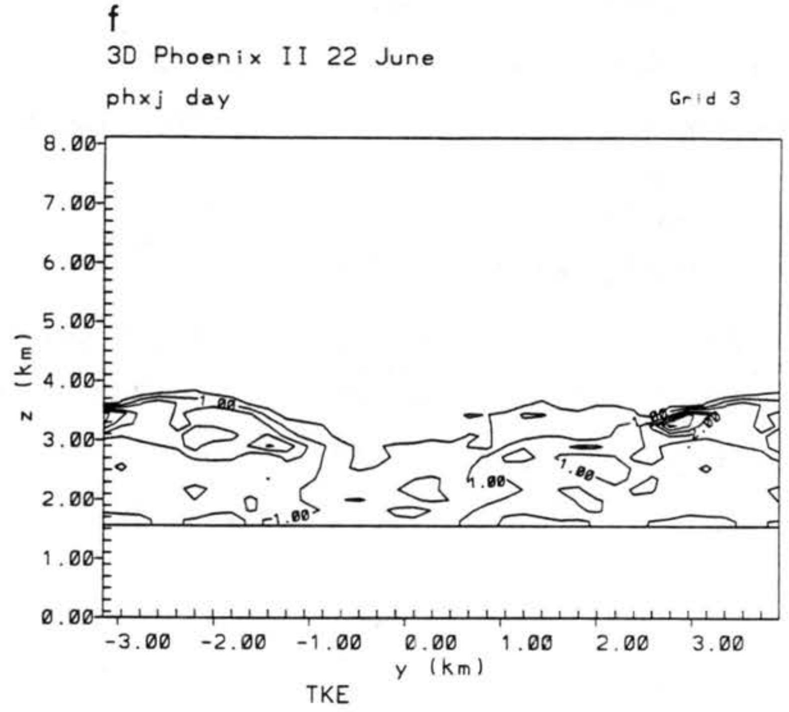


Figure 6.3: Continued.

The waves in the inversion layer between 5 and 6 km MSL are more apparent at this time.

The horizontal wind fields, on the average, have changed little but the fluctuations due to the presence of the large eddies are evident. In the vertical motion field, the maximum updraft speed increased somewhat to 5 $ms^{-1}$. The two-dimensional simulation predicted updraft speeds nearly twice as large. The distinction between the plains boundary layer and the mountain boundary layer in the w field is not as obvious at this time. The upper boundary layer appears to not only be influenced by waves, but also by turbulence. This turbulence in the mountain boundary layer is intermittent, as can be seen when the field is animated.

The water vapor mixing ratio and subgrid turbulent kinetic energy fields also reflect the greater depth of the plains boundary layer at this time.

Later in the simulation, a lee side convergence zone, as described by Banta (1984), can be seen moving into the LES grid. This is an area marked by relatively strong upward motion, where the easterly winds of the thermally-induced circulation encounter the upper level westerly winds. From the animation of the wind fields, the slow progression of the lee side convergence zone down the eastern slope of the Colorado Rockies can be observed. The lee side convergence zone enters the LES grid approximately 9.5 hours after sunrise or about 1430 MST.

### 6.1.2 Comparisons to Phoenix II observations

The development of the plains boundary layer predicted by the model is in agreement with the observations during the Phoenix II field program. Exact comparisons are not always possible because of the manner in which the observations were obtained. The aircraft observations collected data in flight legs, which were essentially two-dimensional, and the radar observations were limited to an approximately 9 km square area, significantly smaller than the LES domain. Nevertheless, comparing the mean conditions is useful and lends credibility to the model results.

Figures 6.6 and 6.7 show streamlines of the flow field in both the east-west and north-south directions at the approximate location of the BAO tower. The scales of the

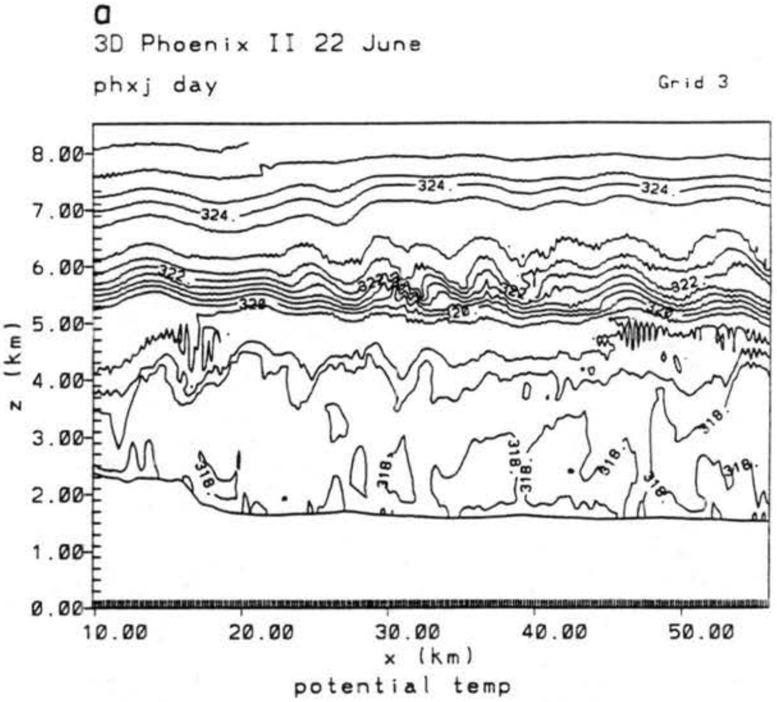


Figure 6.4: Vertical x-z cross sections of potential temperature (a), u-component of the wind (b), v-component of the wind (c), vertical wind speed (d), total water vapor mixing ratio (e), and subgrid turbulent kinetic energy (f) on the LES grid at 1940 UTC (1240 MST). The contour intervals are 0.5 K in (a), 2 $ms^{-1}$ in (b), 2 $ms^{-1}$ in (c), 1 $ms^{-1}$ in (d), and 0.2 $gkg^{-1}$ in (e), and 0.5 $m^2s^{-2}$ in (f).

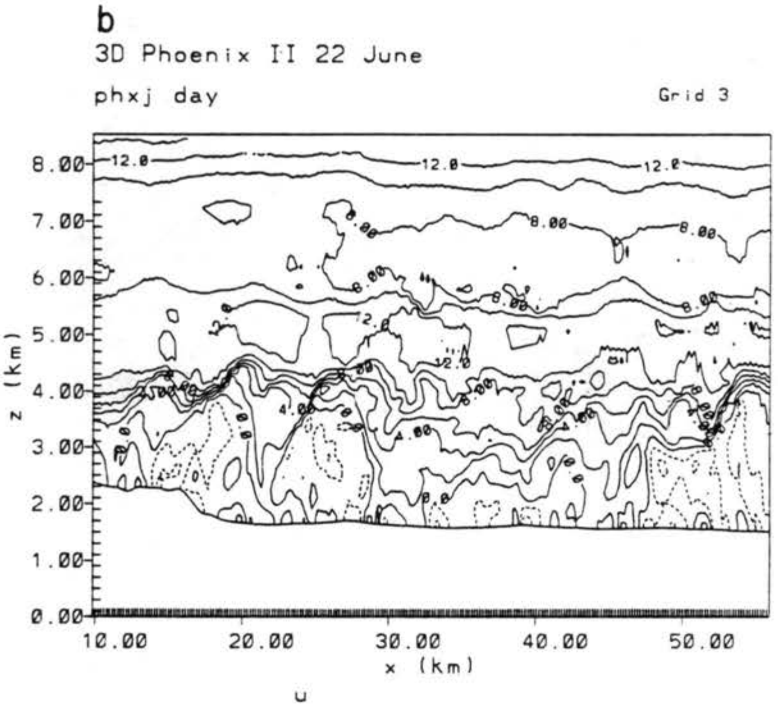


Figure 6.4: Continued.

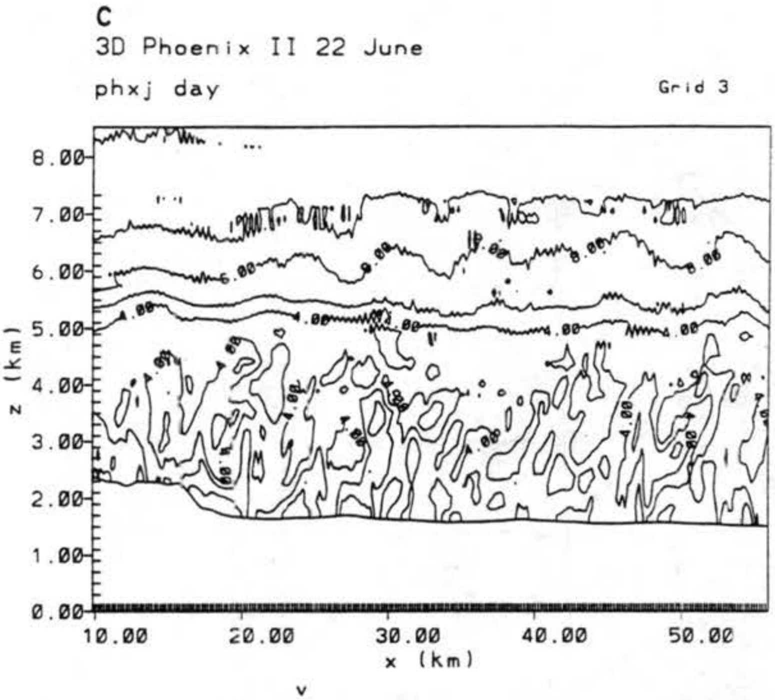


Figure 6.4: Continued.

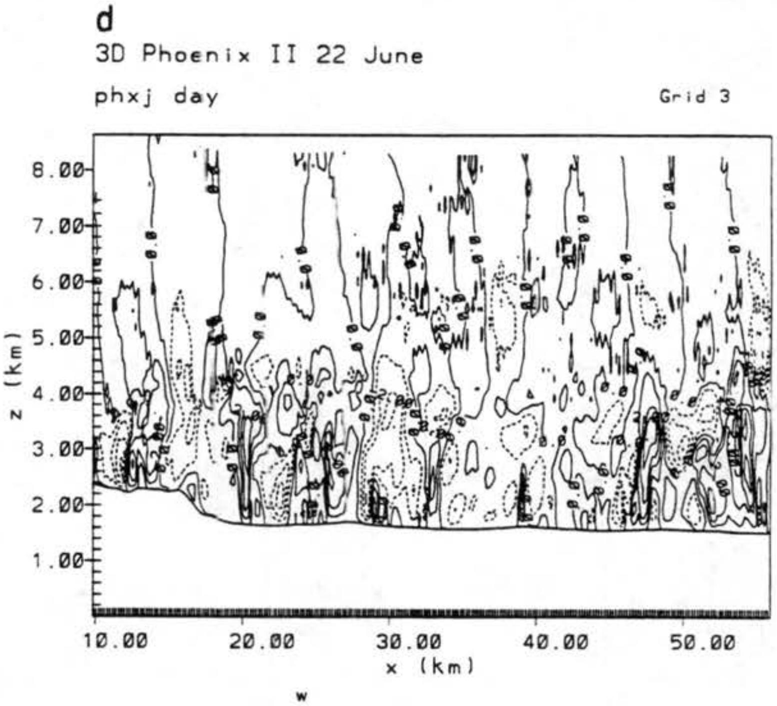


Figure 6.4: Continued.

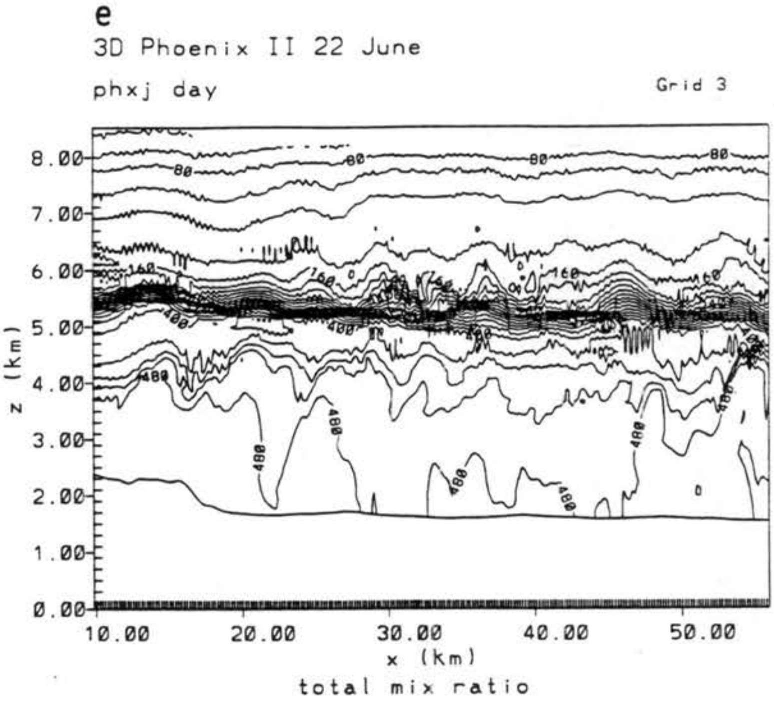


Figure 6.4: Continued.

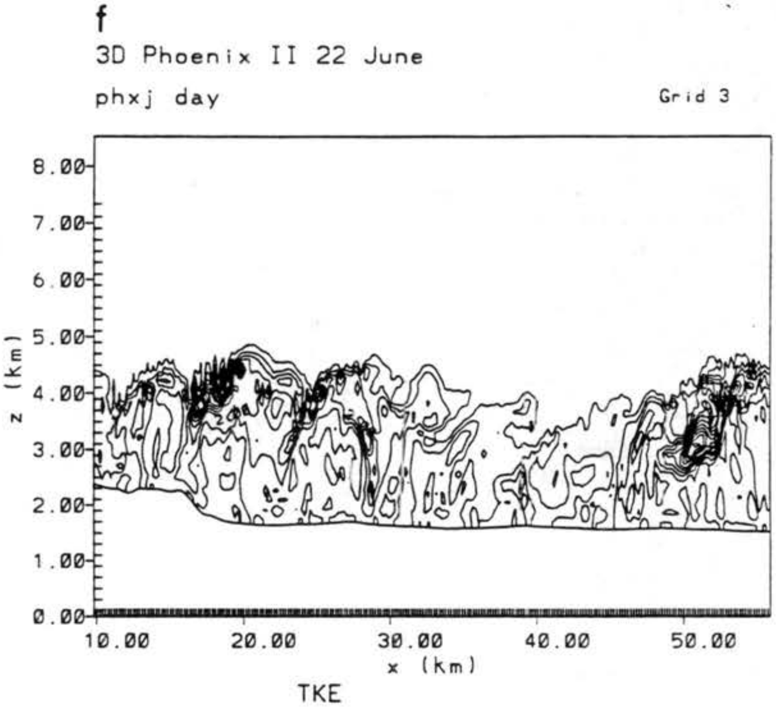


Figure 6.4: Continued.

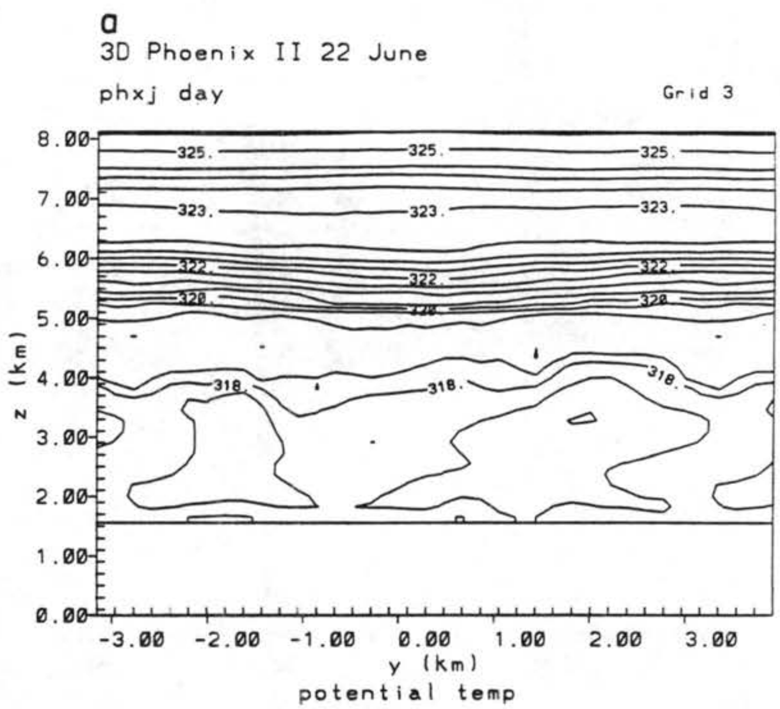


Figure 6.5: Vertical y-z cross sections of potential temperature (a), u-component of the wind (b), v-component of the wind (c), vertical wind speed (d), total water vapor mixing ratio (e), and subgrid turbulent kinetic energy (f) on the LES grid at 1940 UTC (1240 MST). The contour intervals are 0.4 K in (a), 2 $ms^{-1}$ in (b), 2 $ms^{-1}$ in (c), 1 $ms^{-1}$ in (d), and 0.2 $gkg^{-1}$ in (e), and 0.5 $m^2s^{-2}$ in (f).

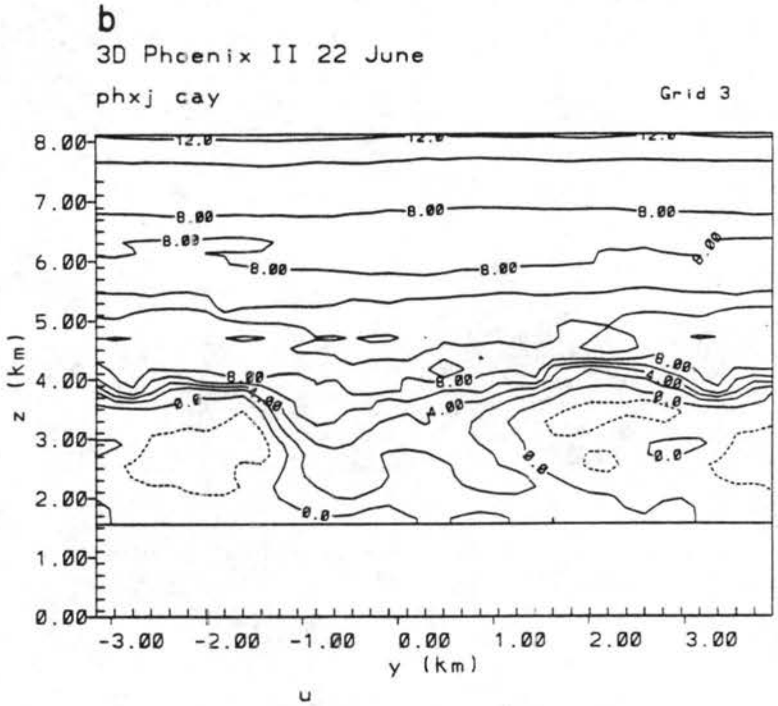


Figure 6.5: Continued.

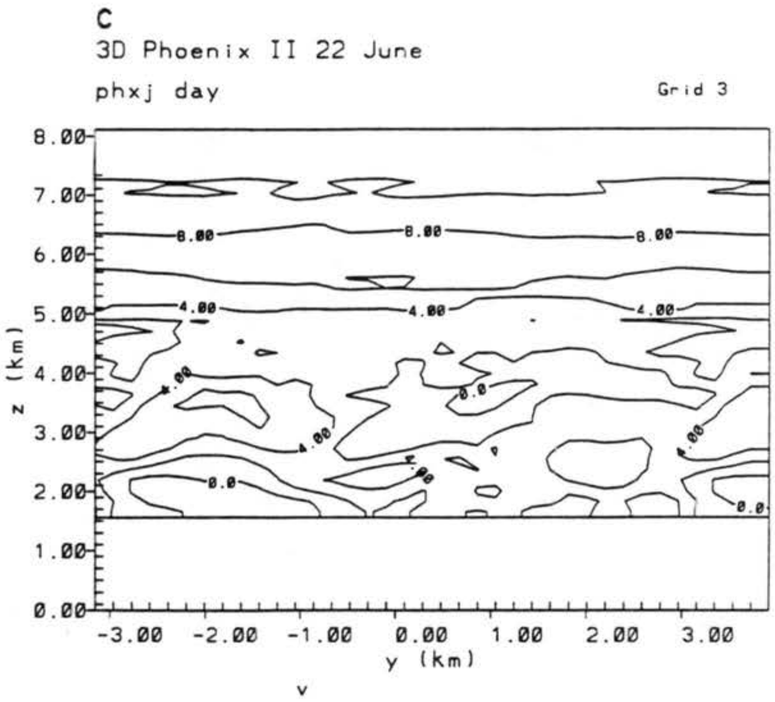


Figure 6.5: Continued.

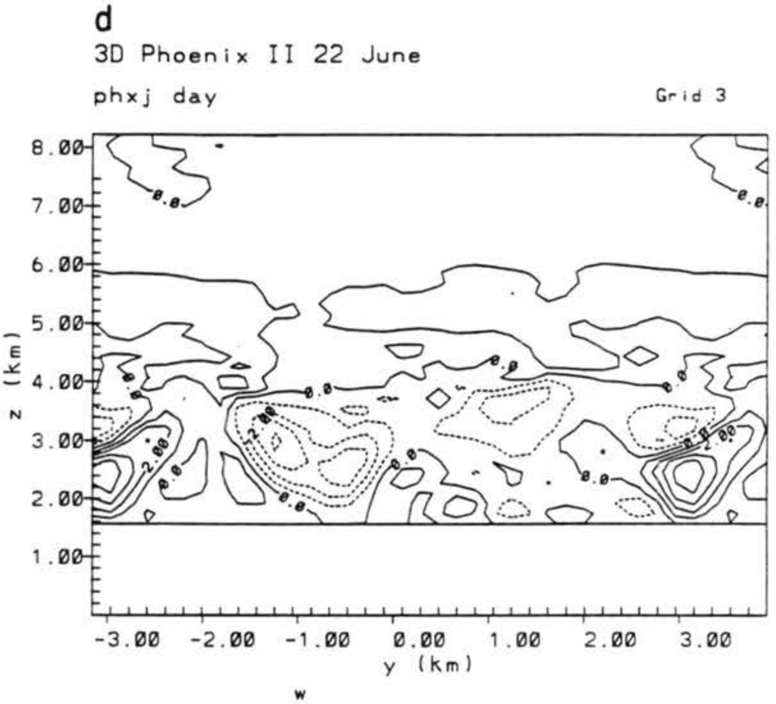


Figure 6.5: Continued.

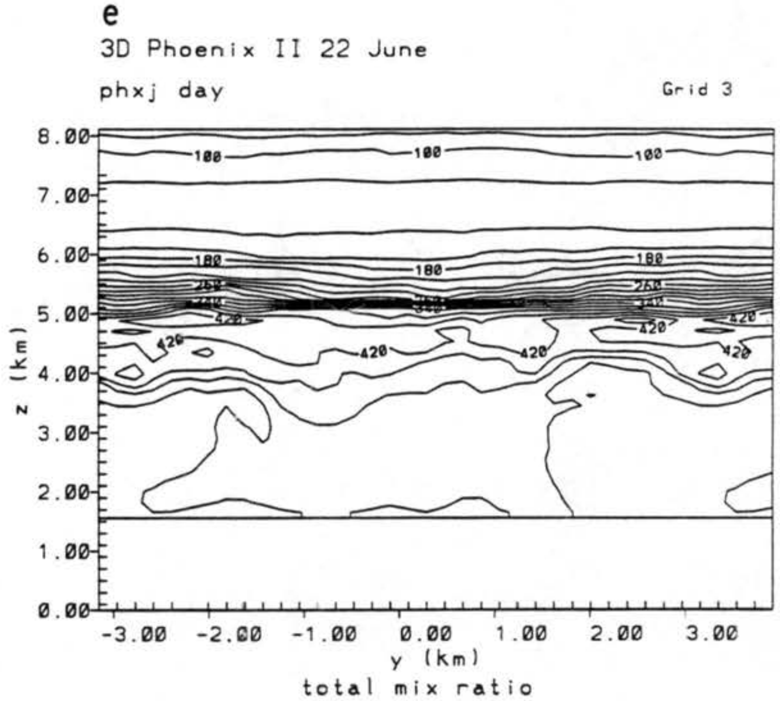


Figure 6.5: Continued.

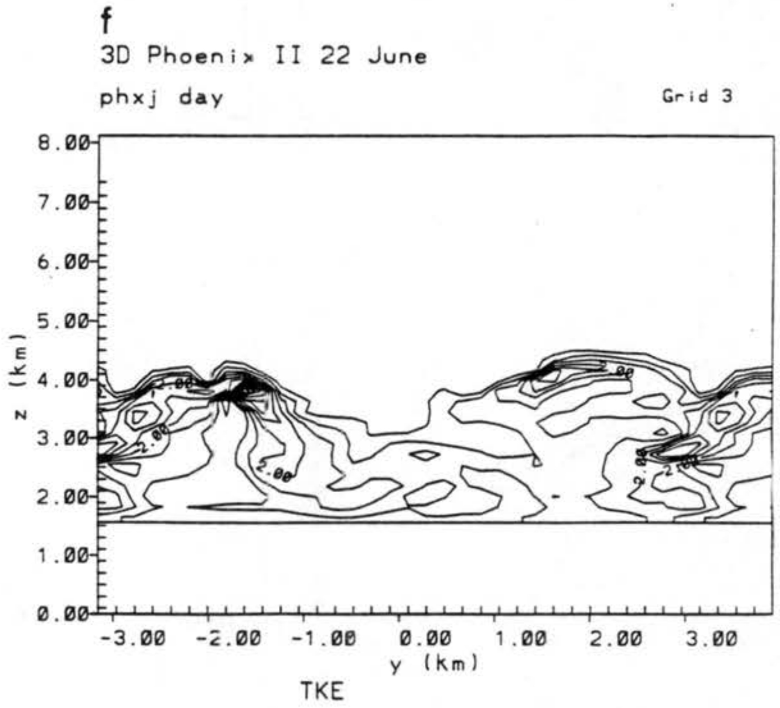


Figure 6.5: Continued.

plots are similar in both directions and only a portion of the grid is presented to give a window of similar size as the radar observations. The x-z cross sections show eddies that are comparable in size (approximately 2 km across) to the depth of the boundary layer, with smaller eddies also present. The y-z cross sections show the circulations to be more elongated in the north-south direction. This is very much what was observed on 22 June (Schneider, personal communication). It is interesting to note that Lenschow (1970) also observed with aircraft that the circulations in approximately the same area of the Colorado Front Range were longer in the north-south direction on 25 April 1968, a day when the winds were primarily from the north-northwest at about 10 $ms^{-1}$.

The mean horizontal wind fields that were observed during Phoenix II from aircraft are given in Figures 6.8 and 6.9 (from Lin, 1988) and from radar data in Figure 6.10 (from Schneider, 1991 ). The u-component of the wind consistently increases with height from light easterlies to substantial westerlies throughout the afternoon. The model predicted mean u field presented in Figure 6.11 also displays this behavior. Although the model does not predict speeds greater than 15 $ms^{-1}$ at 5 km AGL it does agree well with the radar observations for blocks I and J.

The v-component of the wind does not show as much agreement between observations and model predictions. The model displays southerly winds through the depth of the domain, with the magnitudes increasing at the level of the strong inversion. The radar and aircraft (Figure 6.9) observations indicate northerly winds at low elevations earlier in the afternoon and becoming southerly later. At upper levels the winds switch from southerly to northerly with time. Because the model does not predict these wind shifts, there is a draw back to these simulations. The differences may be due to synoptic influences, a weak cold front was approaching the area from the north on this day, or due to the lack of topographical variation in the model in the north-south direction. Neither of these effects can be captured in this simulation.

The observed mean vertical velocity profiles from the Phoenix II radar observations are presented in Figure 6.12. The largest magnitudes of the velocity are in the upper portions of the boundary layer. At these levels, confidence is low in the values because errors accumulate with height as vertical velocity is calculated from the observed horizontal

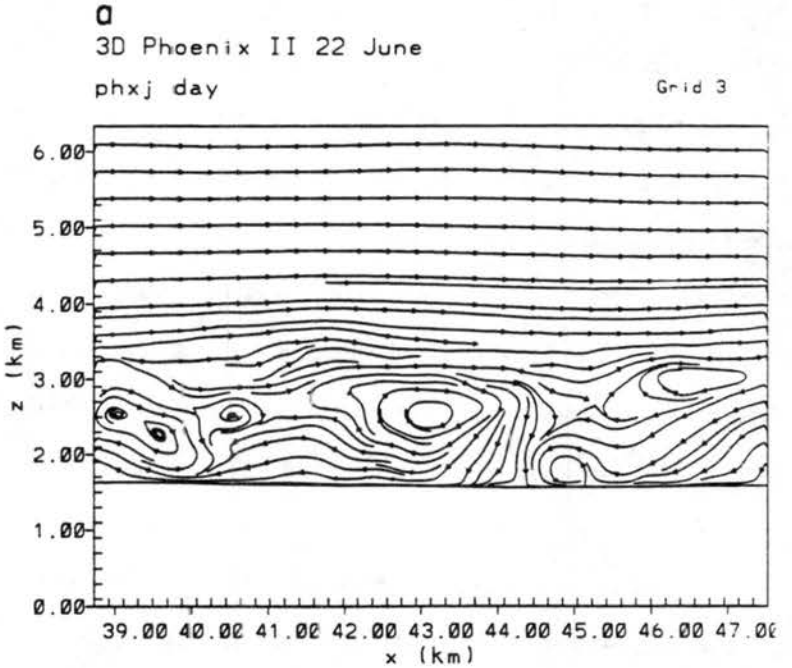


Figure 6.6: Vertical x-z (a) and y-z (b) cross sections of streamlines on the plains portion of the LES grid at 1820 UTC (1120 MST).

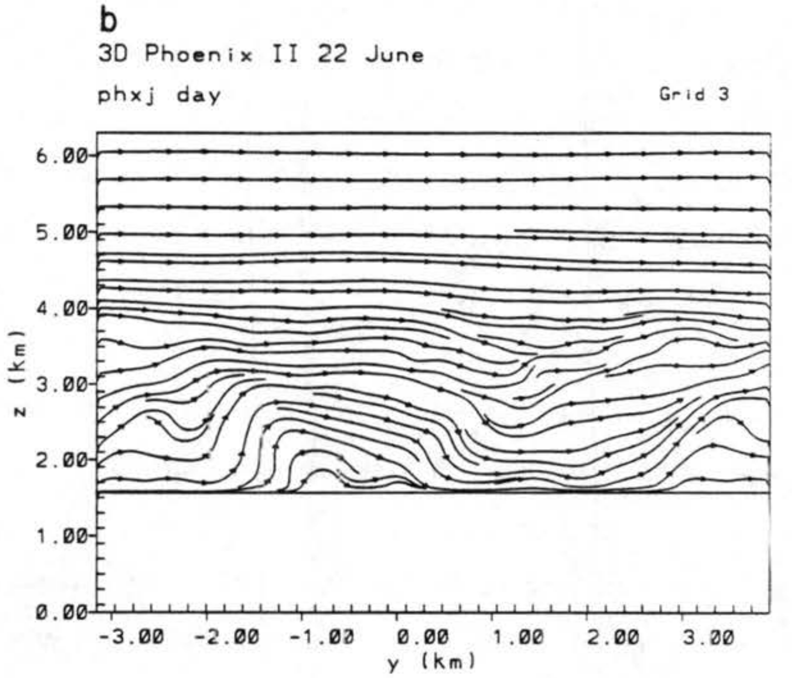


Figure 6.6: Continued.

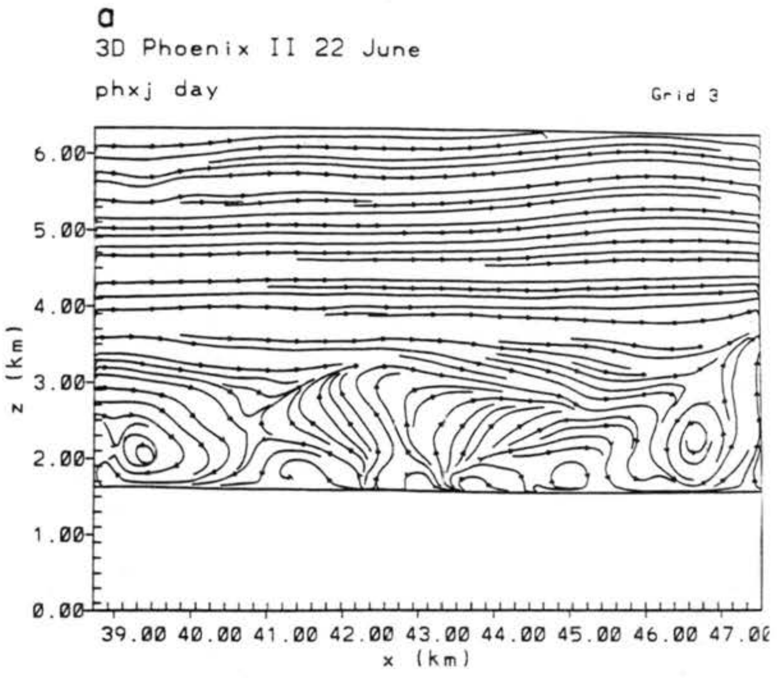


Figure 6.7: Vertical x-z (a) and y-z (b) cross sections of streamlines on the plains portion of the LES grid at 1940 UTC (1240 MST).

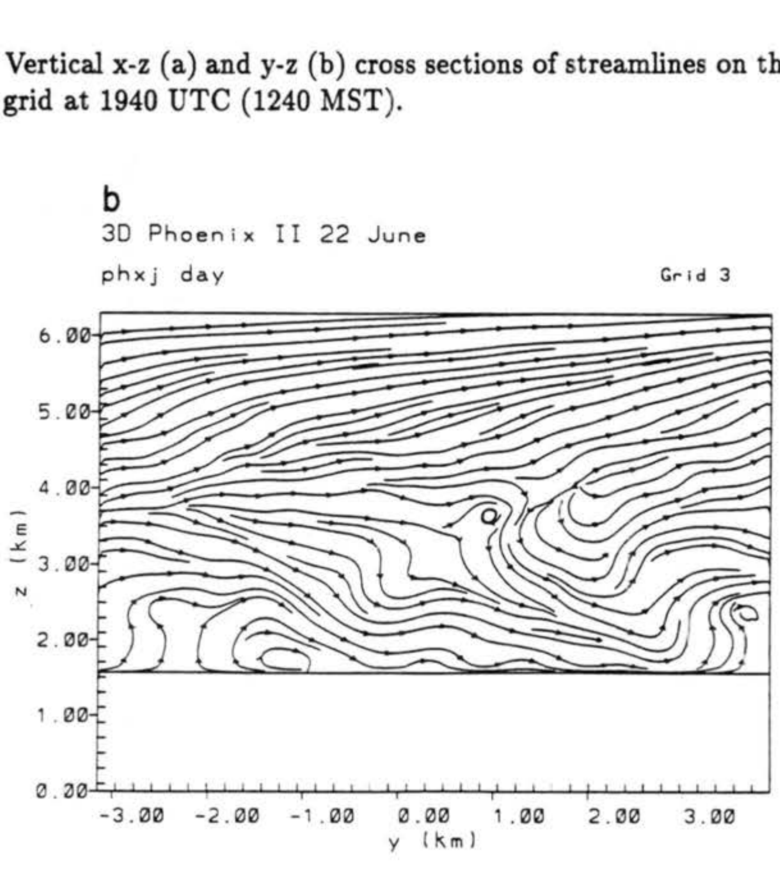


Figure 6.7: Continued.

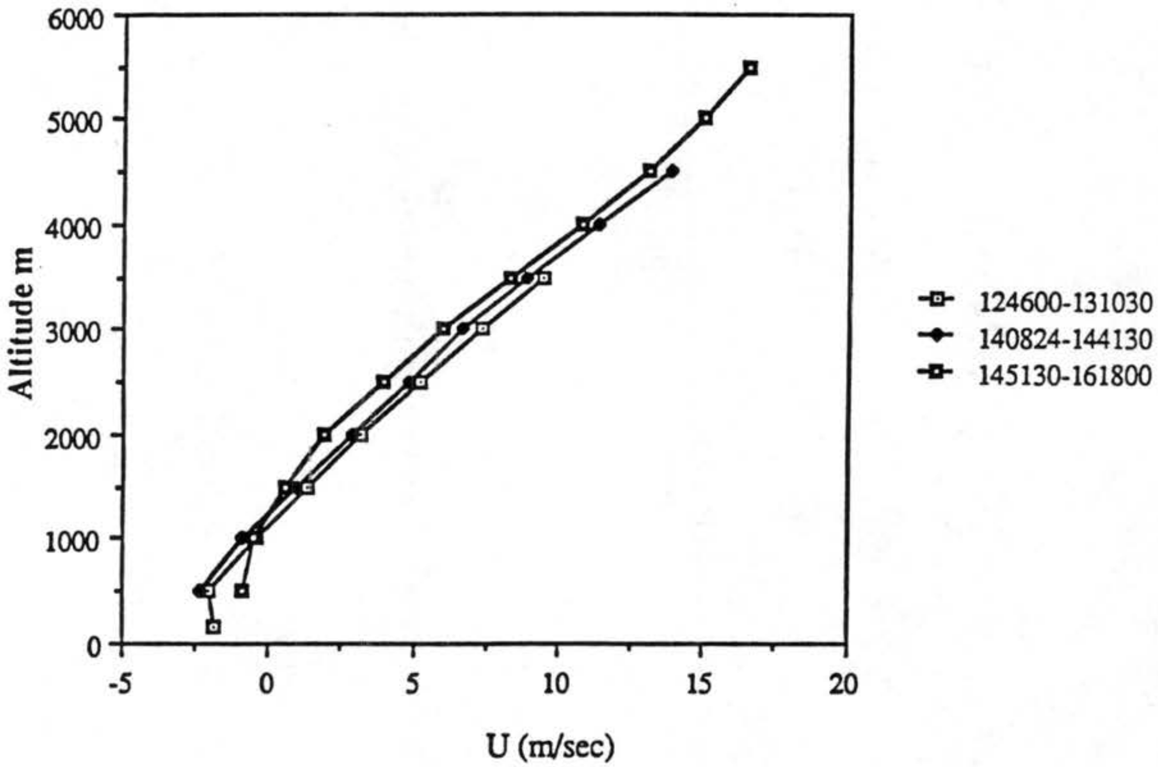


Figure 6.8: The vertical profile for u from three aircraft soundings on 22 June. From Lin (1988).

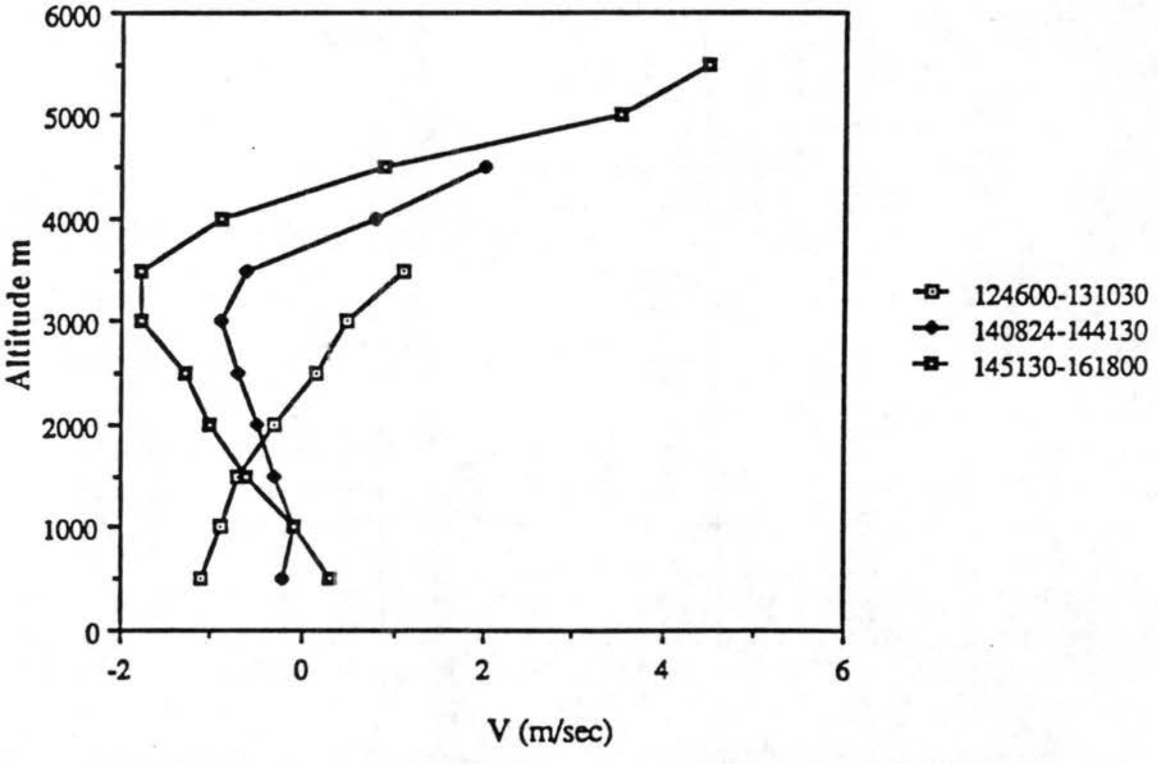


Figure 6.9: The vertical profile for v from three aircraft soundings on 22 June. From Lin (1988).

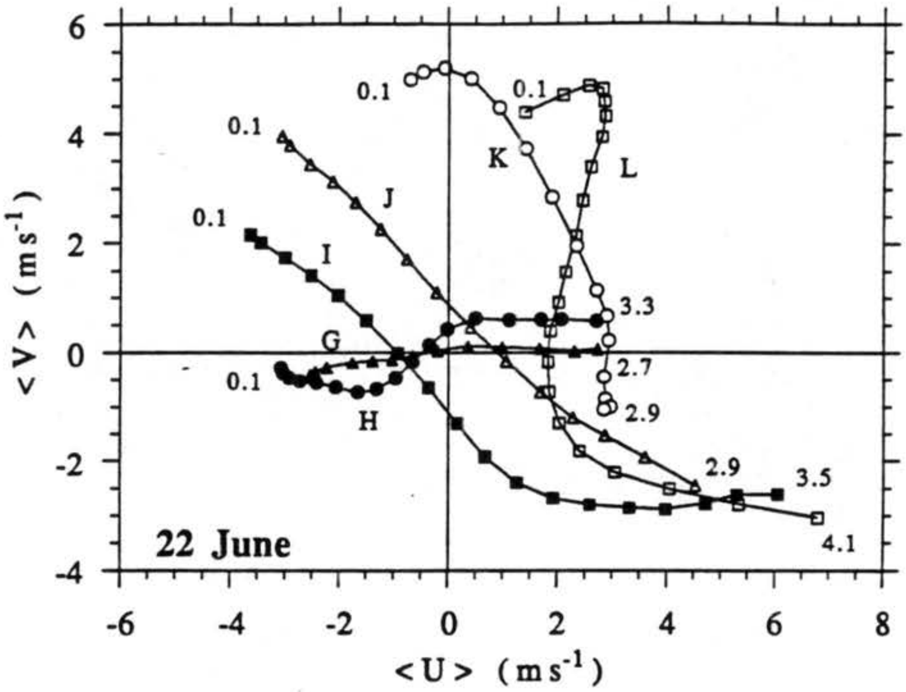


Figure 6.10: Hodographs of mean velocities from radar data. The height of the starting and ending levels are labeled in kilometers. From Schneider (1991).

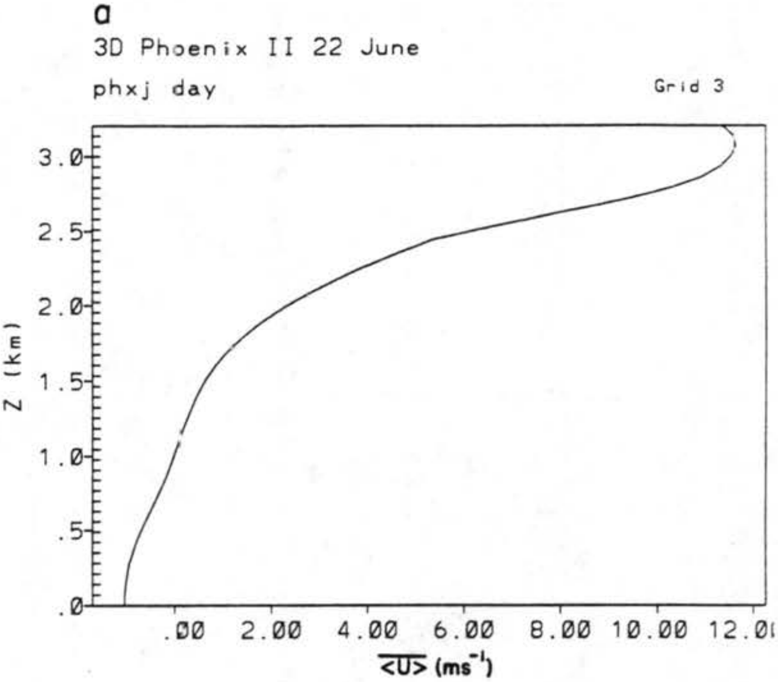


Figure 6.11: Vertical profiles of mean u-component of the wind, in meters per second, from the LES. The averaging period from 1940 to 2000 UTC (1240-1300 MST) is presented in (a), 2020 to 2040 UTC (1320-1340 MST) in (b), 2120 to 2140 UTC (1420-1440 MST) in (c), 2220 to 2240 UTC (1520-1540 MST) in (d), and 2300 to 2330 UTC (1600-1620 MST) in (e).

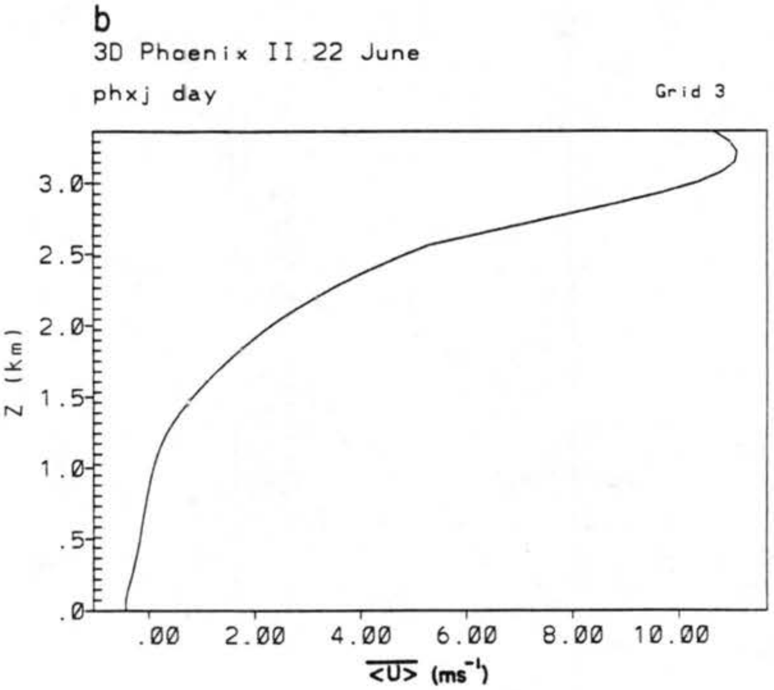


Figure 6.11: Continued.

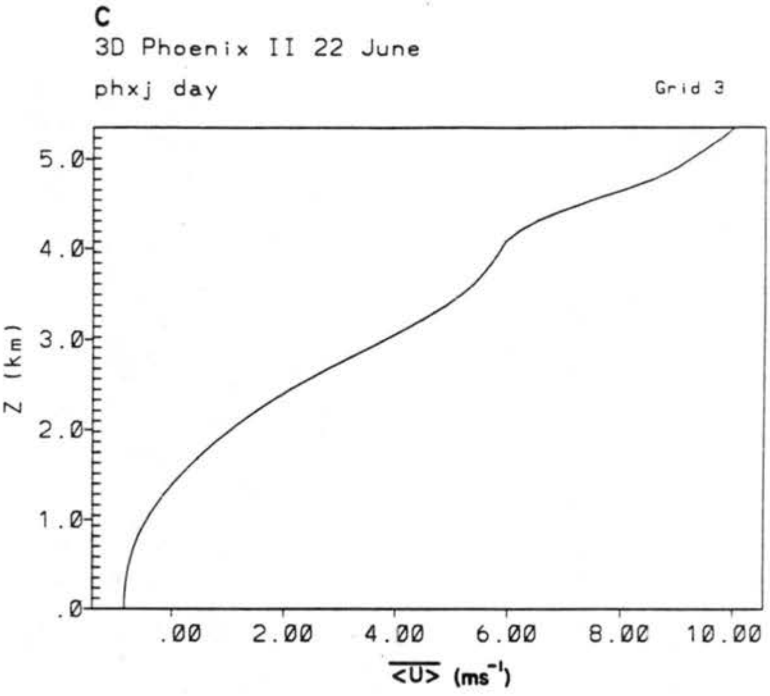


Figure 6.11: Continued.

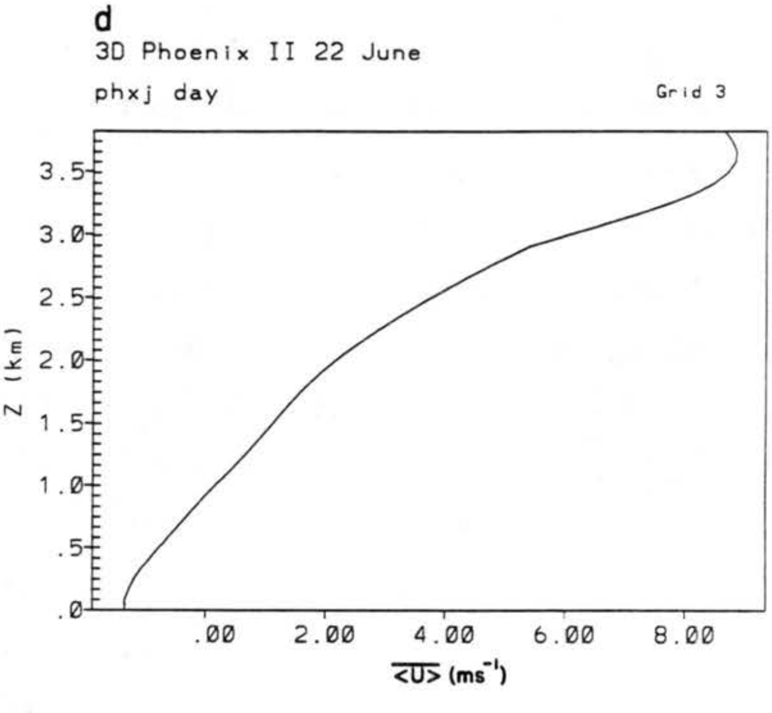


Figure 6.11: Continued.

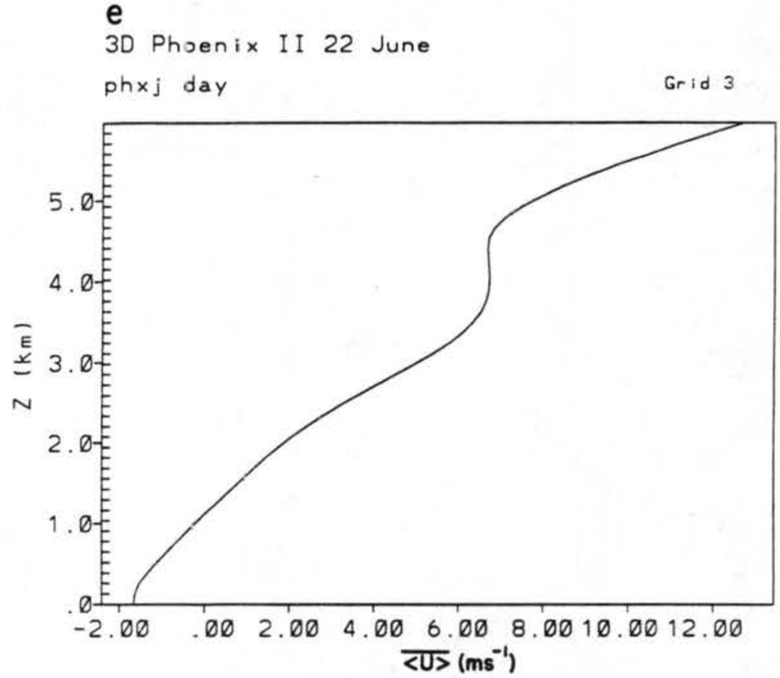


Figure 6.11: Continued.

wind fields. In the lower half of the boundary layer, the mean vertical velocity is positive and has magnitudes of a few tenths $ms^{-1}$. Later in the afternoon, there is mean sinking motion instead. The model-predicted mean vertical velocity is given in Figure 6.13. The first and last time periods, where the results are averaged from 1940 to 2000 UTC and 2300 to 2320 UTC, are the only times where there is positive vertical motion and just in the lower half of the plains boundary layer in the first time period. The magnitudes of the mean vertical velocity predicted by the model are quite a bit smaller, generally less than 0.1 $ms^{-1}$. Both observations and model results indicate that the mean vertical motion is not necessarily zero at the top of the boundary layer.

The mean potential temperature profiles show the development of the plains boundary layer with time. The aircraft plots of potential temperature are presented in Figure 6.14 and model- predicted potential temperature is in Figure 6.15. Heating progresses similarly in both the aircraft observations and the model results. One notable feature of these profiles is the lack of a strong capping inversion on the plains boundary layer.

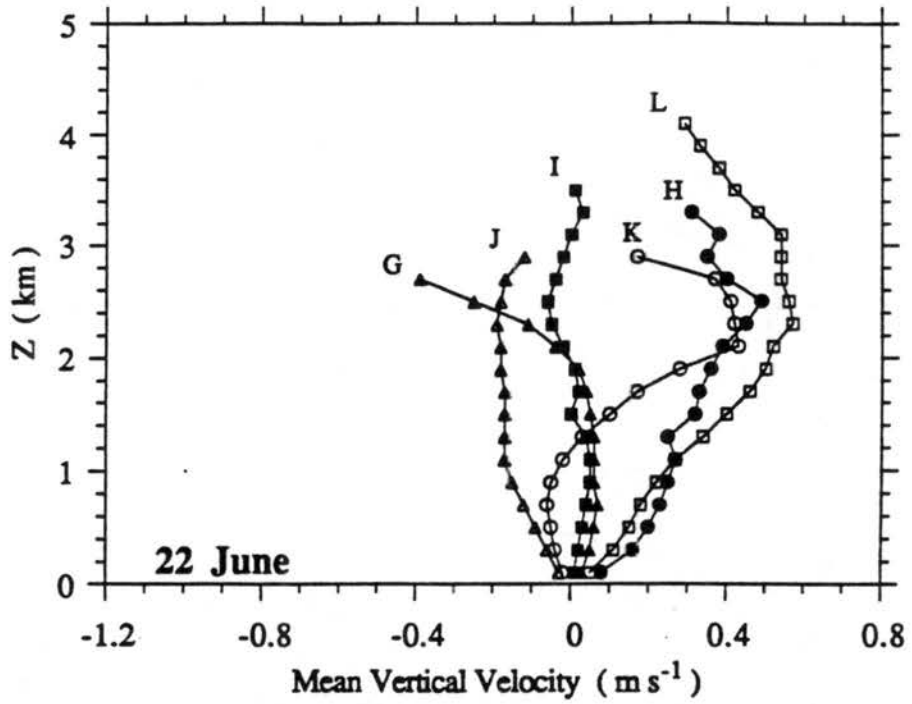


Figure 6.12: Vertical profiles of mean vertical velocity from the radar data. From Schneider (1991).

This is particularly so in the model results. Because the radar does not observe potential temperature directly, and because the precise height of the weak inversion was difficult to ascertain, Schneider (1991) used the height to which released chaff mixed as a determiner of boundary layer height (Figure 6.16). This method showed a significant variability with time of the boundary layer height. This is not surprising given the limited area of the dual Doppler observations. Only a few eddies are captured in these observations and do not necessarily represent the entire boundary layer. Noting the undulatory nature of the plains capping inversion (Figure 6.4), a true mean boundary layer height iis understandably difficult to obtain.

Figure 6.17 compares the estimated depth of the plains boundary layer for the two-dimensional run, the three-dimensional channel simulation, and the radar observations at times throughout the day. It should be stressed that these estimates are approximate. The values obtained for the radar estimates are based on Figure 6.16 of Schneider (1991) and are plotted at the middle of the time averaging period. She states that, in the

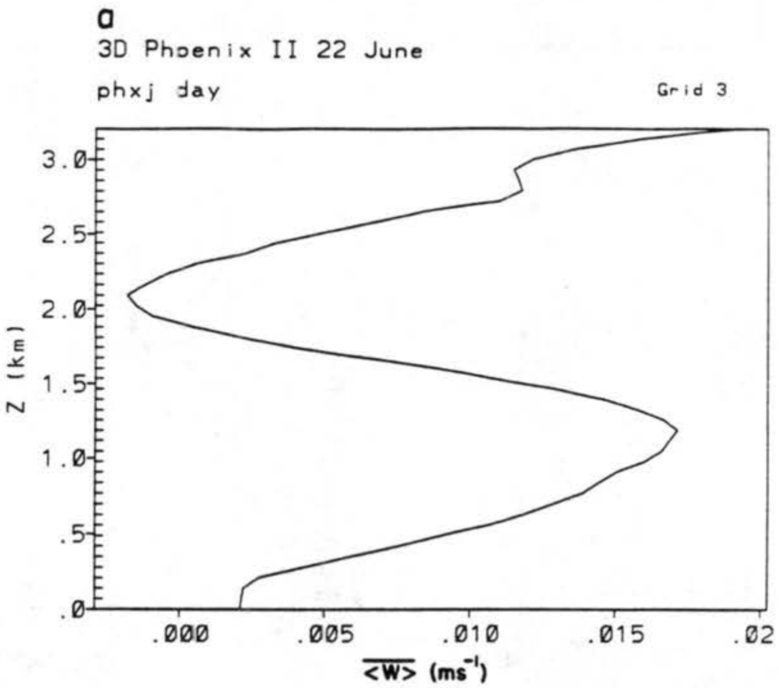


**Figure 6.13: Vertical profiles of mean vertical velocity, in meters per second, from the LES. The averaging period from 1940 to 2000 UTC (1240-1300 MST) is presented in (a), 2020 to 2040 UTC (1320-1340 MST) in (b), 2120 to 2140 UTC (1420-1440 MST) in (c), 2220 to 2240 UTC (1520-1540 MST) in (d), and 2300 to 2330 UTC (1600-1620 MST) in (e).**

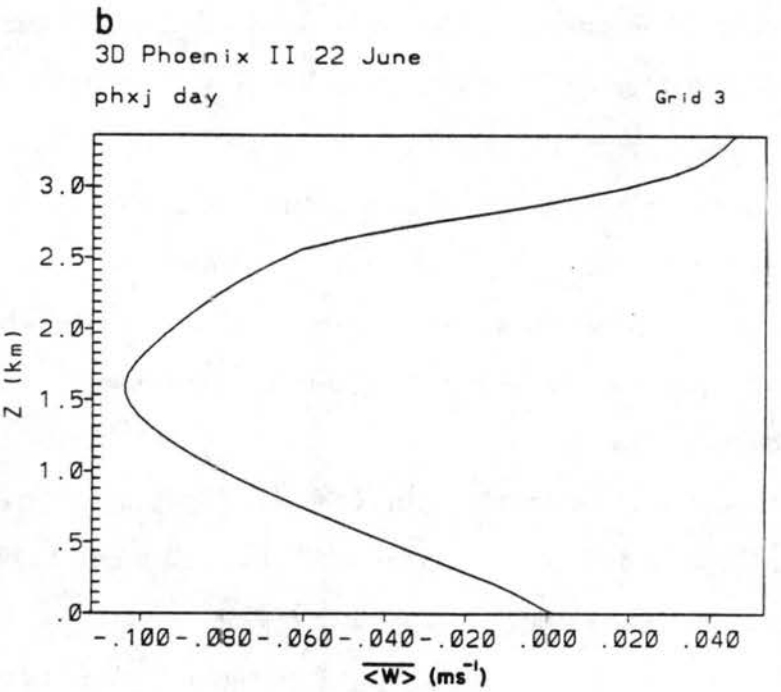


Figure 6.13: Continued.

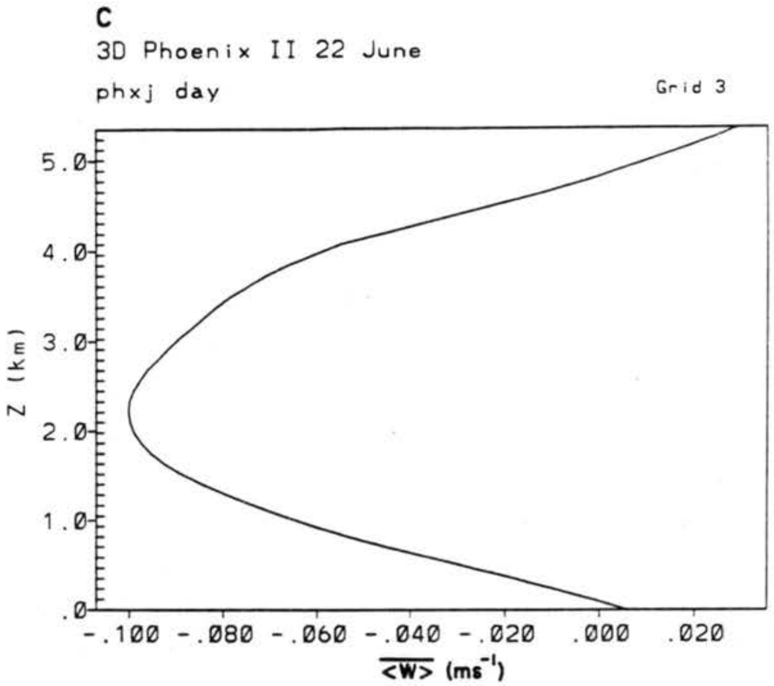


Figure 6.13: Continued.

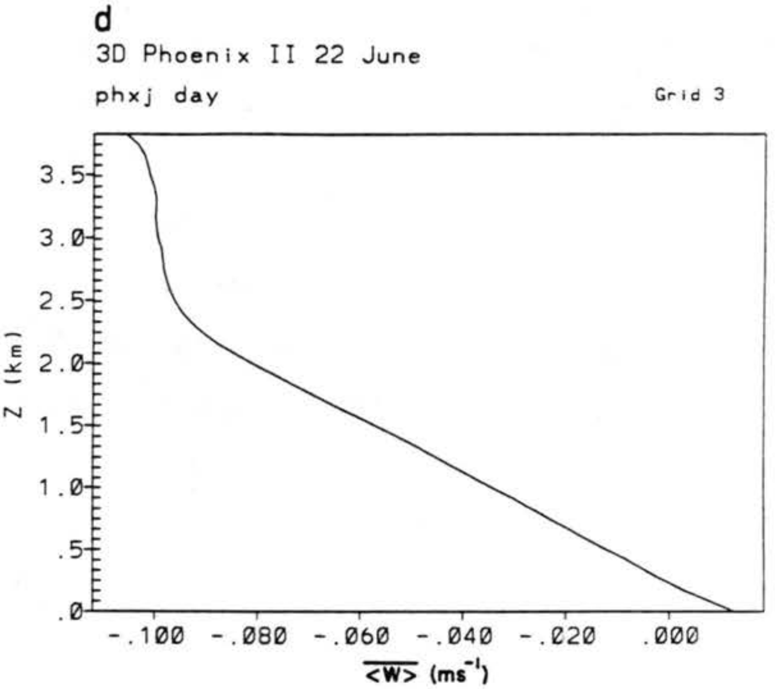


Figure 6.13: Continued.

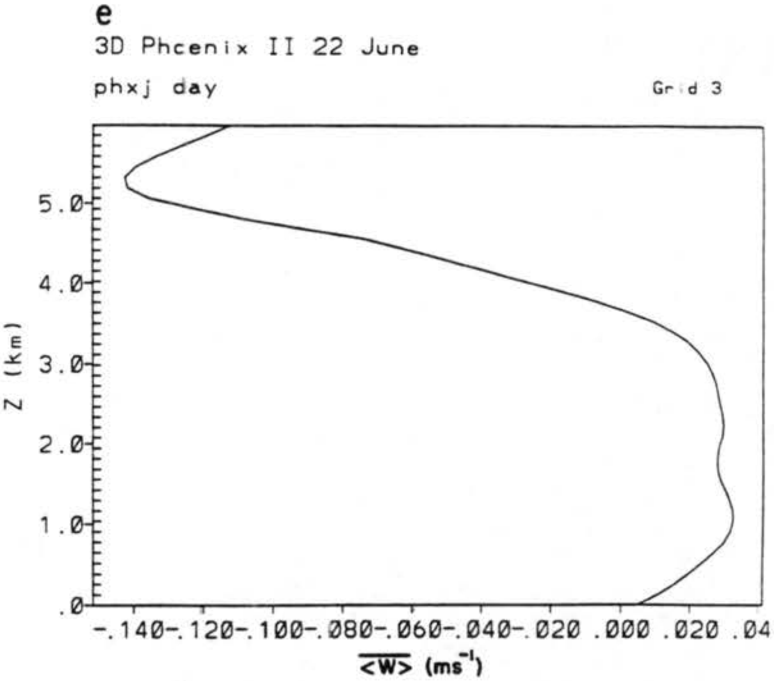


Figure 6.13: Continued.

upper levels, a sudden decrease in points with height indicates the top of the mixed layer. Figure 6.16 is a mean measure in both time and space and the actual upper chaff surface was deeply convoluted (by as much as a kilometer) and varied over the block duration. The values for the three-dimensional simulation are obtained by finding the local minimum in heat flux for the plains boundary layer at that particular time. The two-dimensional simulation did not include calculation of statistics and the estimates of boundary layer depth are subjectively determined from plots of the potential temperature field. The model boundary layer depth for both runs also varied considerably in time and space.

The heights predicted by the three-dimensional channel simulation agree well with observations until later in the afternoon, when both show a great deal of variability. The dramatic difference between the two-dimensional and three-dimensional runs is evident in the late morning. The plains boundary layer of the two-dimensional simulation grows quickly and merges with the mountain boundary layer by late morning. In the

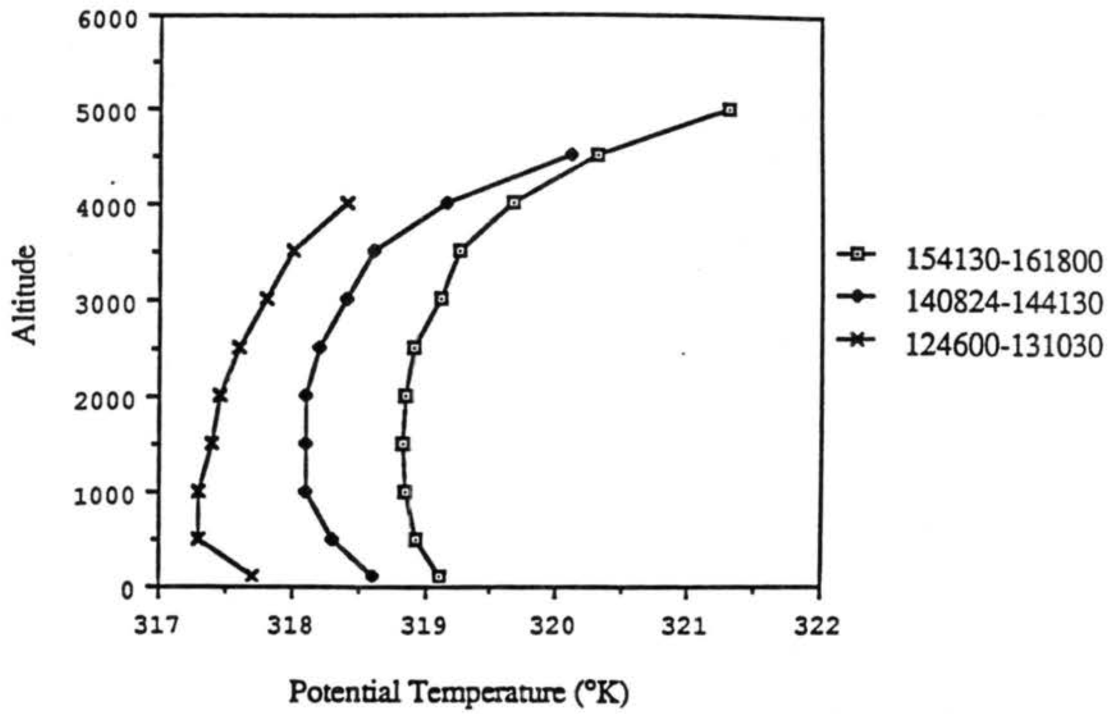


Figure 6.14: Vertical profiles of potential temperature from aircraft soundings for 22 June. From Lin (1988).

three-dimensional simulation, the two boundary layers interact intermittently but do not completely merge.

### 6.1.3 Comparisons to LES of the horizontally homogeneous boundary layer

Some of the gross features described in the previous sections are not found in the horizontally homogeneous, free convection LES. Because such LES simulations simulate the purely convective boundary layer, wind shear and ambient winds are expected to be weak, along with mean vertical velocity. Also, the boundary layer depth in most of these runs is assumed to be at a relatively steady state so that growth of the boundary layer is ignored. The potential temperature profile of the horizontally homogeneous LES simulation typically represents a mean neutral stability through the depth of the boundary layer, as described above for Phoenix II observations and the model results, but the capping inversion is defined to be significantly stronger and its position is more distinctive.

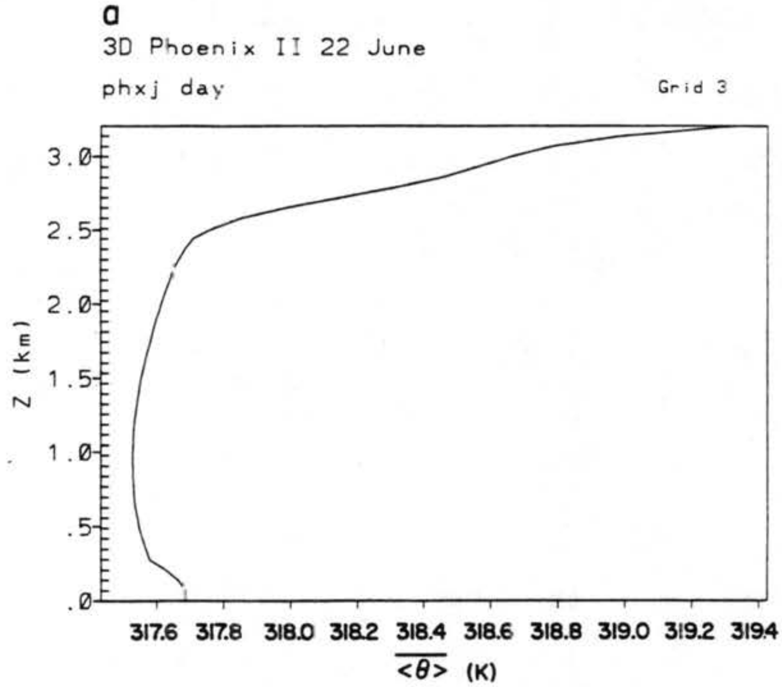


Figure 6.15: Vertical profiles of mean potential temperature, in degrees K, from the LES. The averaging period from 1940 to 2000 UTC (1240-1300 MST) is presented in (a), 2020 to 2040 UTC (1320-1340 MST) in (b), 2120 to 2140 UTC (1420-1440 MST) in (c), 2220 to 2240 UTC (1520-1540 MST) in (d), and 2300 to 2330 UTC (1600-1620 MST) in (e).

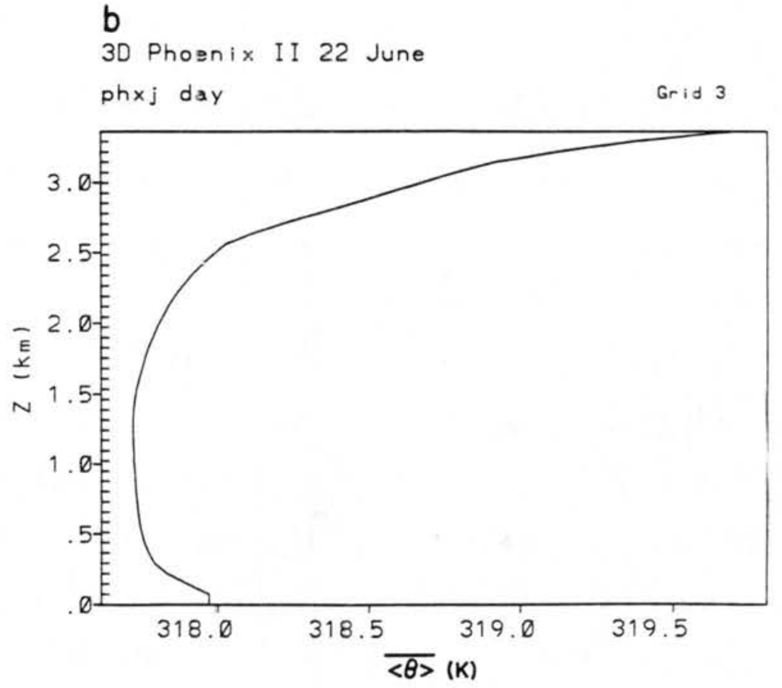


Figure 6.15: Continued.

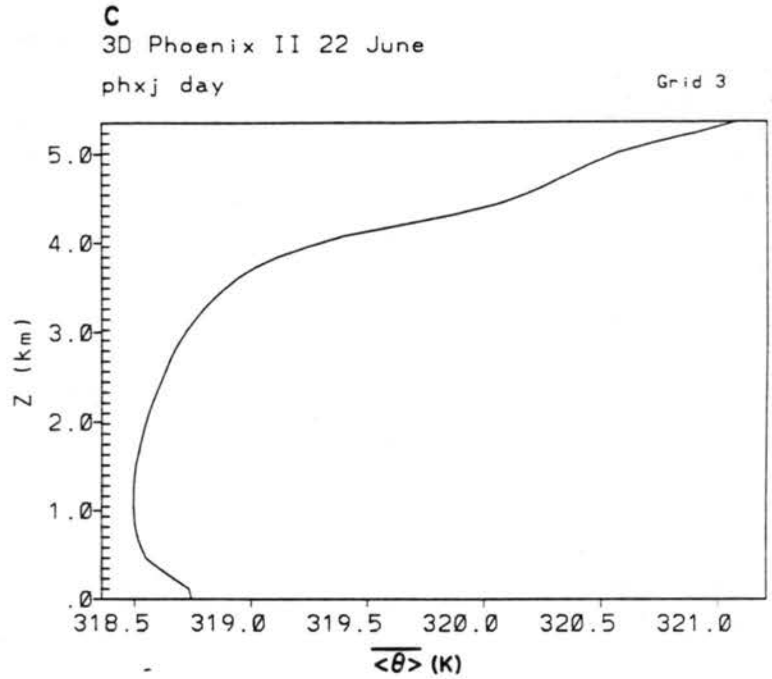


Figure 6.15: Continued.

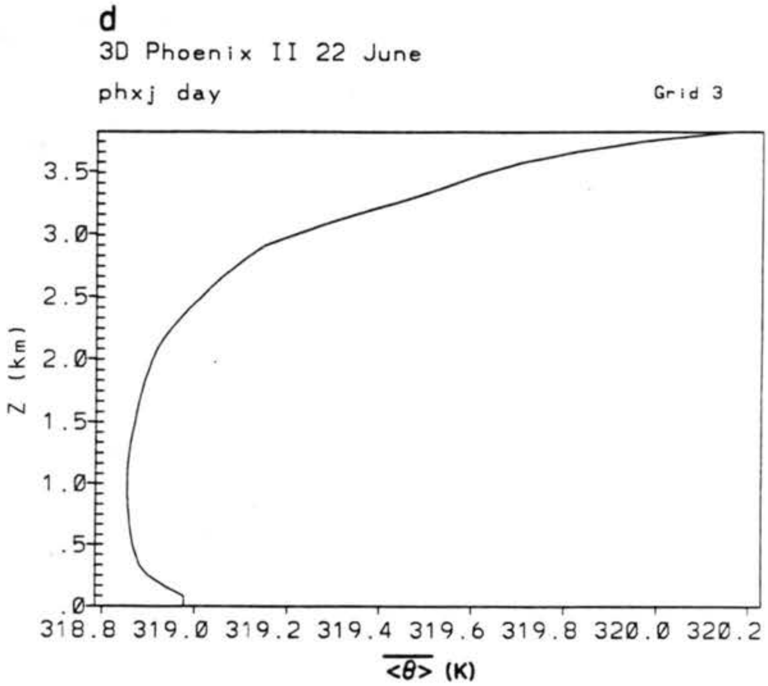


Figure 6.15: Continued.

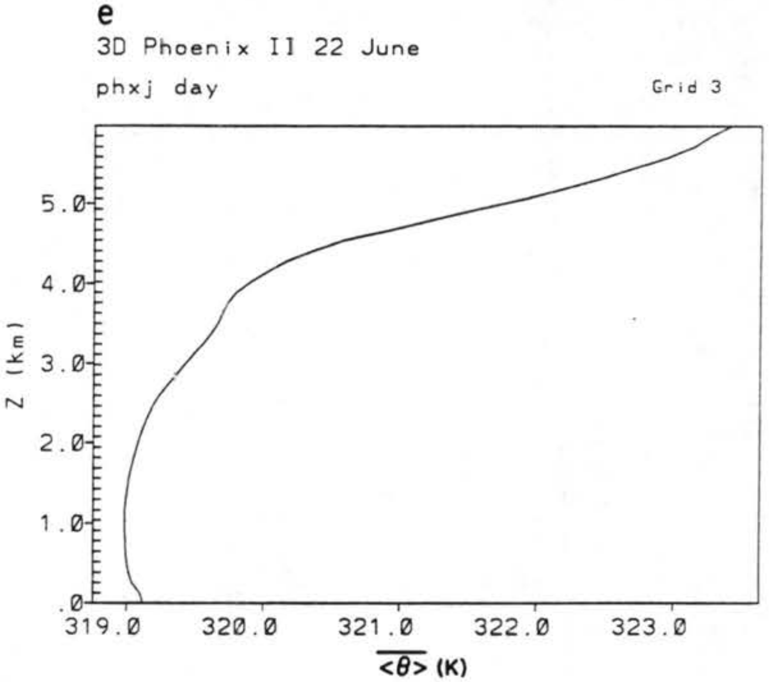


Figure 6.15: Continued.

One way that the general flow of the three-dimensional simulation can be compared to LES simulations of the horizontally homogeneous boundary layer is with horizontal cross sections of the vertical motion field. Figures 6.18 and 6.19 present these cross sections at 2000 UTC (1300 MST) and 2140 UTC (1440 MST) for the LES grid 100, 1100, and 2700 m AGL, representing the near surface, midlevel, and near boundary layer top. The 2700 m level is just above the boundary layer top at 2000 UTC when the boundary layer depth is about 2400 m and at about the boundary layer top at 2140 UTC when the boundary depth is about 2700 m. They can be compared to Figure 2.7 of Schmidt and Schumann (1989) for LES of a horizontally homogeneous boundary layer. In both cases, the size of the circulations becomes larger with height. Numerous small updrafts are present at the lower levels, with fewer and the strongest updrafts at midlevels. Wide areas of downdrafts are present near the top of the plains boundary layer. However, the polygonal pattern in the lower levels of Figure 2.7 are difficult to find, consistent with the work of Sykes and Henn (1989) for sheared convective flow. The patterns are instead elongated in the north-south direction.

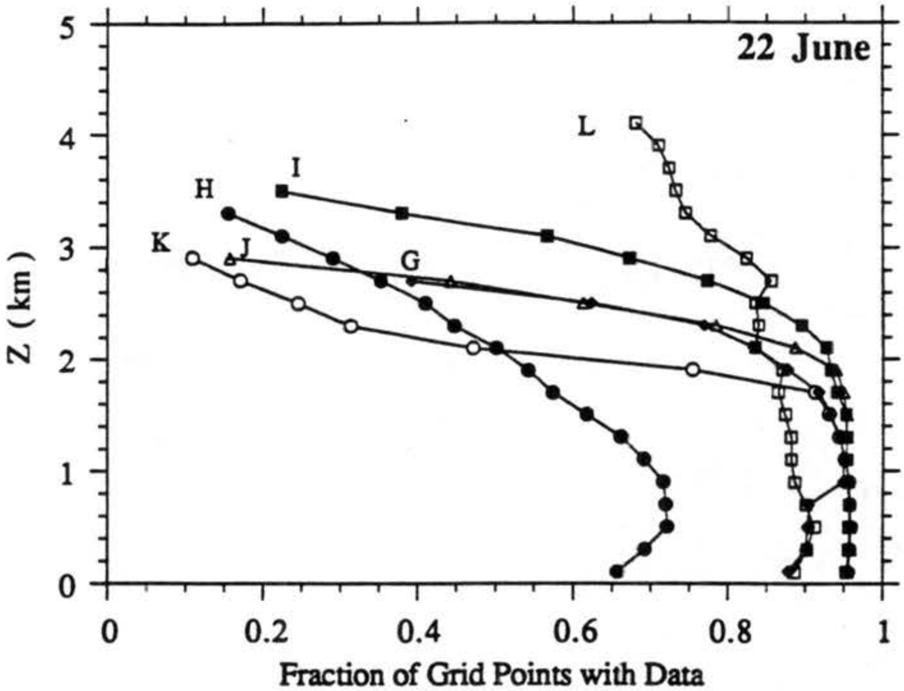


Figure 6.16: Vertical profiles of density of radar data across the afternoon of 22 June, as a fraction of the grid points available. There are 2116 grid points defined at each level. Time periods of each block are defined in Table I. From Schneider (1991).

### 6.2 Turbulence Statistics

As described in Section 6.1.2, fields are averaged horizontally over the flat portion of the LES domain (x grid points 54 through 242) and are then averaged over 20 minute sections of time. In this study, the notation of an overbar will represent a time average and a tilde will represent departures from the mean. A variable $a$ at any time would be

$$a = \overline{a} + \tilde{a}.$$

To represent a spatial average, a bracket is used with a prime mark used to denote departures from the horizontal average. A variable $b$ at any point would be

$$b = < b > + b'.$$

In 6.1.2, the profiles of $\overline{< \theta >}$, $\overline{< u >}$, and $\overline{< w >}$ were presented. This section will primarily be concerned with the turbulent statistics $\overline{< w'\theta' >}$, $\overline{< u'u' >}$, $\overline{< v'v' >}$, $\overline{< w'w' >}$,

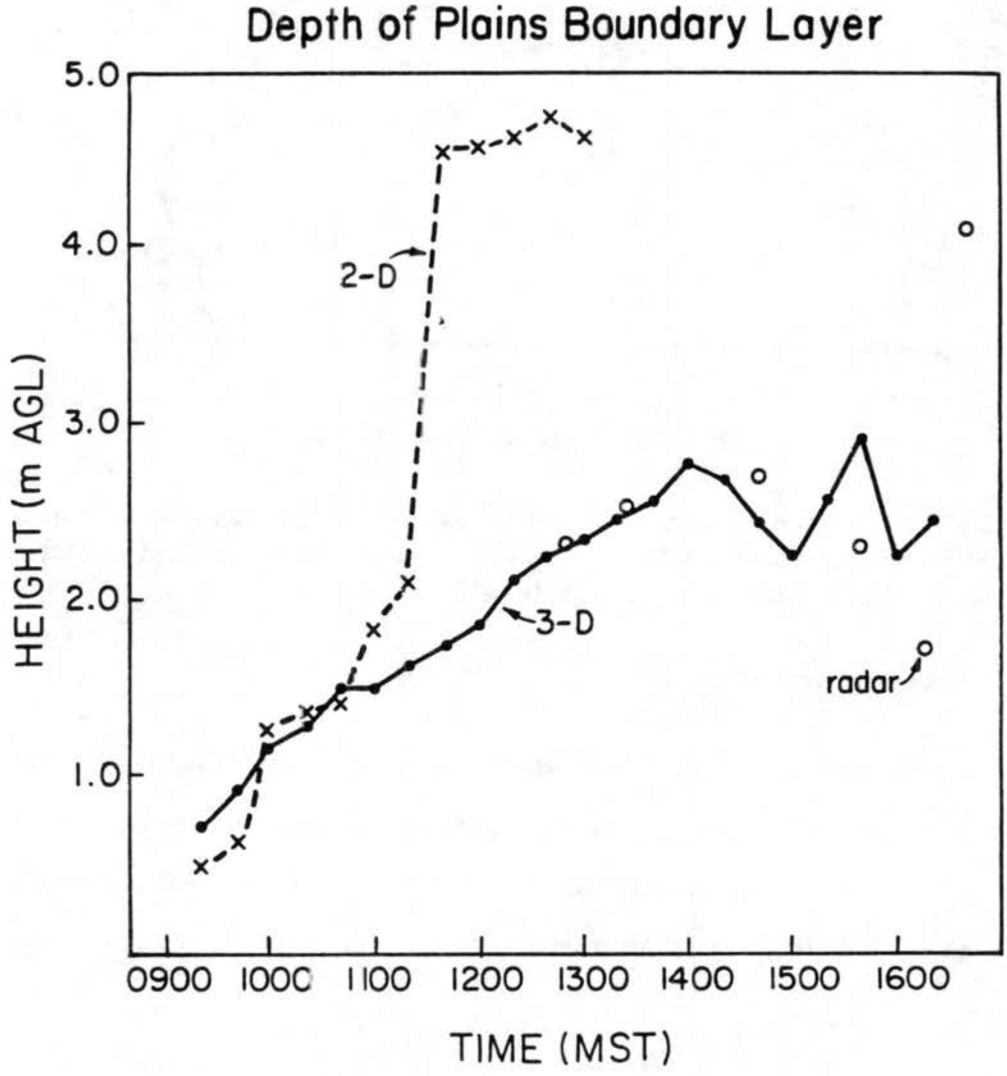


Figure 6.17: Plains boundary layer depth with time determined from the three-dimensional simulation (solid line), the two-dimensional simulation (dashed line), and the radar observations (circles).

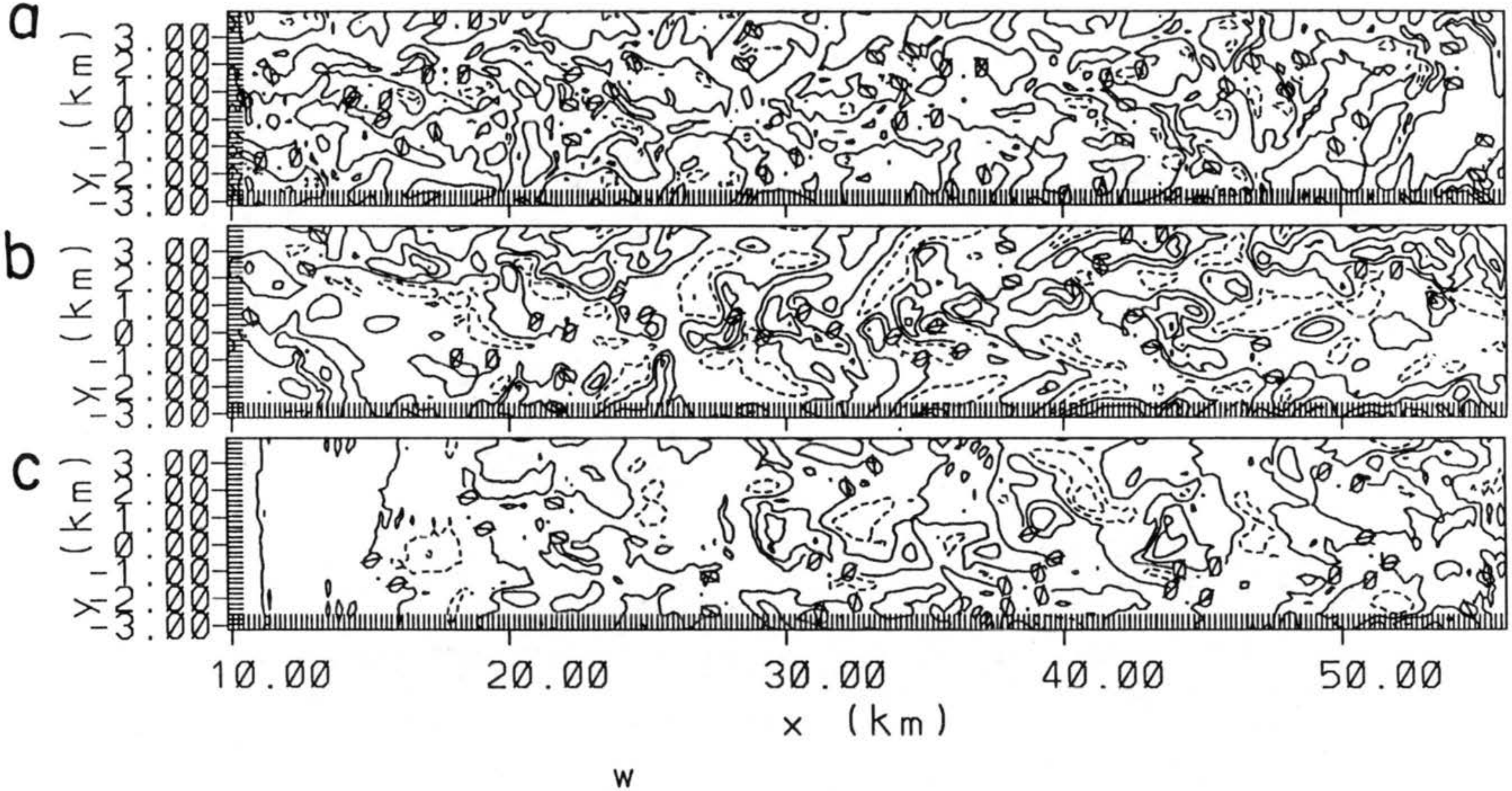


**Figure 6.18: Horizontal cross sections of the vertical velocity field on the LES grid at 2000 UTC (1300 MST). The surface 100 m AGL is presented in (a), 1100 m AGL in (b), and 2700 m AGL in (c).**

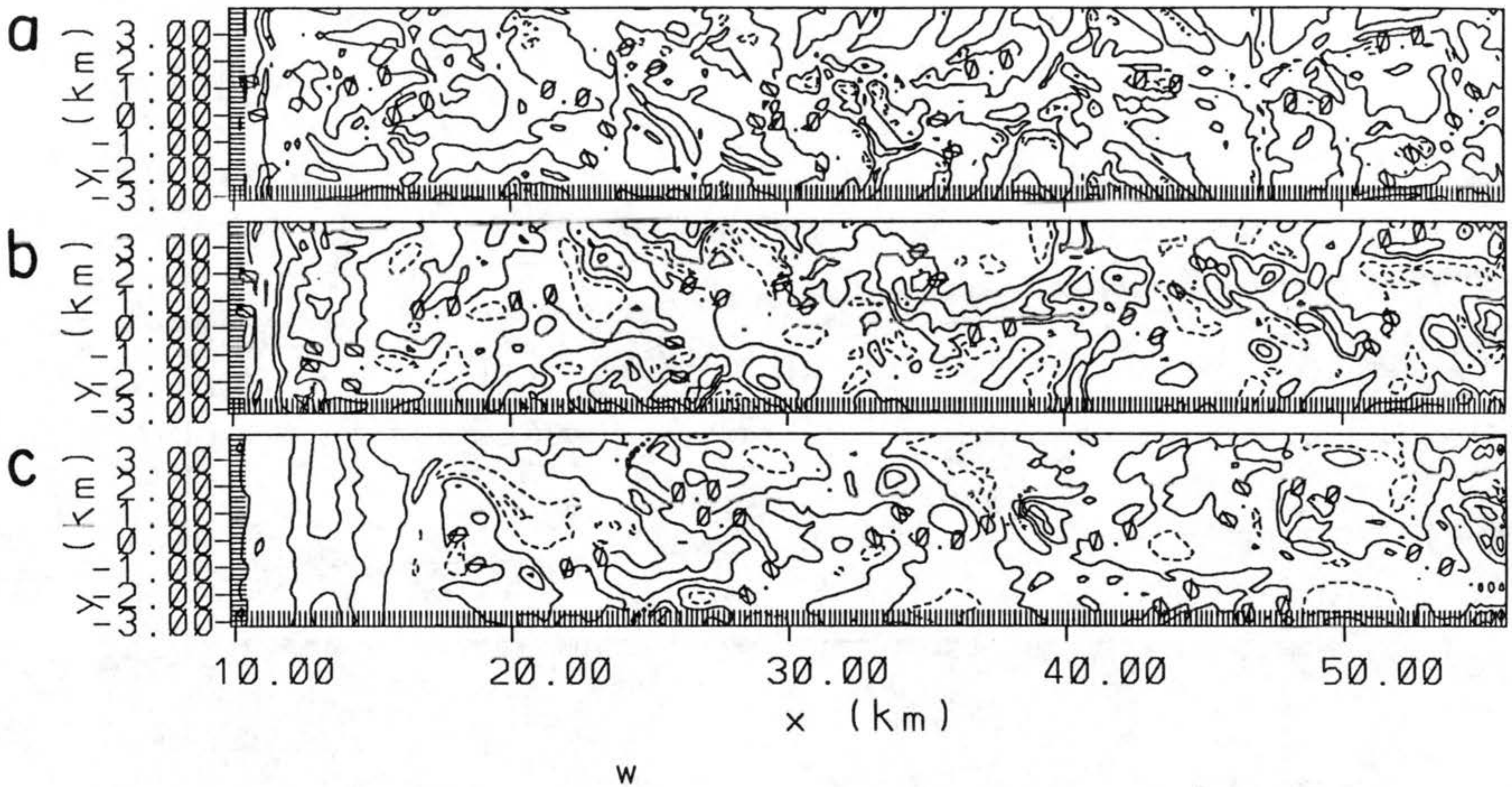


**Figure 6.19: Horizontal cross sections of the vertical velocity field on the LES grid at 2140 UTC (1440 MST). The surface 100 m AGL is presented in (a), 1100 m AGL in (b), and 2700 m AGL in (c).**

$\overline{<\theta'\theta'>}$, $\overline{<u'w'>}$, and $\overline{\frac{<w'^3>}{<w'^2>^{\frac{3}{2}}}}$. These calculations are performed over the depth of the plains boundary layer. The approximate boundary layer depth determined by the model is found as the height where the heat flux $\overline{<w'\theta'>}$ is minimum. This is the method adopted by previous studies using LES (i.e. Hadfield, 1988 and Walko et al. (1992).

The figures that present the model results are not scaled using mixed layer similarity. With the wind shear present on 22 June 1984, the assumption used in mixed layer scaling that buoyant forces dominate the production of energy is not valid. And, as pointed out by Schneider (1991), the precise determination of the boundary layer top, $z_i$, is not possible on this day. This non-scaled presentation of the model results facilitates the comparison of model results to the Phoenix II observations, which are also not scaled, but will take some interpretation when comparing to plots of LES results for the horizontally homogeneous boundary layer, which are scaled.

### 6.2.1 Comparisons to Phoenix II observations

This description will begin by looking at the heat flux profiles because they are used to determine the approximate depth of the boundary layer. Relative height references will be made to the boundary layer top. Schneider (1991) does not present heat flux, $\overline{<w'\theta'>}$, but gives profiles of buoyancy flux $\overline{\frac{g}{\theta_0}<w'\theta'>}$ in Figure 6.20. Moisture effects on $\theta_v$ are not included in this analysis. The largest values of the buoyancy flux were observed earlier in the afternoon. Only block K exhibits the expected linear decrease of buoyancy flux with height, with the other times showing elevated maxima. Schneider (1991) attributes this to the radar sampling architecture and the spatial filtering that she uses. These characteristics of the radar effectively mean that the radar data cannot resolve the heat flux near the surface. Figure 6.21 gives the resolved heat flux predicted by the nested grid LES. The model results are more like the expected linear decrease of heat flux with height. The maximum is elevated due to the model's inability to resolve the smallest scales (including subgrid heat flux would bring the maximum down to the surface) but the level of the maximum is lower in the model results and is consistently below 0.5 km throughout the afternoon.

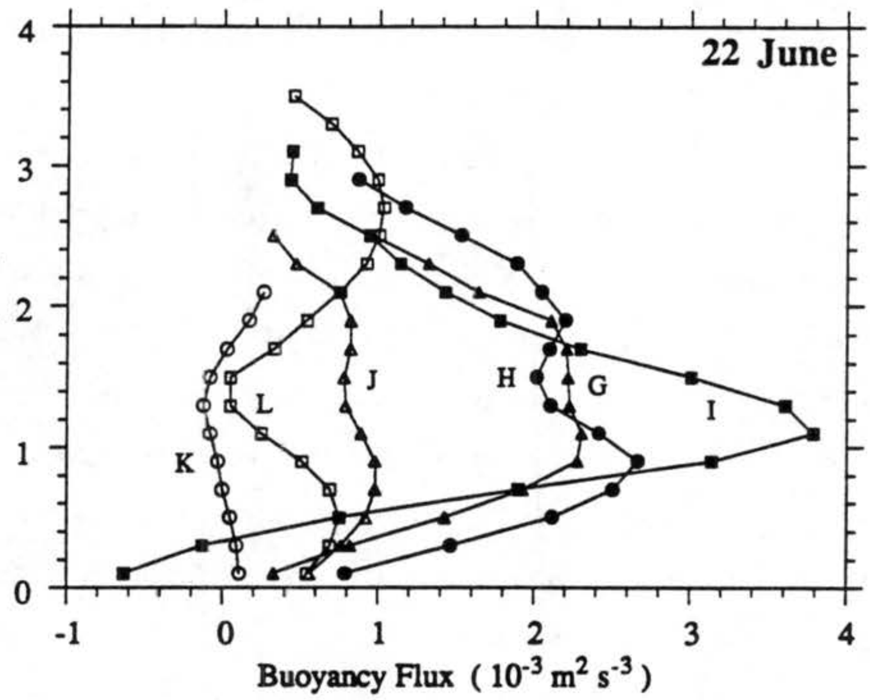


Figure 6.20: Vertical profiles of Buoyancy flux recovered from the radar data. Block times are defined in Table I. From Schneider (1991).

The observations indicate that the buoyancy flux reaches a minimum near the highest data levels (the heights to which the chaff has mixed and the estimated height of the boundary layer top). The top of the plains boundary layer is not always obvious in the model results also. In the first few averaging periods, a definite minimum in the heat flux profile can be seen at 2.4 km and 2.6 km, but there are hints of other local minima at higher altitudes. By 2140 UTC (1440 MST), the upper level minimum is the absolute minimum and dominates, with only a hint of a local minimum at the plains boundary layer top. The higher level minima are associated with the upper level boundary layer.

The variance of the horizontal and vertical velocities from the Phoenix II radar observations are given in Figure 6.22 for one time period. Summing the curves in the top plot will give the same parameter that would be obtained by summing the curves in Figures 6.23 and 6.24. Summing the curves in the bottom plot gives the curve in Figure 6.25. At the time period ending at 2000 UTC (1300 MST), the time corresponding to block G of the radar data, both observations and LES results give a maximum in the horizontal

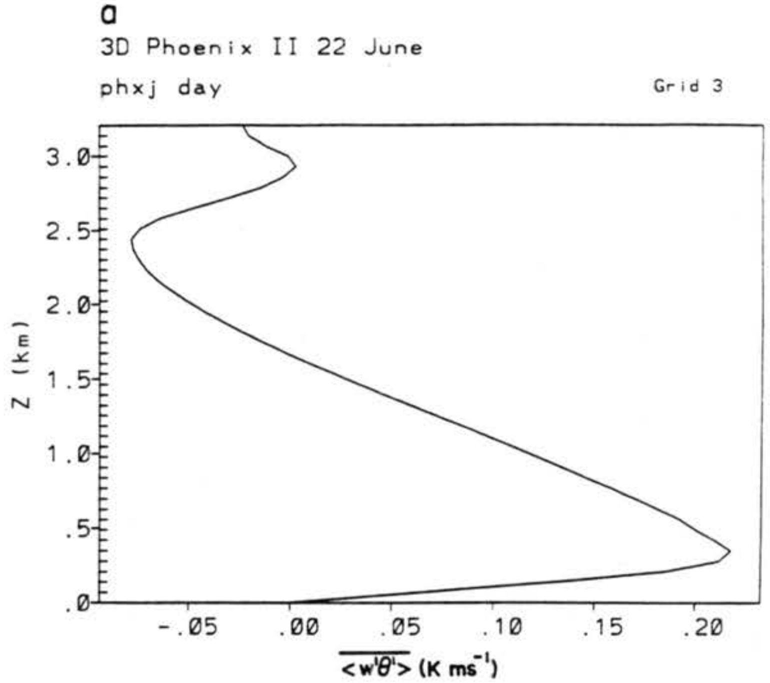


Figure 6.21: Vertical profiles of heat flux $\overline{< w'\theta' >}$, in degrees K meters per second, from the LES. The averaging period from 1940 to 2000 UTC (1240-1300 MST) is presented in (a), 2020 to 2040 UTC (1320-1340 MST) in (b), 2120 to 2140 UTC (1420-1440 MST) in (c), 2220 to 2240 UTC (1520-1540 MST) in (d), and 2300 to 2330 UTC (1600-1620 MST) in (e).

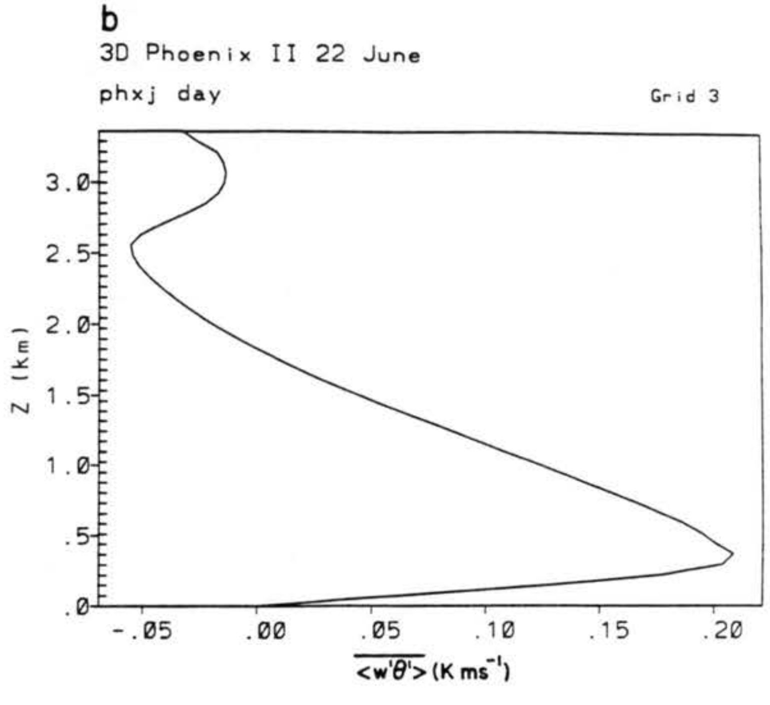


Figure 6.21: Continued.

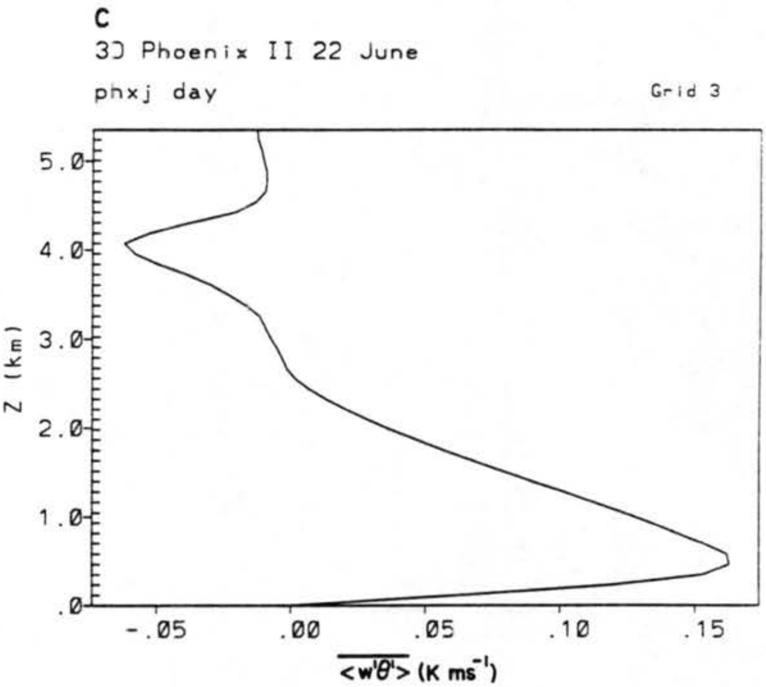


Figure 6.21: Continued.

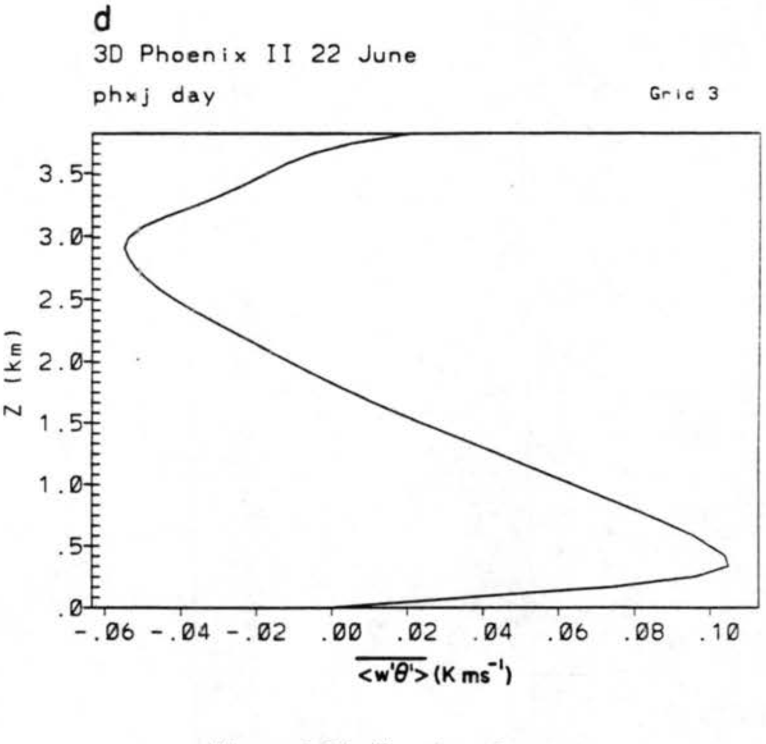


Figure 6.21: Continued.

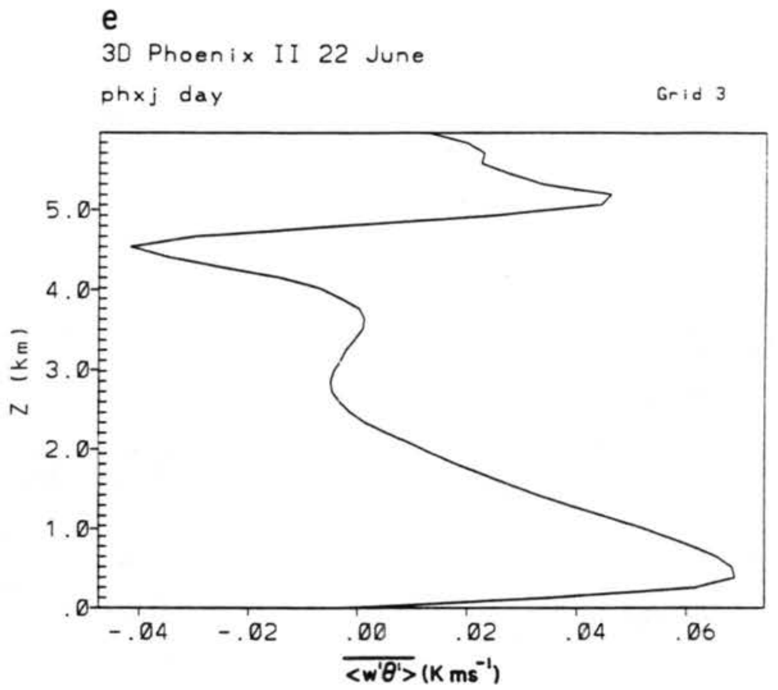


Figure 6.21: Continued.

wind variance just below the top of the plains boundary layer, with the model predicting somewhat larger values. The observations do not capture a second local maximum near the surface and do not have the sharp decrease in horizontal velocity variance at the plains boundary layer top. These are near the edges of the observations. Through the afternoon, the LES predicted values of the $\overline{< u'u' >}$ and the $\overline{< v'v' >}$ maxima, just below the plains boundary layer top, tend to decrease. At some of the later times, rather large magnitudes in horizontal velocity variance can be found above the plains boundary layer, in the area that is affected by the mountain boundary layer and out of reach of the radar observations.

The vertical velocity variance predicted by the model is given in Figure 6.25. The model and observations agree quite well in placing the maximum vertical velocity variance at about 1 km AGL with a value of about 3 $m^2s^{-2}$. Noteworthy, is the fact that neither observations or LES results have vertical velocity variance returning to zero near the top of the plains boundary layer. The model profiles show that the magnitude of the

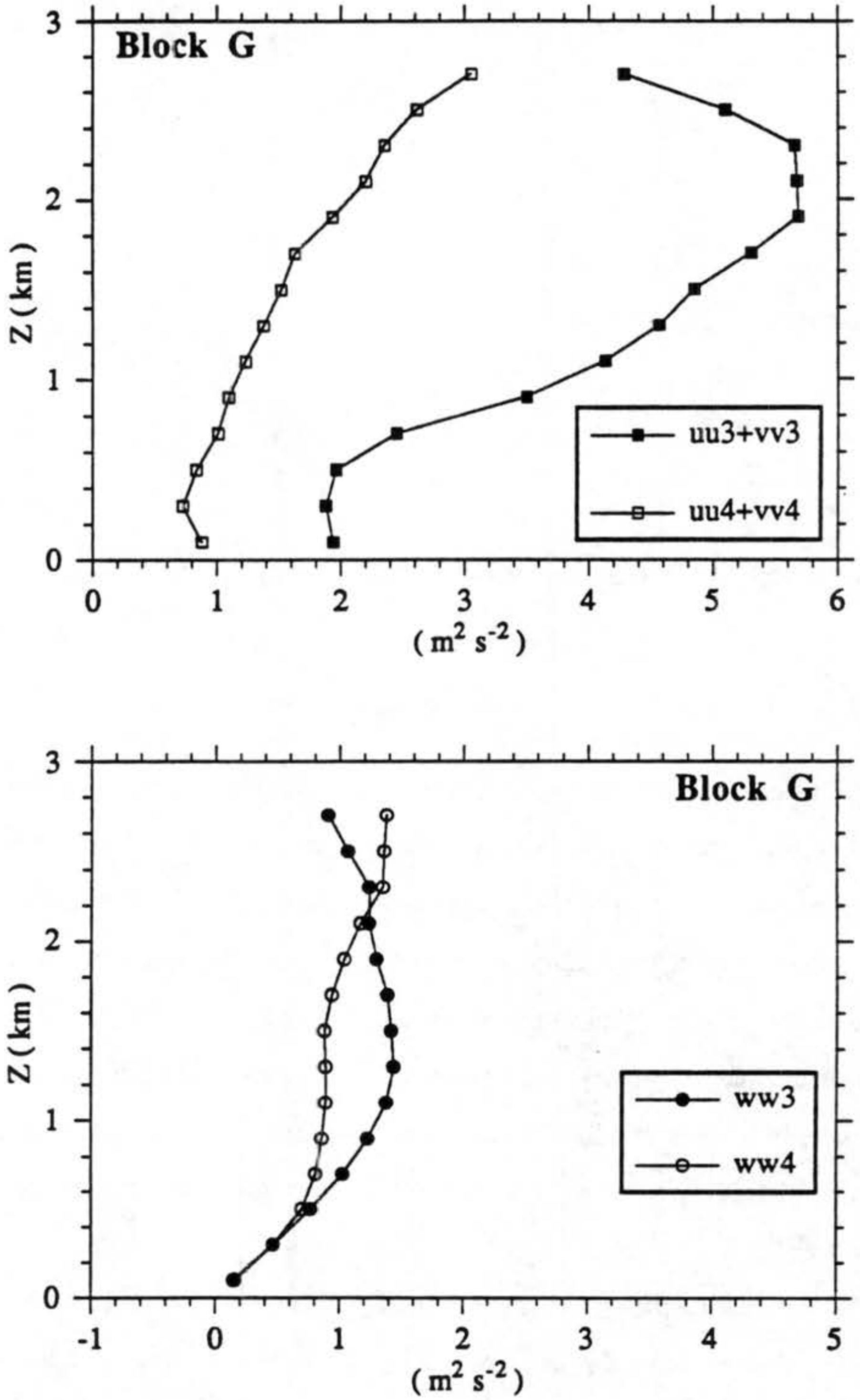


Figure 6.22: Vertical profiles of horizontal and vertical velocity variances from radar data collected during block G on 22 June. From Schneider (1991).

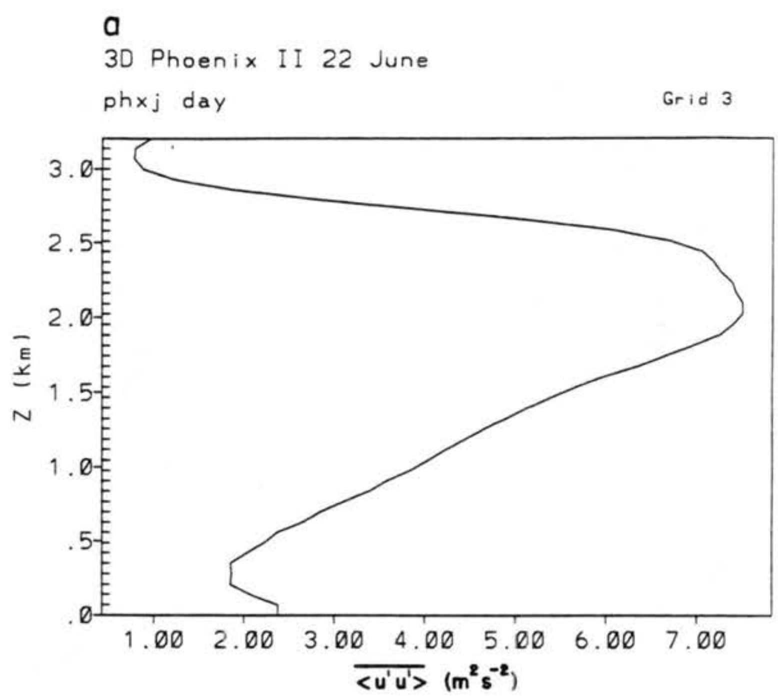


Figure 6.23: Vertical profiles of u velocity variance $\overline{< u'u' >}$, in $m^2s^{-2}$, from the LES. The averaging period from 1940 to 2000 UTC (1240-1300 MST) is presented in (a), 2020 to 2040 UTC (1320-1340 MST) in (b), 2120 to 2140 UTC (1420-1440 MST) in (c), 2220 to 2240 UTC (1520-1540 MST) in (d), and 2300 to 2330 UTC (1600-1620 MST) in (e).

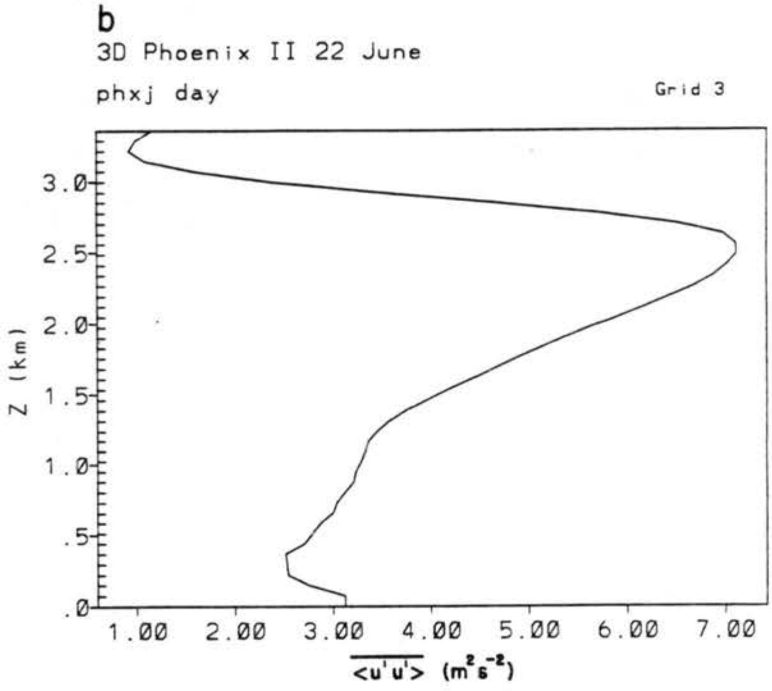


Figure 6.23: Continued.

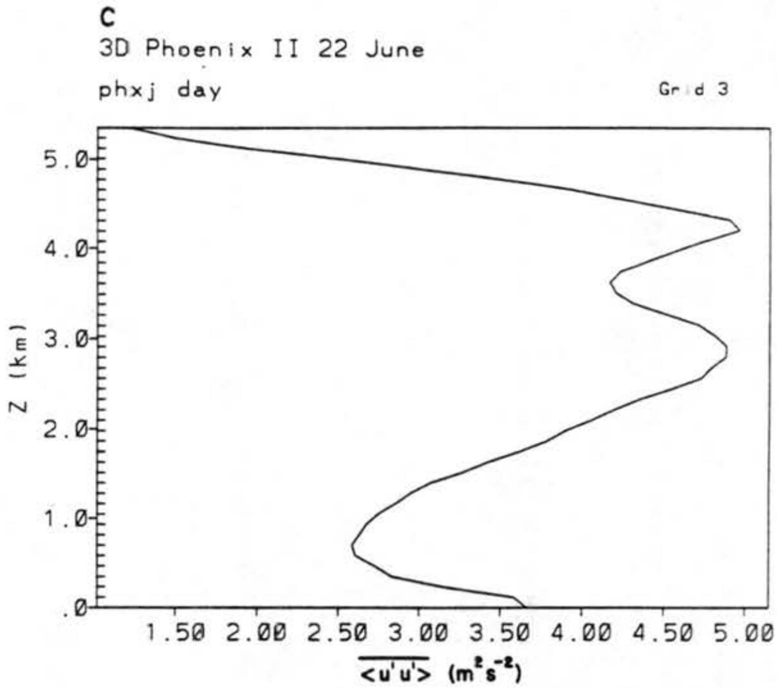


Figure 6.23: Continued.

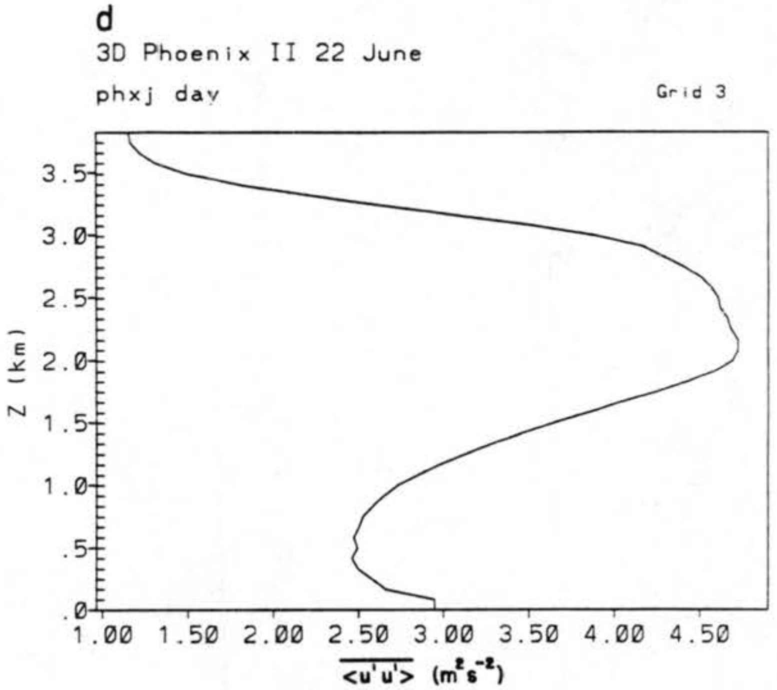


Figure 6.23: Continued.

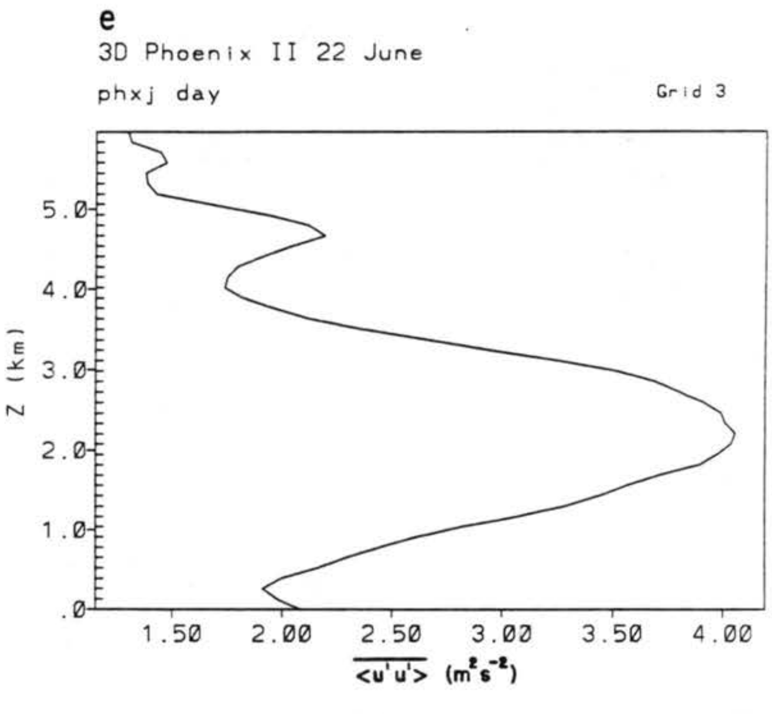


Figure 6.23: Continued.

maximum $\overline{< w'w' >}$ begins to decrease later in the afternoon. There is also evidence of a secondary maximum in vertical velocity variance above the plains boundary layer. The u momentum flux, $\overline{< u'w' >}$, for various time blocks of radar data through the afternoon is given in Figure 6.26 and the corresponding LES results are given in Figure 6.27. For the time periods simulated, both observations and the model give negative momentum flux through the depth of the boundary layer. This is not surprising, since the strongest winds are above the plains boundary layer. The shape of the profile changes through the afternoon, particularly in the observations. In the first time period ending at 2000 UTC (1300 MST), the level of maximum momentum flux is 1.4 km in the radar observations and 1.6 km in the LES, but the magnitude of the momentum flux in the LES is nearly twice as large (1.8 $m^2s^{-2}$). Also, the radar observations become positive in the highest levels of the boundary layer. While the LES results give decreasing momentum flux in the highest levels, they do not become positive. The shape and magnitude of the LES results are more consistent with time than the observations. The height of the maximum is from

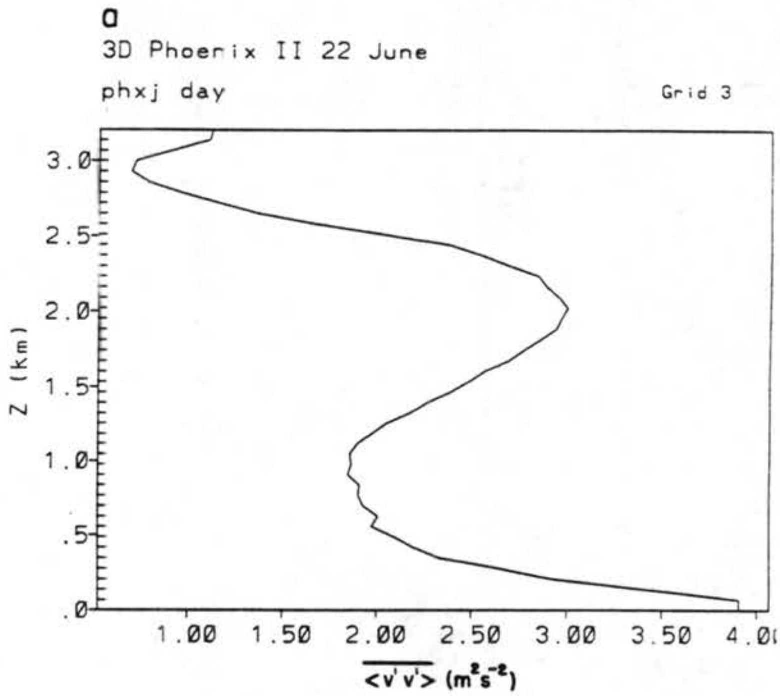


Figure 6.24: Vertical profiles of v velocity variance $\overline{< v'v' >}$, in $m^2s^{-2}$, from the LES. The averaging period from 1940 to 2000 UTC (1240-1300 MST) is presented in (a), 2020 to 2040 UTC (1320-1340 MST) in (b), 2120 to 2140 UTC (1420-1440 MST) in (c), 2220 to 2240 UTC (1520-1540 MST) in (d), and 2300 to 2330 UTC (1600-1620 MST) in (e).

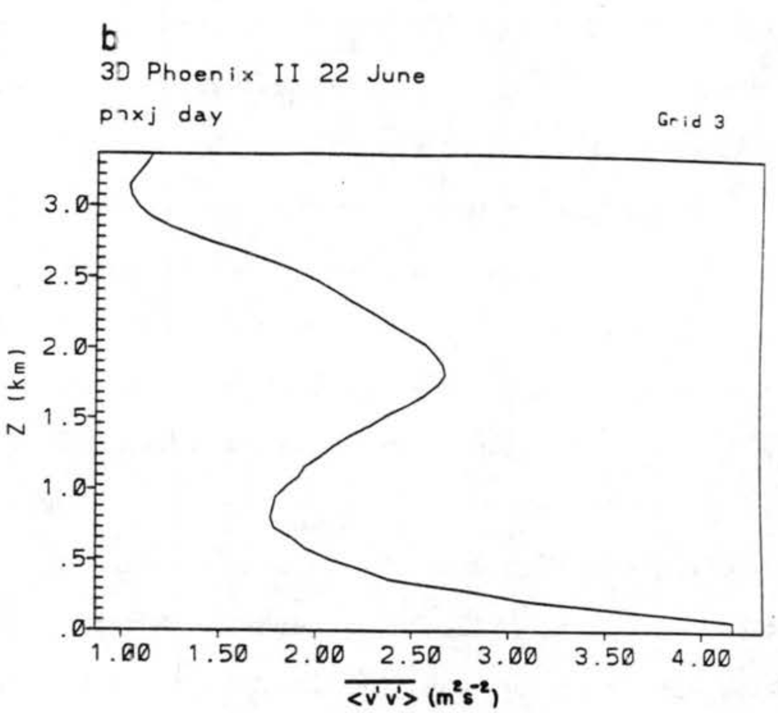


Figure 6.24: Continued.

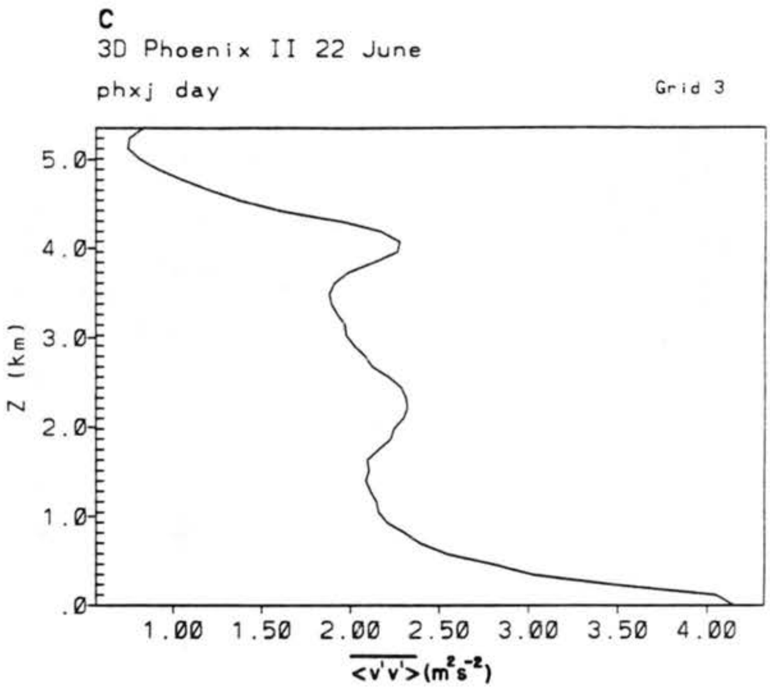


Figure 6.24: Continued.

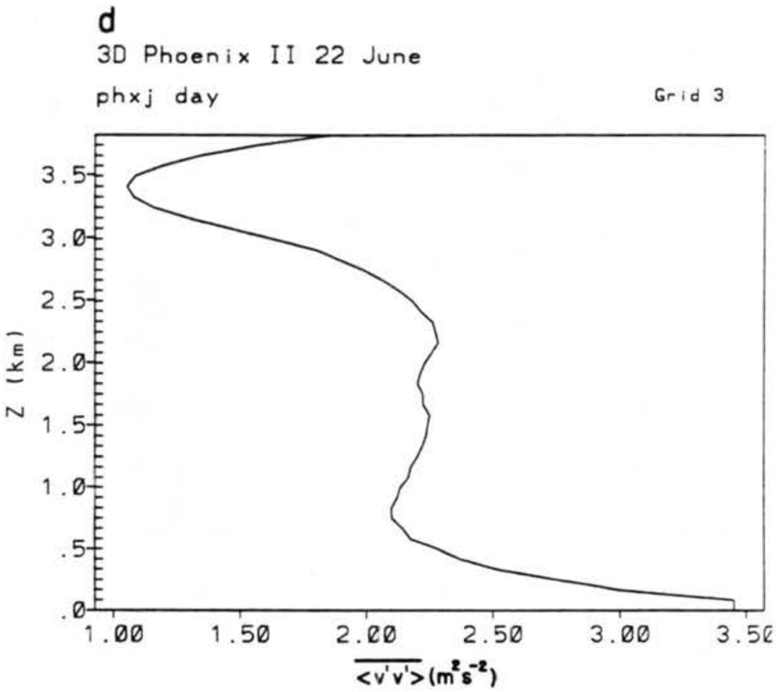


Figure 6.24: Continued.

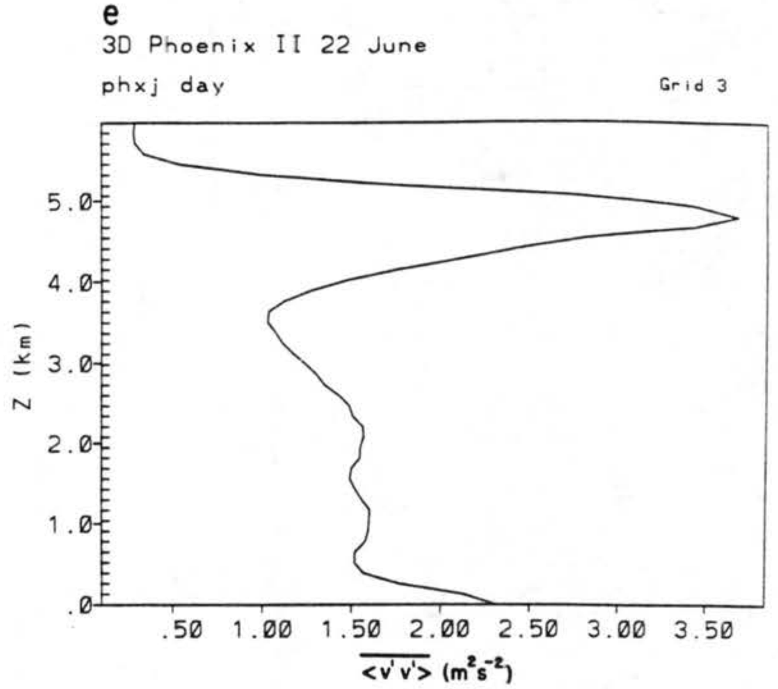


Figure 6.24: Continued.

1.0 to 2.2 km and the maximum magnitudes steadily decrease with time. Recall that the mean wind shear also decreases slowly over the afternoon in the model (Figure 6.11). For the time period ending at 1240 UTC, the magnitude of the maximum momentum flux predicted by the LES is somewhat less than the observations.

The skewness is given by $\overline{\frac{<w'^3>}{<w'^2>^{\frac{3}{2}}}}$. It represents the relative cross-sectional area of updrafts to downdrafts, with positive skewness indicating relatively narrow updrafts. Figure 6.28 presents the skewness profiles derived from the radar data, while Figure 6.29 presents the skewness profiles represented in the model. Both have near zero values throughout the afternoon at the surface. This is not what has been observed by other observational studies (see Figure 2.8), presumably due to the lack of resolution in both the model and radar data near the surface. The maximum value of skewness in the LES profile can be found to be at approximately the level of the maximum found in the observations (around 1.7 km) or higher. The value of the maximum is about 0.6, which is comparable to the maximum found in some of the observed profiles. The skewness

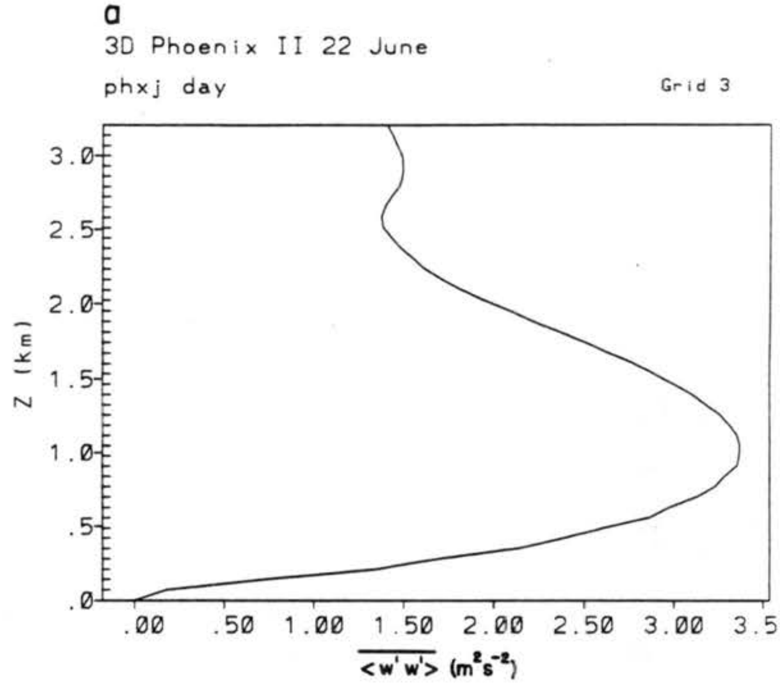


Figure 6.25: Vertical profiles of w velocity variance $\overline{<w'w'>}$, in $m^2s^{-2}$, from the LES. The averaging period from 1940 to 2000 UTC (1240-1300 MST) is presented in (a), 2020 to 2040 UTC (1320-1340 MST) in (b), 2120 to 2140 UTC (1420-1440 MST) in (c), 2220 to 2240 UTC (1520-1540 MST) in (d), and 2300 to 2330 UTC (1600-1620 MST) in (e).

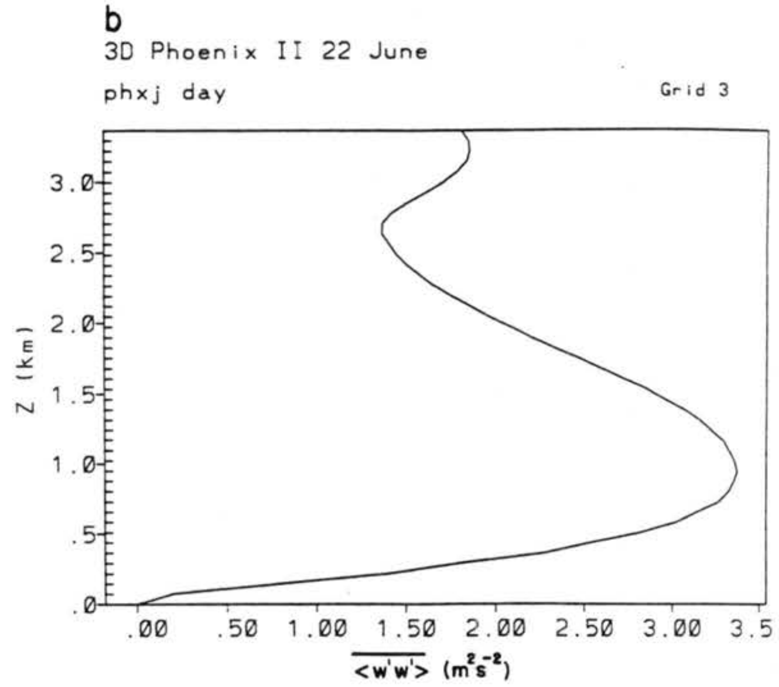


Figure 6.25: Continued.

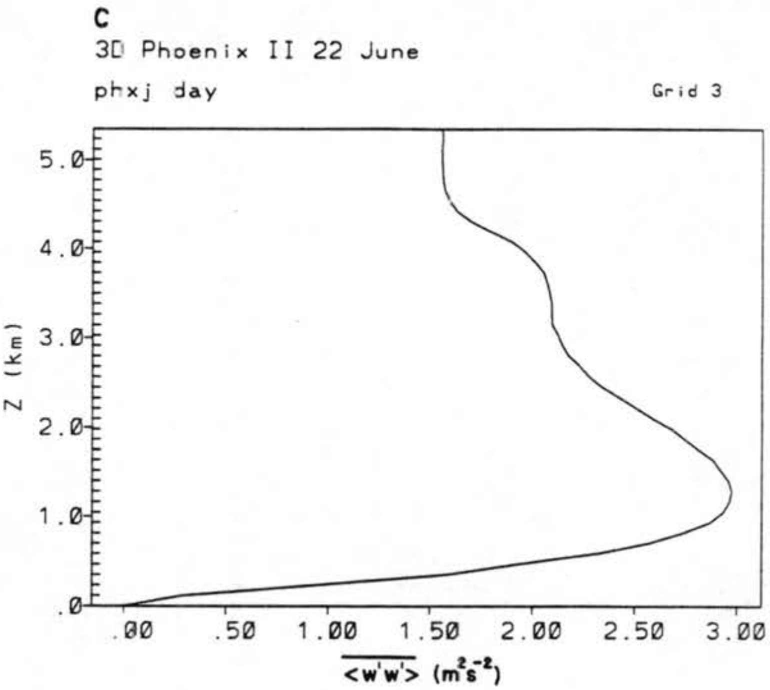


Figure 6.25: Continued.

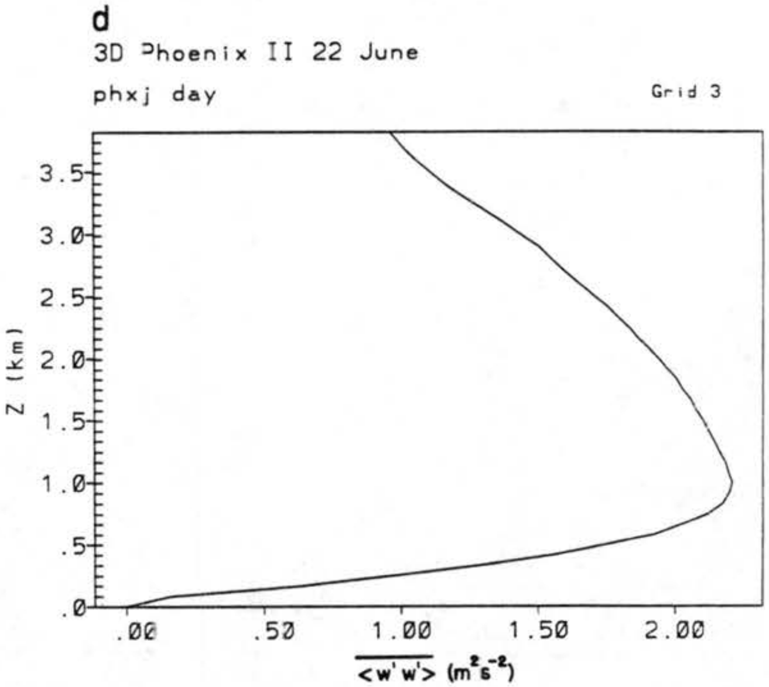


Figure 6.25: Continued.

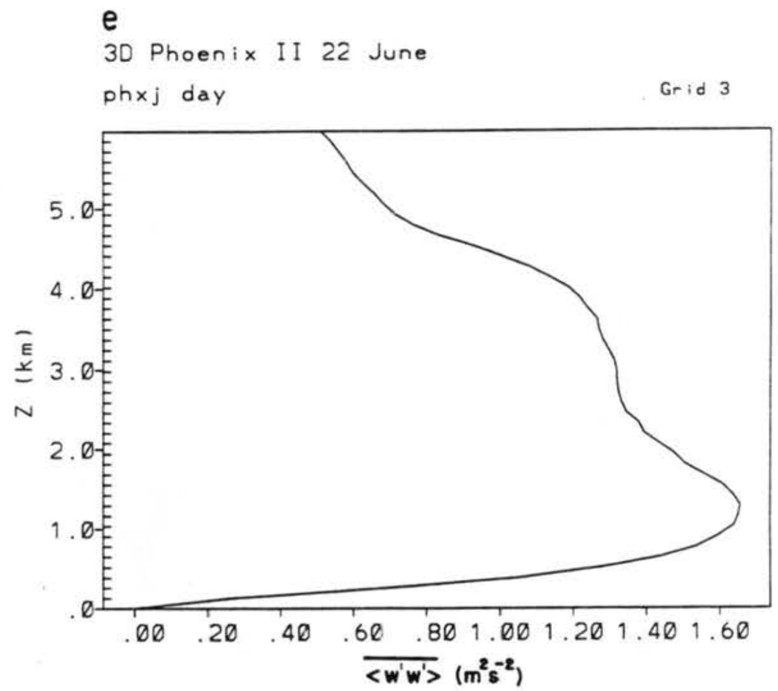


Figure 6.25: Continued.

in the LES profiles drops to negative values above the plains boundary layer except for the time averaging periods ending at 2140 UTC and 2320 UTC, where second local maxima are found in the elevated neutral stability layer. The observations tend to have skewness approaching zero near the top of the boundary layer, but are highly variable throughout the afternoon. The interpretation of the skewness profiles, where positive skewness indicates relatively small updrafts, presumes a mean vertical velocity of zero. From Figure 6.13, there are non-zero values of $\overline{< w >}$ in each of the averaging times. The effect of the mean upward vertical motion in the first and last averaging periods is to decrease the magnitude of the positive skewness in those time blocks. Likewise, the mean subsidence at the other times adds to the positive skewness.

In general, the turbulent statistics derived from the LES predictions agree well with the observations of Phoenix II. Throughout these comparisons of the turbulence statistics produced in the nested grid LES used in this study to the statistics from the Phoenix II radar observations, one particular difference is persistent. The profiles from the LES

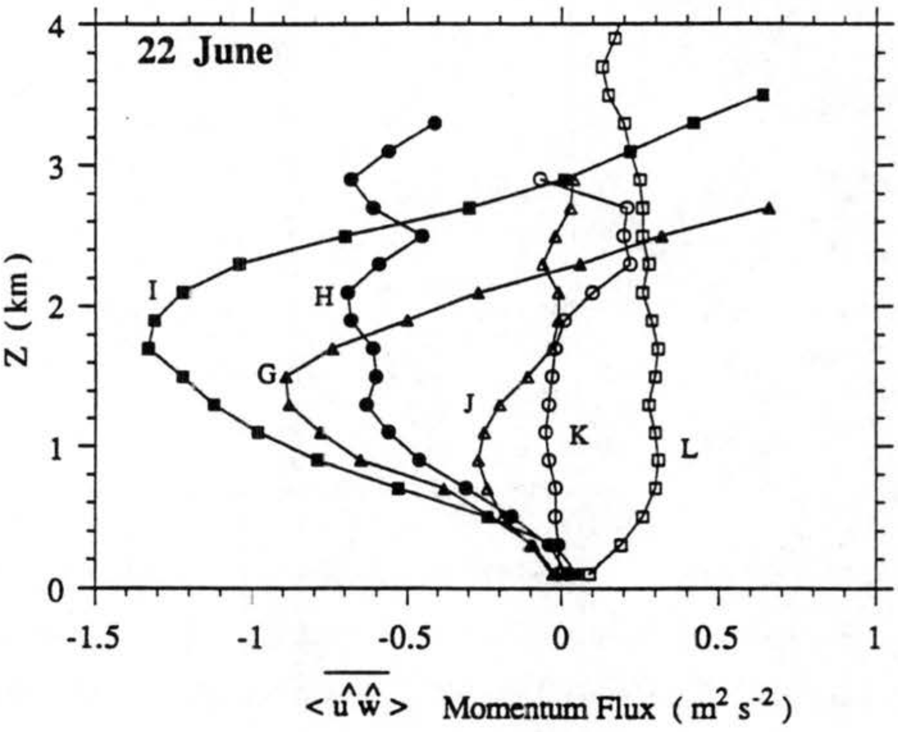


Figure 6.26: Vertical profiles of momentum flux from the radar data on 22 June. Block times are defined in Table 1. From Schneider (1991).

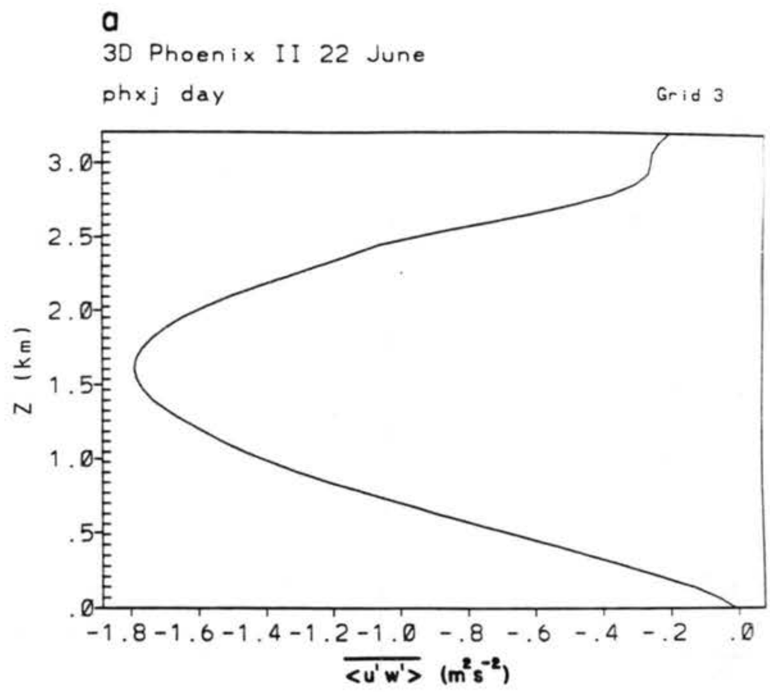


Figure 6.27: Vertical profiles of momentum flux $\overline{< u'w' >}$, in $m^2s^{-2}$, from the LES. The averaging period from 1940 to 2000 UTC (1240-1300 MST) is presented in (a), 2020 to 2040 UTC (1320-1340 MST) in (b), 2120 to 2140 UTC (1420-1440 MST) in (c), 2220 to 2240 UTC (1520-1540 MST) in (d), and 2300 to 2330 UTC (1600-1620 MST) in (e).

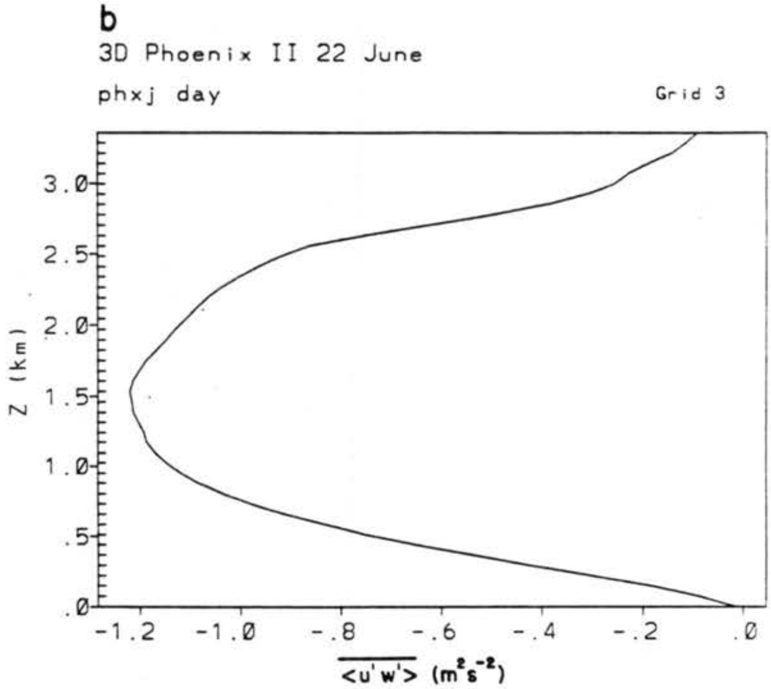


Figure 6.27: Continued.

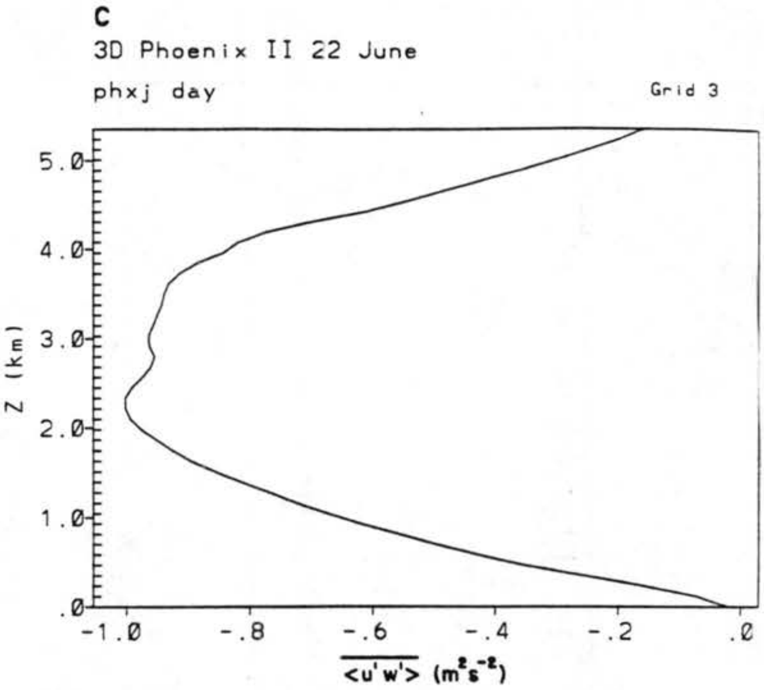


Figure 6.27: Continued.

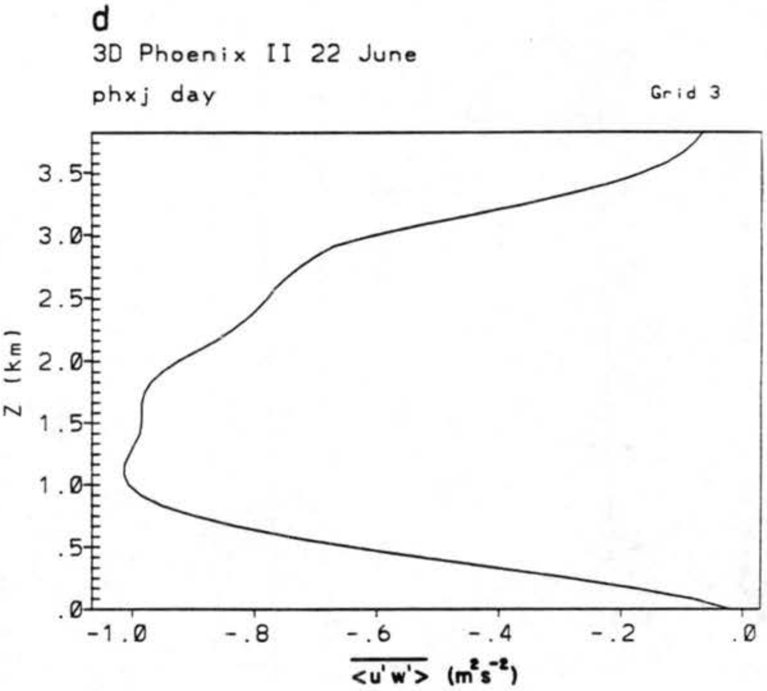


Figure 6.27: Continued.

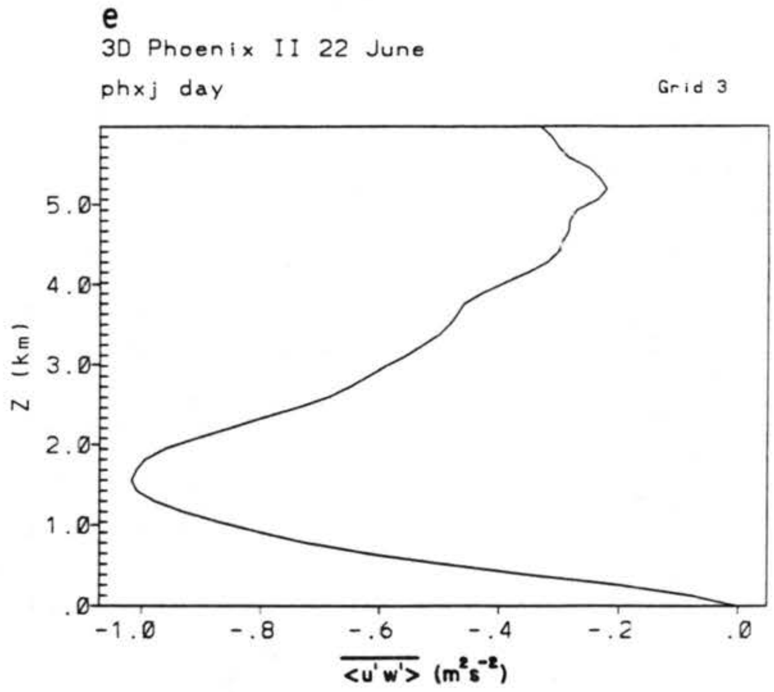


Figure 6.27: Continued.

do not change as much from one averaging period to the next. The profiles derived from the radar observations can change dramatically. This can be explained by the difference between the LES and the radar observations in the number of realizations of eddies over which the horizontal averaging takes place. The east-west extent of the LES averaging area is nearly 36 km, as opposed to about 9 km for the radar dual Doppler area, and a larger number of eddies can be represented. In fact, Figure 6.30 gives composites of the early afternoon radar blocks that compare better with the LES profiles. It seems that the large LES domain gives a better estimate of the ensemble average. The nested grid LES also has the advantage of being able to derive statistics in the area above the plains boundary layer. The chaff used for the radar reflections does not mix with significant concentrations to give reliable statistics from the radar observations at these heights.

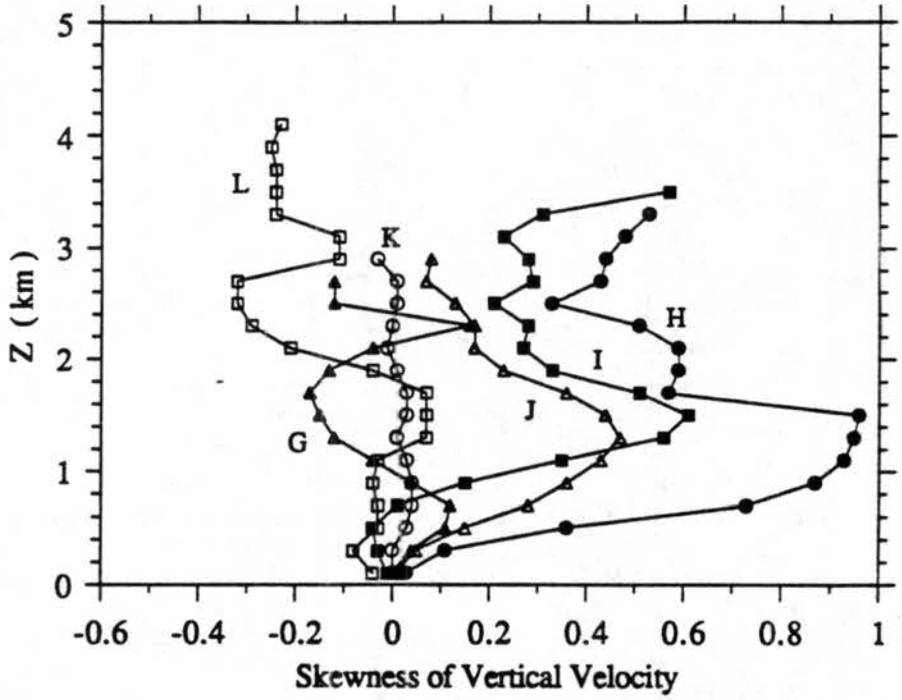


Figure 6.28: Vertical profiles of vertical velocity skewness from the radar data. Block times are defined in Table I. From Schneider (1991).

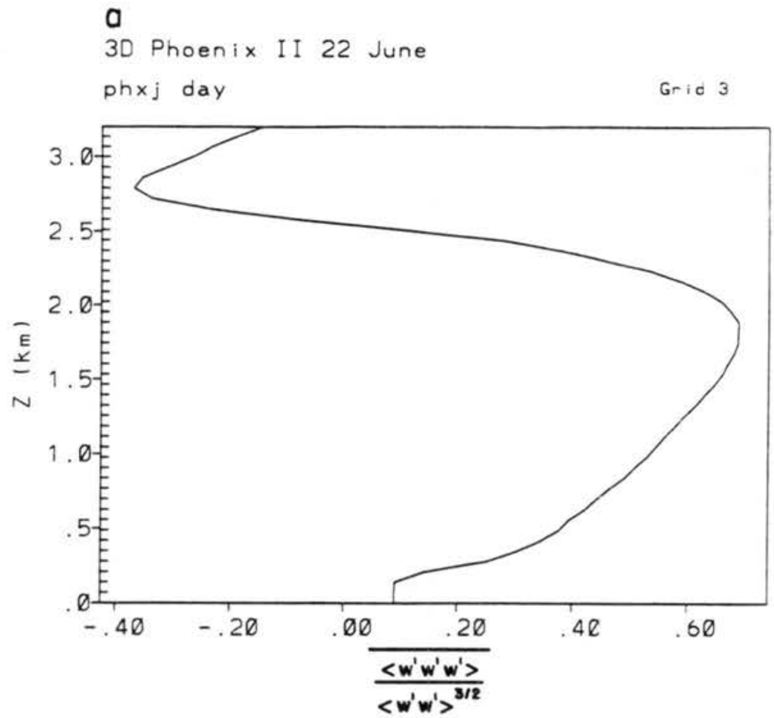


Figure 6.29: Vertical profiles of vertical velocity skewness $\frac{<w'^3>}{<w'^2>^{\frac{3}{2}}}$, from the LES. The averaging period from 1940 to 2000 UTC (1240-1300 MST) is presented in (a), 2020 to 2040 UTC (1320-1340 MST) in (b), 2120 to 2140 UTC (1420-1440 MST) in (c), 2220 to 2240 UTC (1520-1540 MST) in (d), and 2300 to 2330 UTC (1600-1620 MST) in (e).

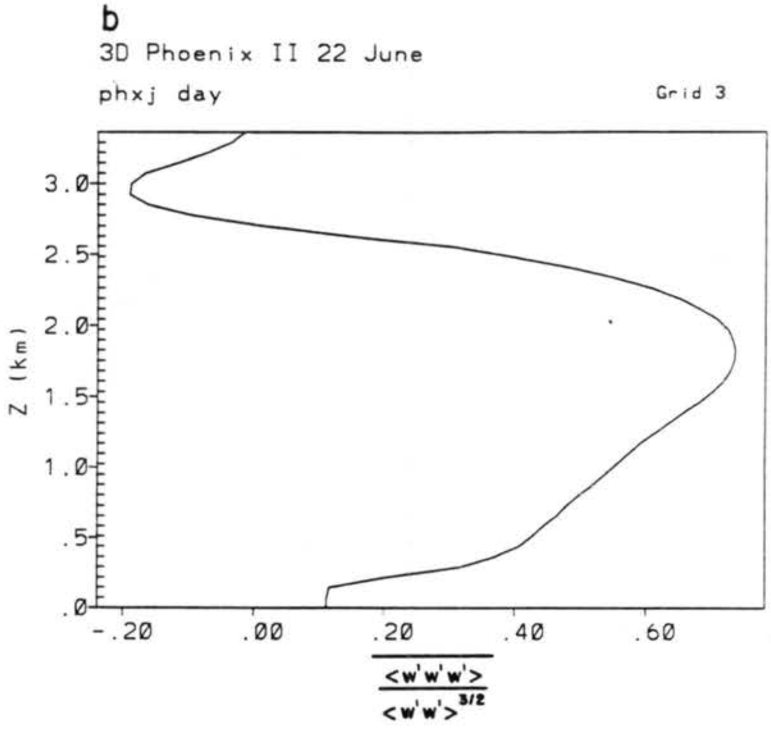


Figure 6.29: Continued.

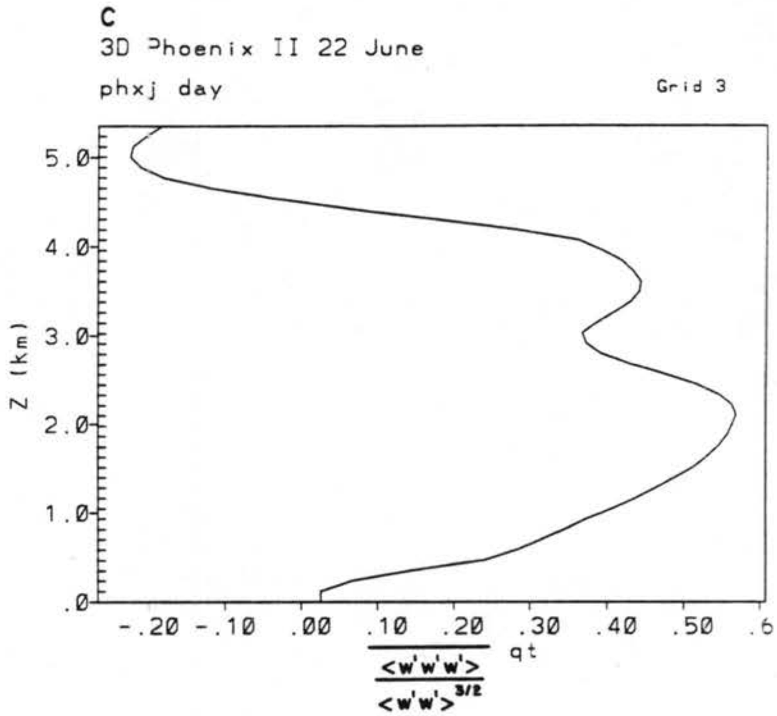


Figure 6.29: Continued.

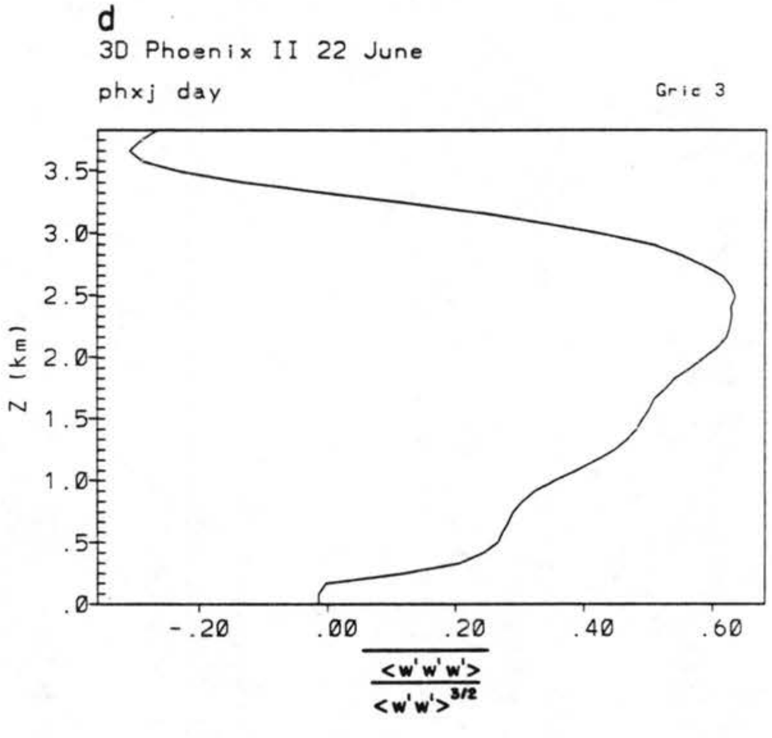


Figure 6.29: Continued.

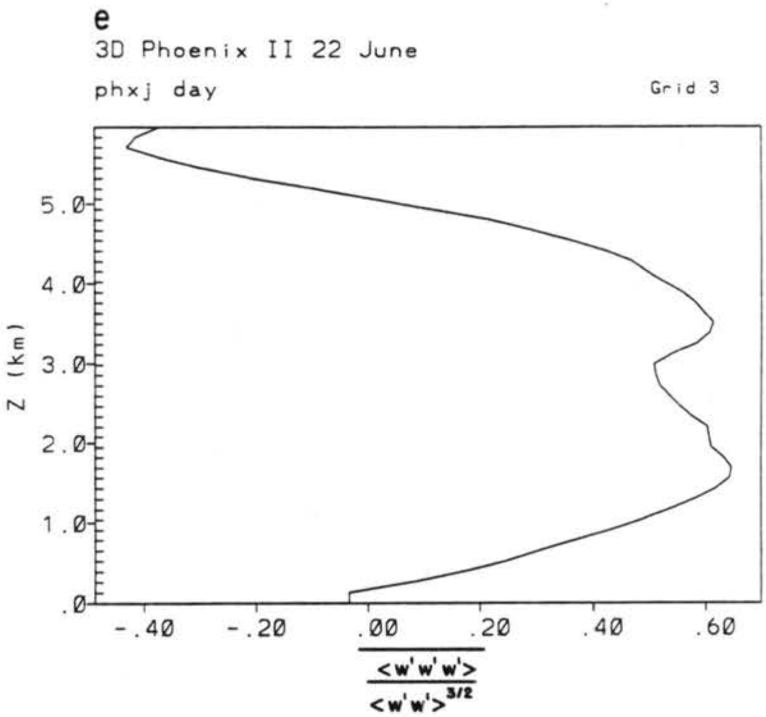


Figure 6.29: Continued.

### 6.2.2 Comparisons to LES of the horizontally homogeneous boundary layer

For purposes of comparison, profiles of the turbulence statistics from LES of the horizontally homogeneous boundary layer are taken from Hadfield (1988), remembering that his profiles are scaled by $z_i$, $w_*$, and $\theta_*$.

The boundary layer top, $z_i$, is determined to be where the heat flux is minimum. This is where entrainment leads to boundary layer growth. Figure 6.31 gives Hadfield's resolved heat flux and the sum of the resolved and subgrid heat fluxes and can be compared to Figure 6.21 of resolved heat flux for the current nested grid study. Both exhibit the linear decrease with height to the minimum at the boundary layer top. For the two time periods ending at 2140 and 2320 UTC the nested grid LES has a small negative heat flux at the top of the plains boundary layer and, in addition, has a sharp minimum below the stronger inversion that caps the mountain boundary layer. This is quite different than expected from the horizontally homogeneous LES. The small magnitude of the negative heat flux at the top of the plains boundary layer is the result of having only a

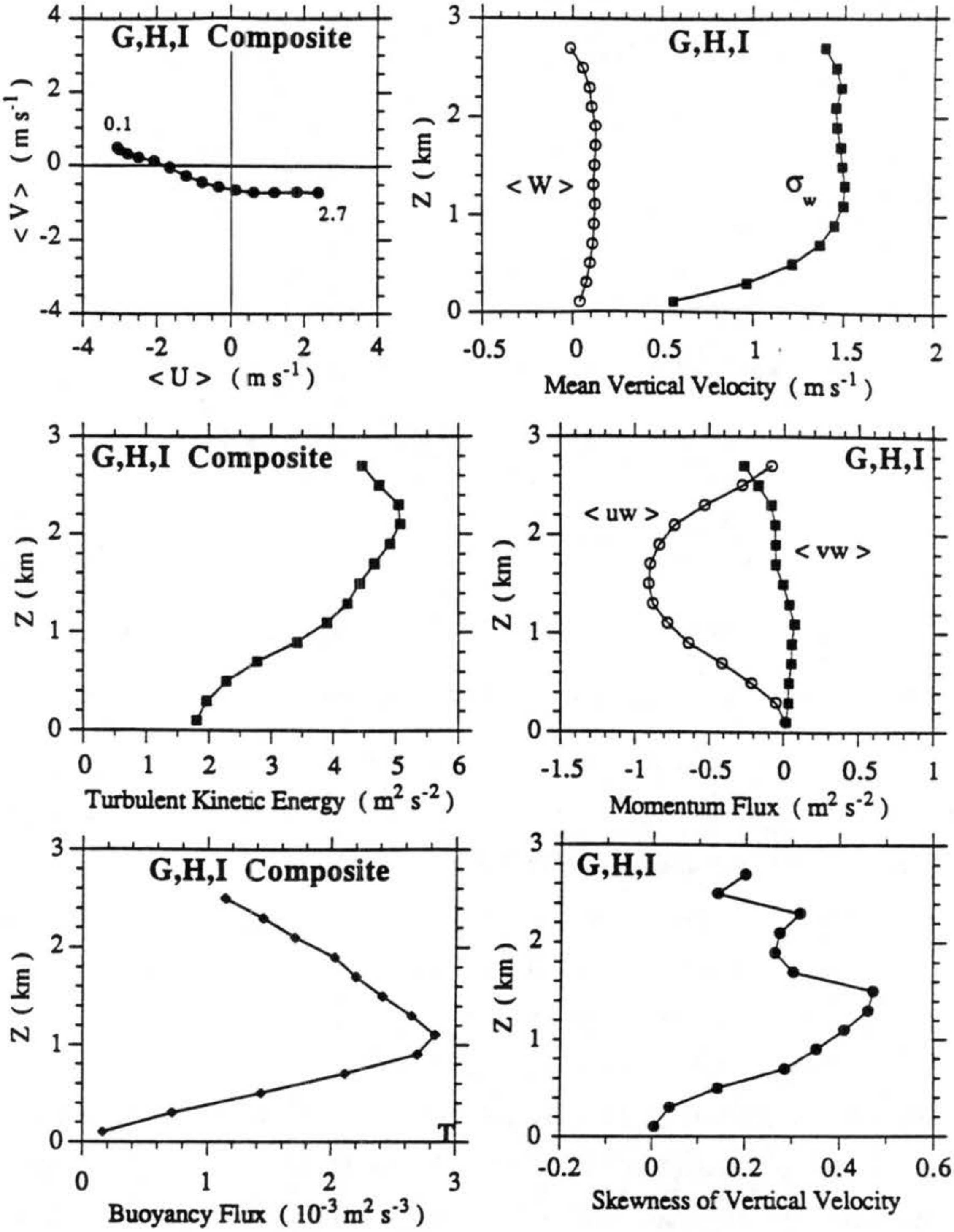


Figure 6.30: Composites of vertical profiles from the radar data for early afternoon of 22 June. From Schneider (1991).

weak inversion capping the plains boundary layer and therefore entrainment of warm air from above is small. It is consistent then that the negative heat flux below the stronger inversion at higher levels has a larger magnitude. The subgrid portion of the heat flux (not shown for the current study) dominates at the surface so that the total heat flux is equal to the heat flux from the soil surface. For the averaging period ending at 2000 UTC (1300 MST), the surface heat flux in the nested grid LES is over 0.3 $mKs^{-1}$, which is significantly higher than the constant value prescribed by Hadfield of 0.2 $mKs^{-1}$, but reasonable for 22 June.

The horizontal velocity variances from Hadfield's (1988) horizontally homogeneous LES are in Figure 6.32. In his simulation, the u and v-components of the winds have very similar profiles, with maxima in the velocity variances near the surface and near the boundary layer top. He points out that LES in general tend to underestimate the horizontal velocity variances in the mid levels. The maximum near the surface is not found so much in observations and can be reduced when the surface roughness is increased. The u-component velocity variance in the nested grid LES presented in Figure 6.23 is dominated by the maximum near the boundary layer top. The maximum near the surface is not much different from the horizontally homogeneous LES (an estimate of $w_*$ for the afternoon of 22 June 1984 is 2.8 $ms^{-1}$) and the variance is generally larger throughout the depth of the boundary layer than Hadfield's barotropic LES. The wind shear present on this day makes a major contribution to the velocity variance that is not normally found in the horizontally homogeneous boundary layer, especially in the upper portions of the boundary layer. Again the second local maximum well above the plains boundary layer is unique to this simulation.

The v-component velocity variance profile (Figure 6.24) appears more like the LES for the horizontally homogeneous boundary layer. Recall from Section 6.1.2 that the wind shear in the v-component is much smaller within the plains boundary layer. Never the less, the velocity variance in this direction is larger than expected for the horizontally homogeneous case.

The vertical velocity variance given in Figure 6.33 is for the horizontally homogeneous case. The resolved portion of the profile can be compared to the nested grid LES

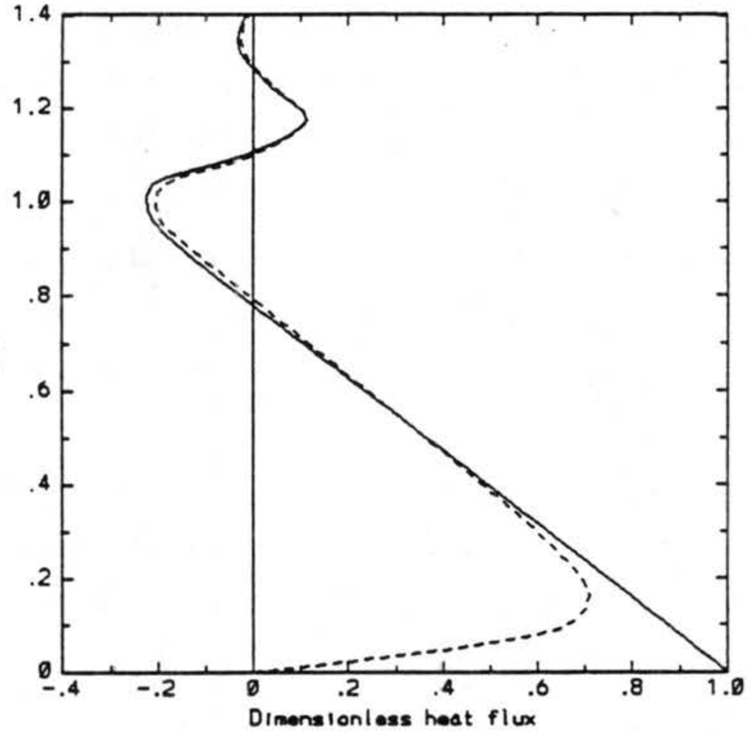


Figure 6.31: Heat flux profile from the horizontally homogeneous LES. Resolved (dashed line) and resolved pus subgrid (solid line) vertical heat flux are made dimensionless with $w_*\theta_*$. From Hadfield (1988).

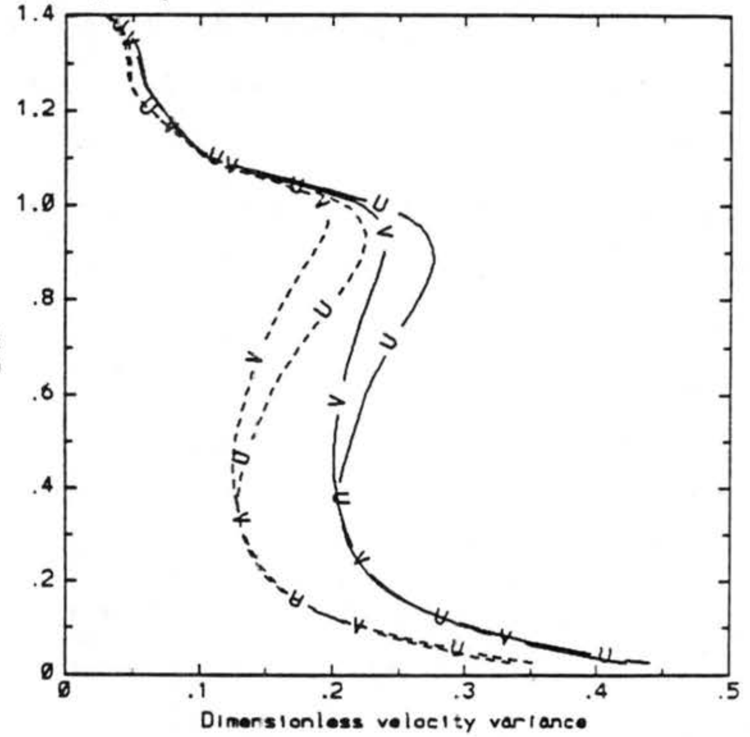


Figure 6.32: Vertical profiles of the dimensionless horizontal velocity variances for the horizontally homogeneous LES. The curves are labeled U for the u-component and V for the v-component. The dashed curves show the resolved part only and the solid curves include a subgrid contribution. From Hadfield (1988).

in Figure 6.25. Typical of the vertical velocity variance profiles, the maximum is found just below the midpoint of the boundary layer after starting at zero at the surface. At the top of the boundary layer, the magnitudes become very small. The nested grid LES of this study and the observations from Phoenix II differ greatly from the horizontally homogeneous boundary layer at the top of the plains boundary layer where $\overline{< w'w' >}$ continues to have significant magnitudes on 22 June 1984. With the stability not as great in the plains boundary layer capping inversion, the buoyancy damping on the vertical motions is not as strong.

The variance of the potential temperature also reflects the weaker capping inversion on the plains boundary layer. Figure 6.34 presents the profiles of $\overline{< \theta'\theta' >}$ for Hadfield's horizontally homogeneous LES along with data from other LES's and observations. Large values of the potential temperature variance are found at the top of the boundary layer but there is a great deal of discrepancy between the studies at this level. Nieuwstadt et al. (1991), in their comparisons of results from a LES using four different models, also note the variation between studies in the temperature variance at that level. They partly explain the differences by the different temperature gradients used in the capping inversion, pointing out that the model that has the largest temperature gradient also has the largest temperature variance at the top of the boundary layer. It is then not surprising to find that the largest values of the temperature variance in the nested grid LES of this study are not at the top of the plains boundary layer, but coincide with the higher and stronger inversion that caps the mountain boundary layer (Figure 6.35). Figure 6.36 gives the profiles of skewness from Hadfield's horizontally homogeneous LES along with data from other LES studies and observations from Young (1986). In both the horizontally homogeneous LES and the nested grid LES, skewness in the low levels is predicted to be very small and underestimates the observed values due to lack of resolution. LeMone (1990) has speculated that gravity waves interacting with the observed convective boundary layer explain the differences found in vertical velocity skewness profiles between LES and observations. In the upper part of the boundary layer, LES skewness coefficients are generally larger than observations. Her explanation of this was that gravity waves

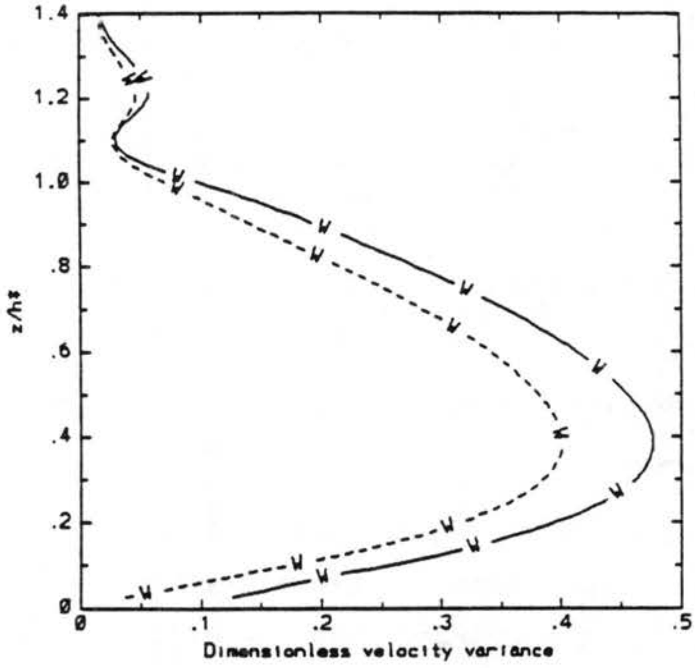


Figure 6.33: Vertical profiles of the dimensionless vertical velocity variances for the horizontally homogeneous LES. The dashed curve shows the resolved part only and the solid curve includes a subgrid contribution. From Hadfield (1988).

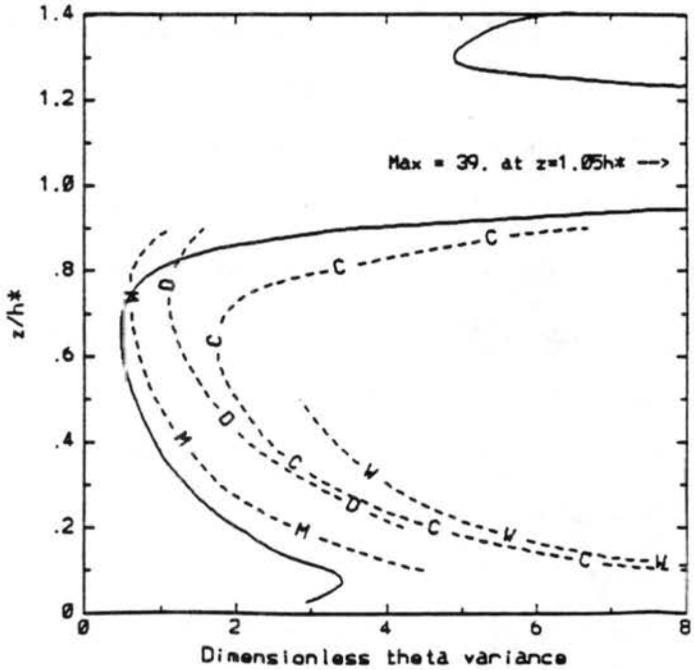


Figure 6.34: Vertical profiles of the dimensionless resolved variance in potential temperature from Hadfield's horizontally homogeneous LES (solid line). Also shown are the fluid tank results of Deardorff and Willis (1985) in curve D, atmospheric observations from Caughey (1982) in curve C, surface layer free convection expression of Wyngaard et al. (1971) in curve W, and resolved potential temperature variance from Moeng and Wyngaard (1984) in curve M. From Hadfield (1988).

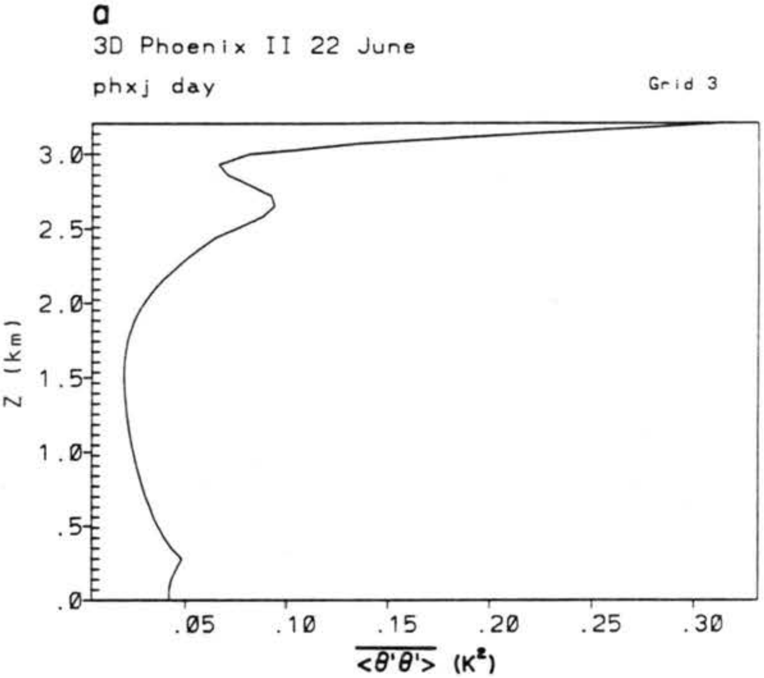


Figure 6.35: Vertical profiles of potential temperature variance $\overline{<\theta'\theta'>}$, in $K^2$, from the LES. The averaging period from 1940 to 2000 UTC (1240-1300 MST) is presented in (a), 2020 to 2040 UTC (1320-1340 MST) in (b), 2120 to 2140 UTC (1420-1440 MST) in (c), 2220 to 2240 UTC (1520-1540 MST) in (d), and 2300 to 2330 UTC (1600-1620 MST) in (e).

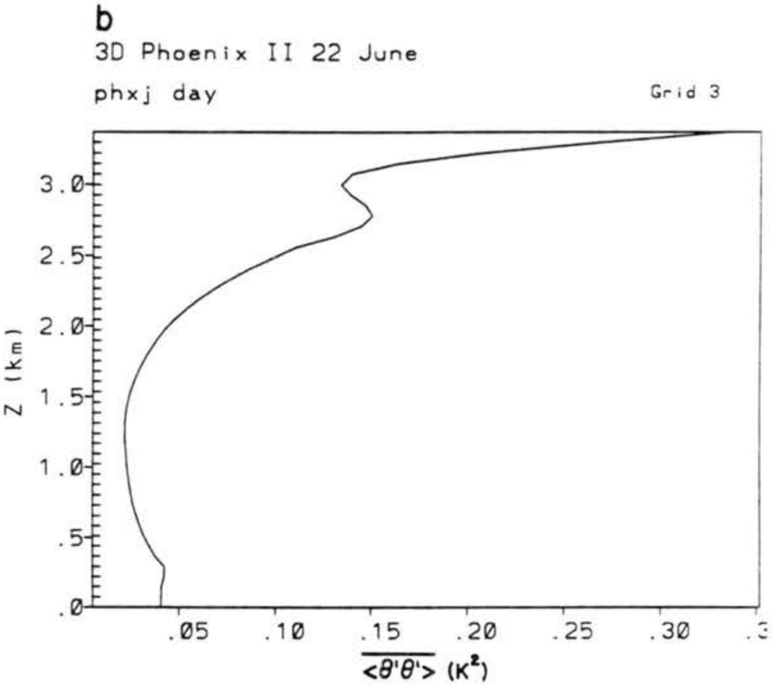


Figure 6.35: Continued.

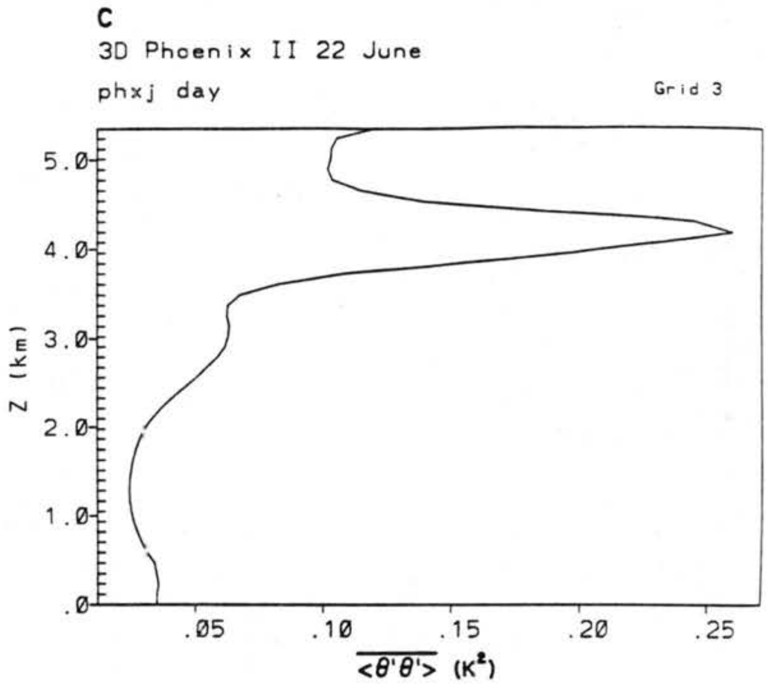


Figure 6.35: Continued.

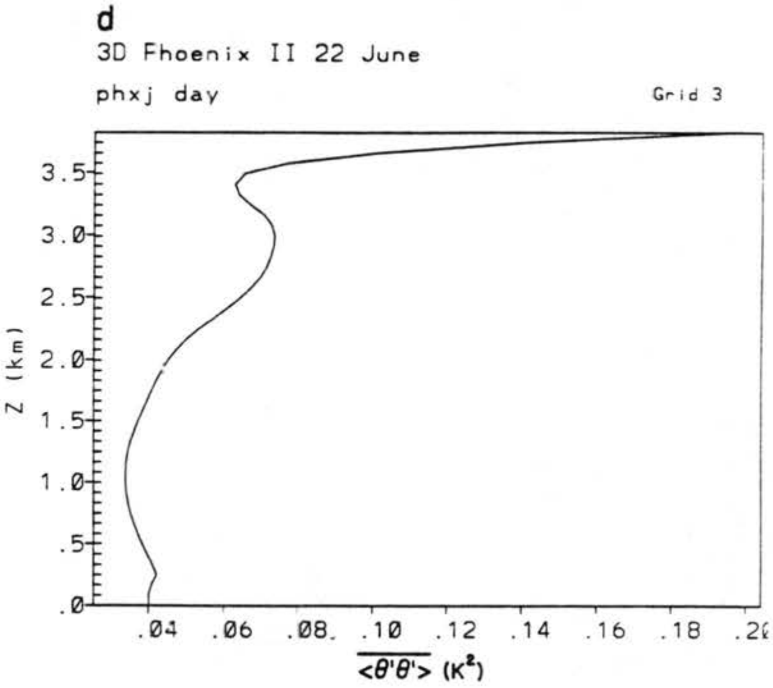


Figure 6.35: Continued.

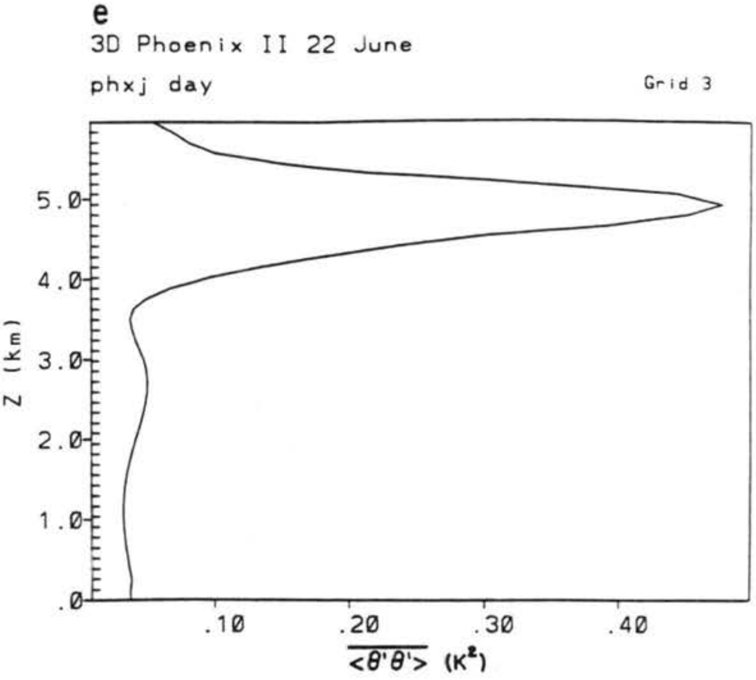


Figure 6.35: Continued.

contribute zero skewness to the observations in the upper portions of the boundary layer. Most LES cannot simulate gravity waves because they use a relatively small domain size in the vertical and horizontal, which restricts both horizontal and vertical wavelengths. In this study, gravity waves can be modeled and the skewness values in the upper portion of the plains boundary layer are comparable to observational studies, as can be seen in Figure 6.29. In the levels above the plains boundary layer, the skewness is non-zero, indicating that turbulence is present in this elevated mixed layer.

This comparison has shown that the turbulence statistics of the plains boundary layer east of the Colorado Rockies are significantly different from the purely convective, horizontally homogeneous boundary layer. The lack of a strong capping inversion, associated with the advection of the mountain boundary layer eastward over the top of the plains boundary layer, is one factor influencing the statistics of the nested grid LES. Another factor is the vertical shear of the horizontal winds. Also the influence of gravity waves can be seen in these statistics.

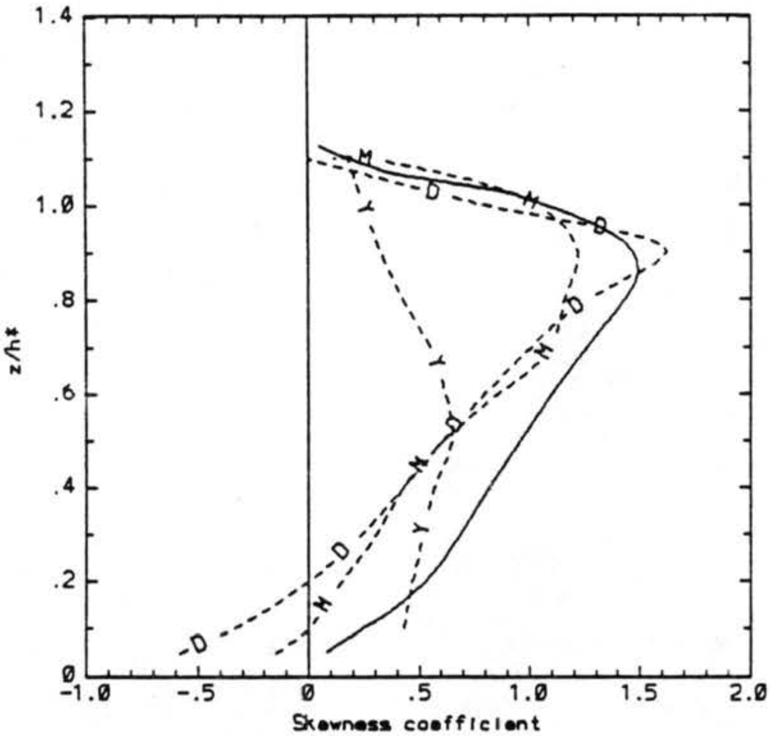


Figure 6.36: Vertical profile of skewness coefficient of resolved w from Hadfield's horizontally homogeneous LES (solid line). Also shown are LES data from Deardorff (1974b) in curve D, and Moeng (1984) in curve M and atmospheric data from Young (1986) in curve Y. From Hadfield (1988).

## 6.3 Spectral Analysis

To investigate how much of the variance of w is associated with a particular size scale, a discrete energy spectrum of the model predicted $w'$ is presented. This gives an indication of the role that gravity waves play in the atmospheric boundary layer in the study area. Also, the phase angle between $w'$ and $\theta'$ from cross spectral analysis indicates if they are in phase, indicating turbulence, or 90 degrees out of phase, indicating linear gravity waves. The largest perturbations of potential temperature and vertical velocity coincide (i.e. the warmest air is associated with the strongest updraft) under the turbulent conditions conditions of the convective boundary layer. But under the influence of gravity waves the largest perturbations of potential temperature do not coincide with the largest vertical velocity perturbations (Stull, 1988; Lin, 1988). The observational data described below are taken from aircraft data analyzed by Lin (1988), and the horizontally homogeneous LES results are again taken from Hadfield (1988).

### 6.3.1 Comparison to Phoenix II observations

The observed power spectrum for $w'$ for five aircraft flights on the days of 17 and 22 June 1984 at 150 m AGL is given in Figure 6.37. It presents the log of the power spectrum multiplied by the wave number and plotted against the log of the wave number. This way of presenting the spectra follows previous LES studies and Schneider (1991) for easier comparisons. Unfortunately, the area under the curve is not proportional to the total variance of w in this presentation. Figure 6.38 gives the power spectrum at what Lin (1988) describes as the entrainment layer (1900-2100 m AGL) and Figure 6.39 gives it in his stable layer (2840-3297 m AGL). The spectra that result from the predictions of the nested grid LES are given in Figure 6.40. The discrete energy spectrum averaged in the y direction and multiplied times the wave number is plotted in the same manner as the aircraft observations. Each of the curves represents a different level in the atmospheric boundary layer. Curve A is at analysis level 5 (almost 600 m AGL). Curve B is at level 14 (about 1700 m AGL), in the middle of the plains boundary layer. Curve C is at level 23 (just over 2700 m AGL) at approximately the plains boundary layer top. Curve D is at level 35 (close to 4200 m AGL), at the bottom of the stronger inversion that caps the mountain boundary layer. And curve E is at level 47 (approximately 5600 m AGL), in the strongly stable layer. Because the aircraft data are compiled from flights on two different days of observations and the nested grid LES results are an average over the twenty minute time period ending at 2140 UTC (1440 MST), the heights of the entrainment and stable layers are different and direct comparisons at a particular height are not valid. But comparisons at relative levels in the boundary layer are useful.

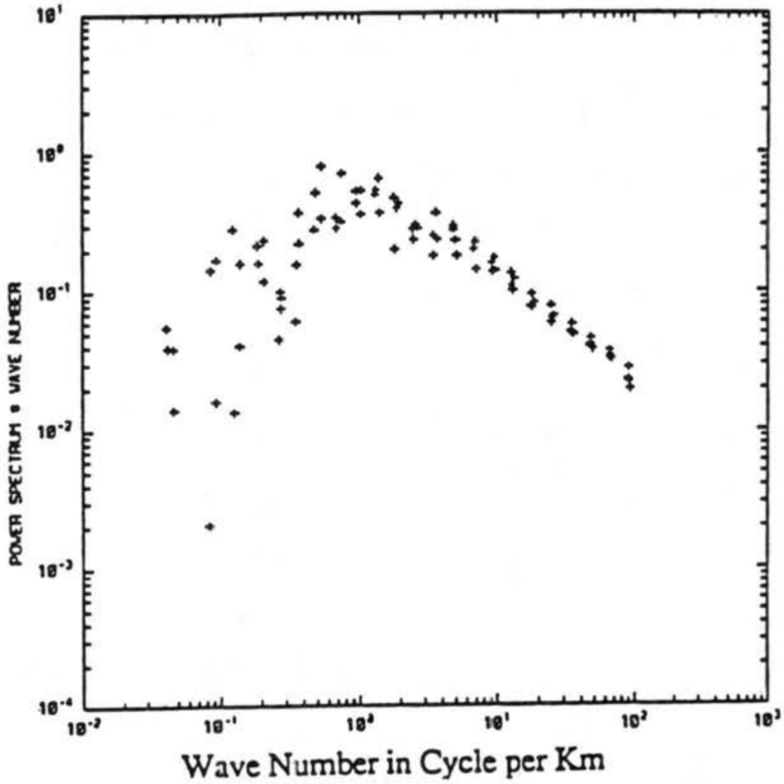


Figure 6.37: The power spectrum of w at 150 m AGL from aircraft data on 22 June. From Lin (1988).

The low level spectrum from the aircraft data shows the importance of the large eddies with the peak energy found at about wave number 1 $km^{-1}$ or wavelength of 1 $km$. At higher wavelengths, the $-\frac{2}{3}$ slope, which is characteristic of the inertial subrange and the energy cascade to smaller scales, can be found. The maximum power density shifts to longer wavelengths at the higher levels of the entrainment layer. And the greatest energy at the level of the stable layer is found around wave number $0.1 km^{-1}$ or wavelength of about 10 km, which is reasonable for gravity waves.

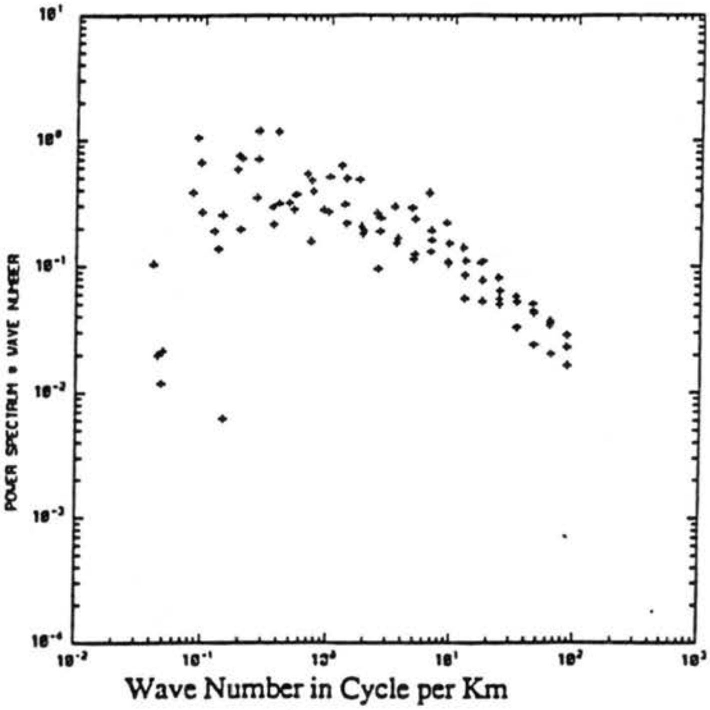


Figure 6.38: The power spectrum of w in layer from 1900 to 2100 m AGL from aircraft data on 22 June. From Lin (1988).

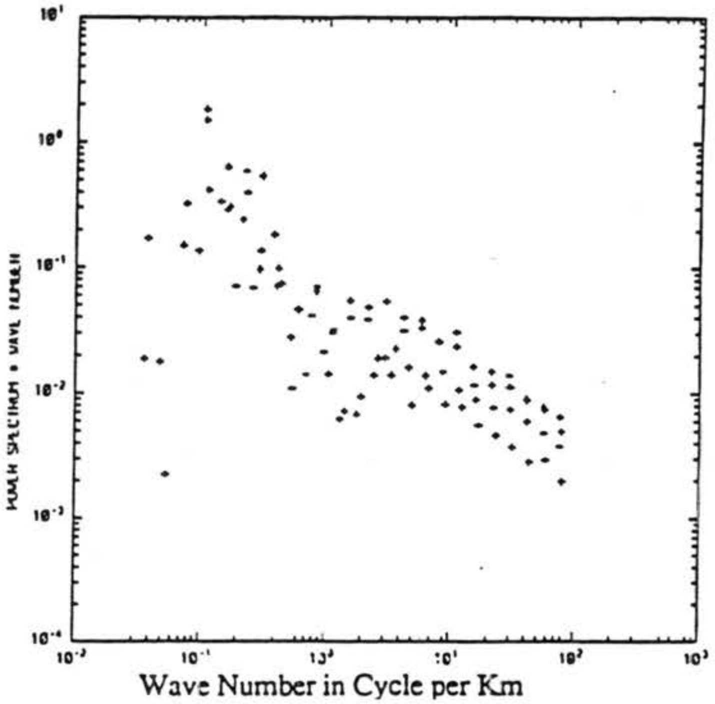


Figure 6.39: The power spectrum of w in layer from 2840 to 3297 m AGL from aircraft data on 22 June. From Lin (1988).

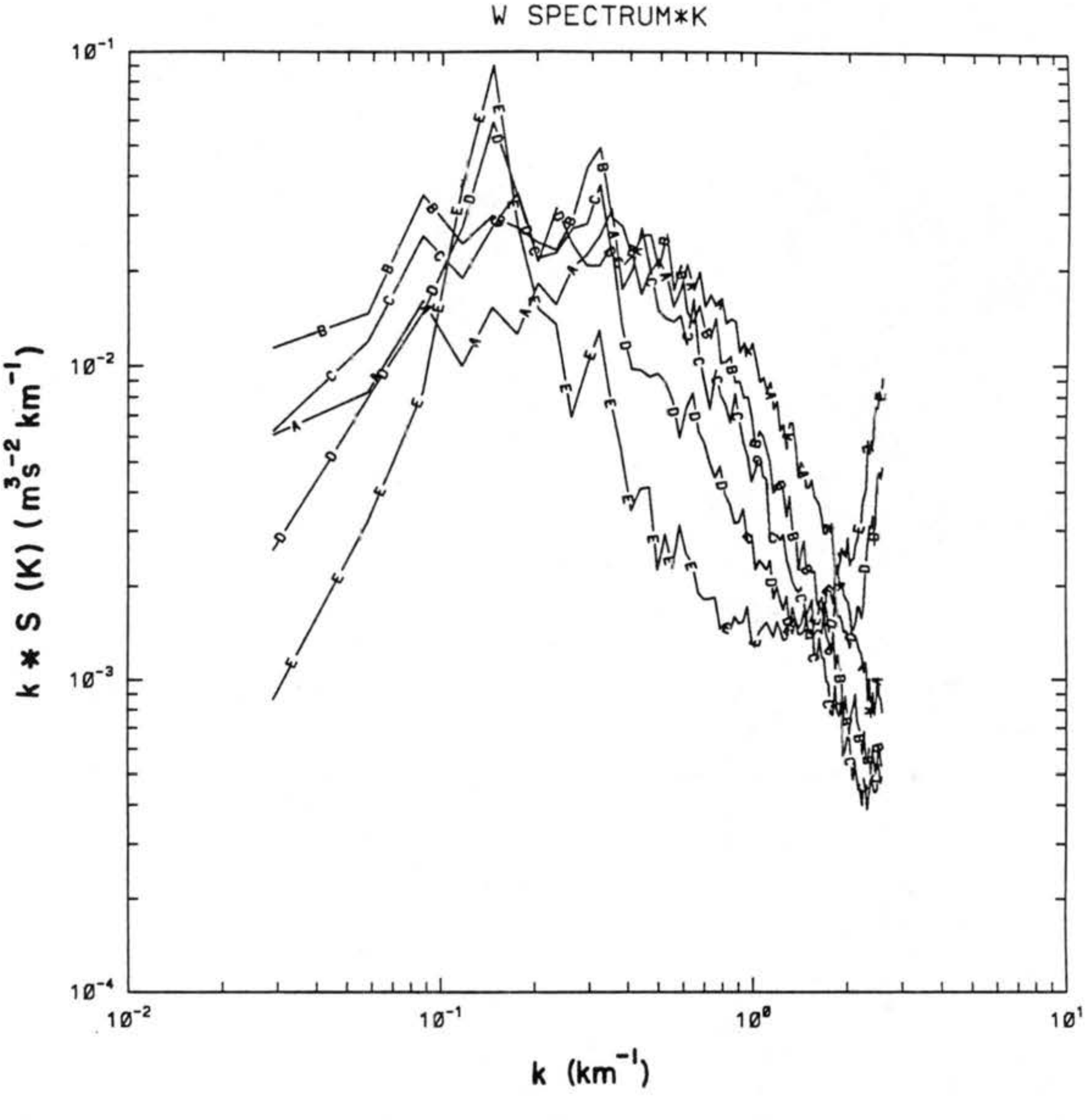


Figure 6.40: The power spectrum of w for the time period 2120 to 2140 UTC (1420-1440 MST). Approximate heights represented by the curves are 600 m AGL in A, 1700 m in B, 2700 m in C, 4200 m in D, and 5600 m in E.

The nested grid LES has the peak in curve A at wavenumber 0.33 $km^{-1}$ or wavelength of about 3 km and just slightly longer wavelengths are associated with the peak energy in curves B and C. This wavelength is somewhat greater than the depth of the plains boundary layer, which is a typical size of the large eddies and consistent with the $1.5z_i$ characteristic wavelength found by Kaimal, et al. (1976). At levels above the plains boundary layer, a distinct peak in energy exists at gravity wave wavelengths of about 7.5 km, consistent with the observations.

While the power spectra of the nested grid LES drops off at higher wavenumbers for all the curves in Figure 6.40, the slope is steeper than the expected $-\frac{2}{3}$. The reason for this will be discussed in section 6.3.2. Also unexpected in these curves is the upward turn of the curves, particularly at the high levels, in the highest wavenumbers. This is associated with the noise described in section 6.1.1 and is not realistic.

The cross spectral analysis of the phase angle between $w$ and $\theta$ derived from the aircraft data is presented in Figure 6.41 for 150 m AGL, Figure 6.42 for Lin's entrainment layer, and Figure 6.43 in his stable layer. The two lower layers have the phase difference to be close to zero or close to 180 degrees, indicating turbulence at these levels. In the stable layer, gravity waves are indicated by the generally 90 degree phase difference, particularly at the smaller wave numbers. Figure 6.44 gives the phase angle between $w'$ and $\theta'$ that comes from the nested grid LES during the time averaging period ending at 2140 UTC (1440 MST). This Figure has curves representing analysis levels within the plains boundary layer, with curves A, B, and C corresponding to the same levels A, B, and C in Figure 6.40. Figure 6.45 is the same plot for the two levels in the mountain boundary layer, where curves A and B are at the same analysis levels as curves D and E, respectively, of Figure 6.40. At the lowest level the phase angle is close to 0 degrees and the level in the middle of the plains boundary layer also has phase angles close to 0 degrees, except for at a few of the lower wave numbers. Curve C in Figure 6.44 gives significantly larger phase angles, even at the smaller wave numbers. This behavior indicates the increasing importance of gravity waves with height in the plains boundary layer. The lowest level curve shows only evidence of turbulence, while the middle level

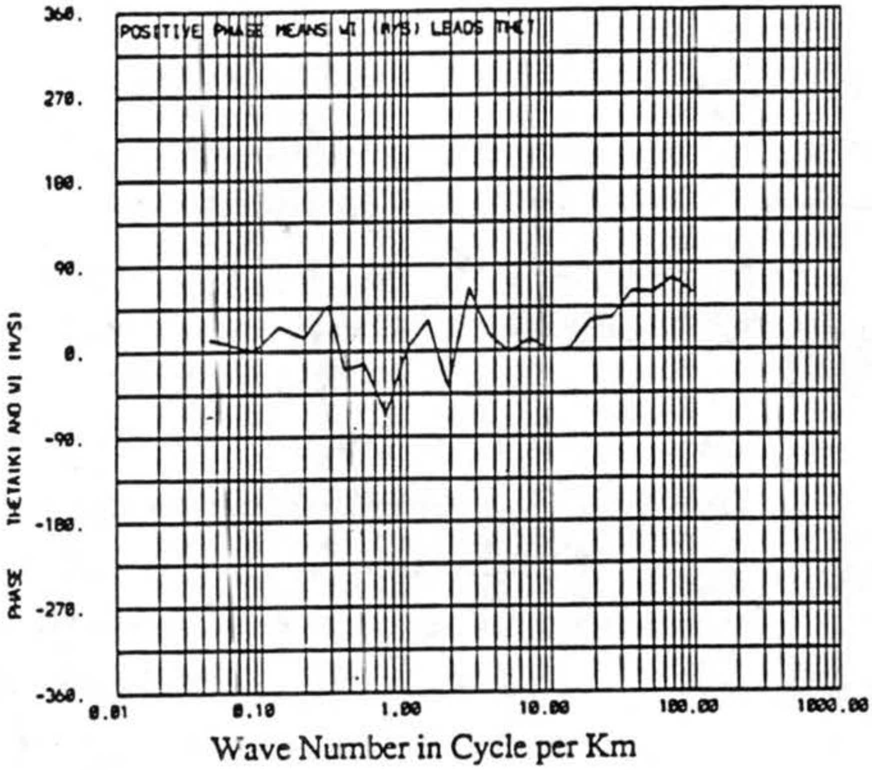


Figure 6.41: The phase difference between w and $\theta$ at 150 m AGL from aircraft data. From Lin (1988).

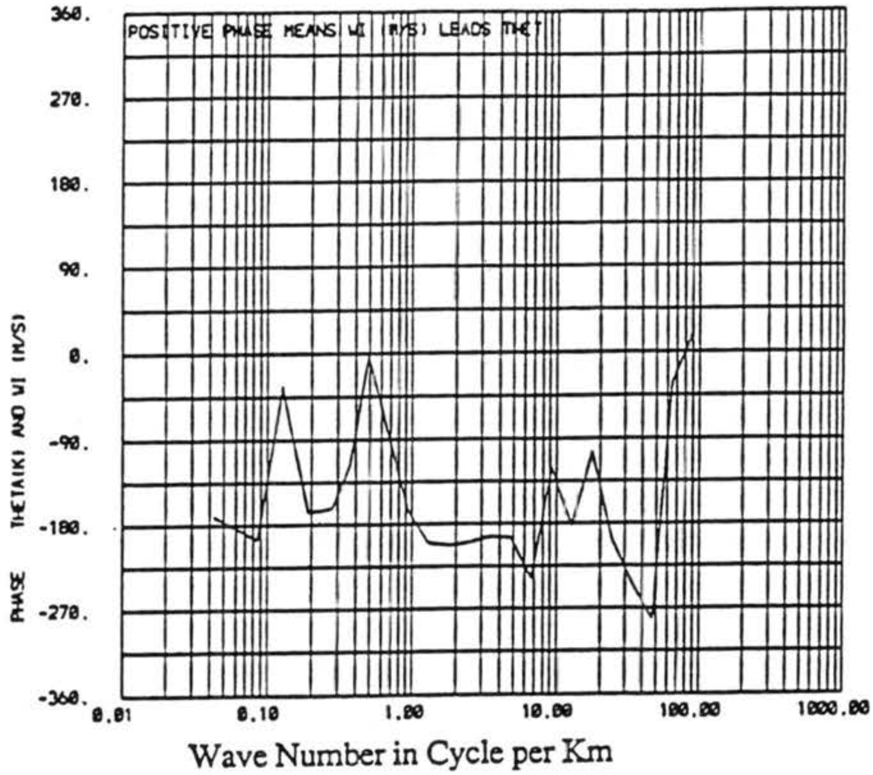


Figure 6.42: The phase difference between w and $\theta$ for the layer from 1900 to 2100 m AGL from aircraft data. From Lin (1988).

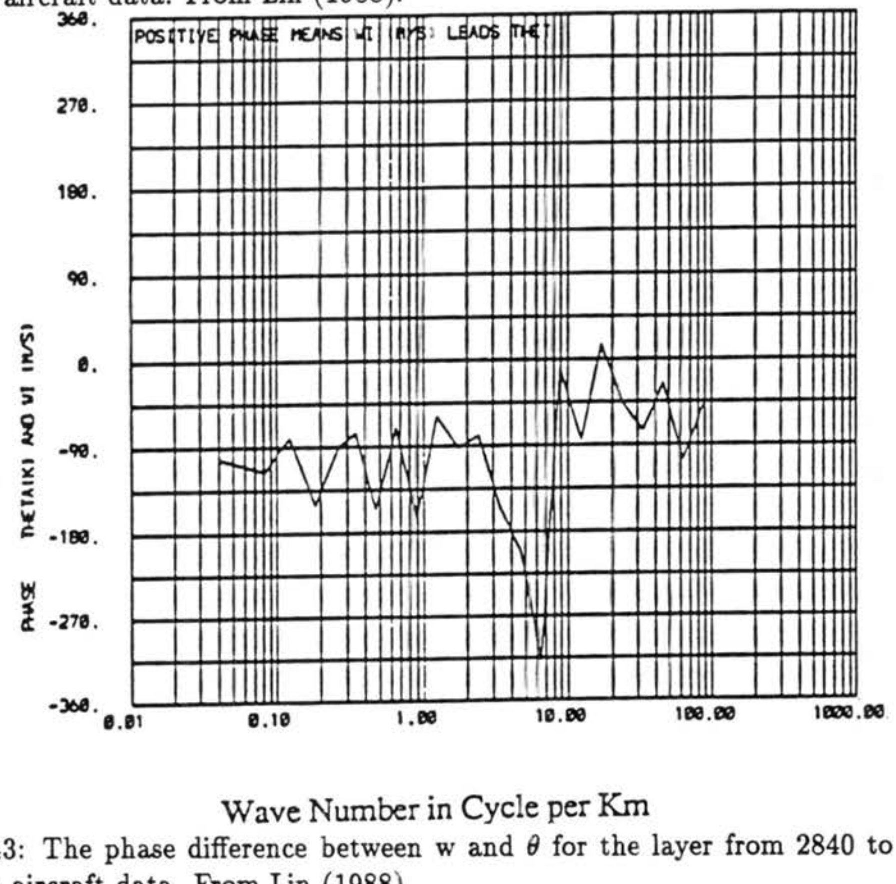


Figure 6.43: The phase difference between w and $\theta$ for the layer from 2840 to 3297 m AGL from aircraft data. From Lin (1988).

shows just a little influence from gravity waves at the longer wavelengths. The 90 degree phase angles of gravity waves are more common in the level at the top of the plains boundary layer and are predominant at the levels above the plains boundary layer.

### 6.3.2 Comparisons to the horizontally homogeneous LES

Comparison of the discrete energy spectra from the current nested grid LES to LES of the horizontally homogeneous boundary layer is limited because of the different scales that are represented. The horizontally homogeneous LES tend to have smaller grid spacing in the horizontal and can resolve features at higher wave numbers than the current simulation. On the other hand, the nested grid LES has a much larger domain and can represent much lower wavenumbers. Figure 6.46 is the spectra presented by Hadfield (1988) . Typical of traditional LES, the peak energy is only associated with the length scale of the large eddies which extend to the top of the boundary layer, approximately the characteristic wavelength of $1.5z_i$ found by Kaimal et al. (1976). His spectra do not have the energy peaks at low wave numbers that are associated with gravity waves in Figure 6.40 near the top of the boundary layer. He does not present spectra above the boundary layer top.

The spectra presented by Hadfield (1988) also have a steeper slope at higher wave numbers than expected. He explains that the steep slope is due to the larger value of the grid length scale constant used in his LES than suggested by Deardorff (1980) . Hadfield used this larger value to bring variances into better agreement with observations. The current nested grid LES uses the same value as Hadfield. Nieuwstadt et al. (1991), in their comparison of four different models for LES, also discuss the fact that the slope of the spectra at high wave numbers becomes steeper with higher values of the constant that is the ratio between mixing length and grid size. They show that, in the model with larger values of the constant, much of the variance at higher wave numbers is filtered out compared with the other models. However, none of the models were able to reproduce the $-\frac{2}{3}$ slope of the inertial subrange well.

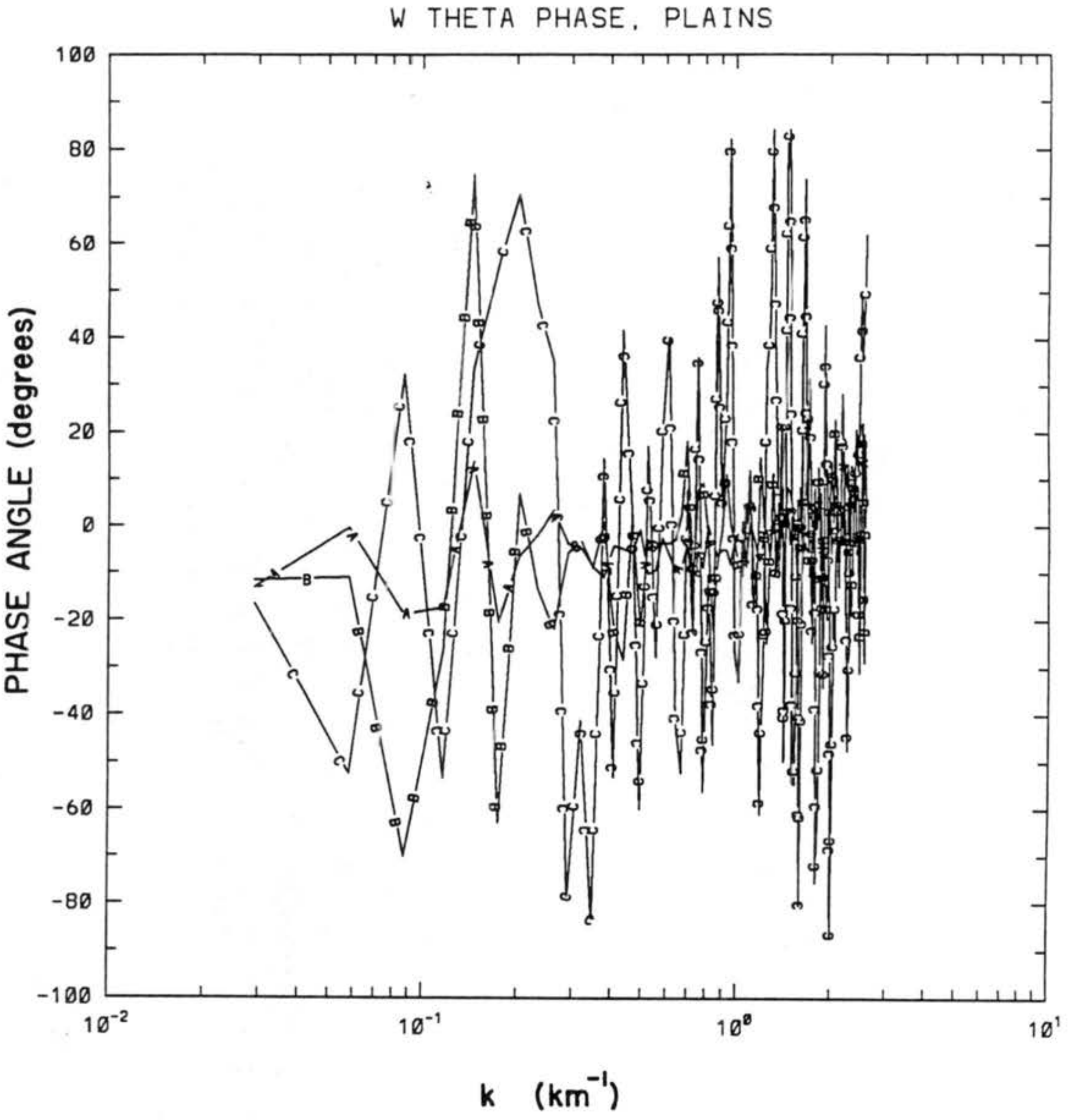


Figure 6.44: Phase angle between w and $\theta$ at three heights in the plains boundary layer. Heights represented by the curves are approximately 600 m AGL in curve A, 1700 m in curve B, and 2700 m in curve C.

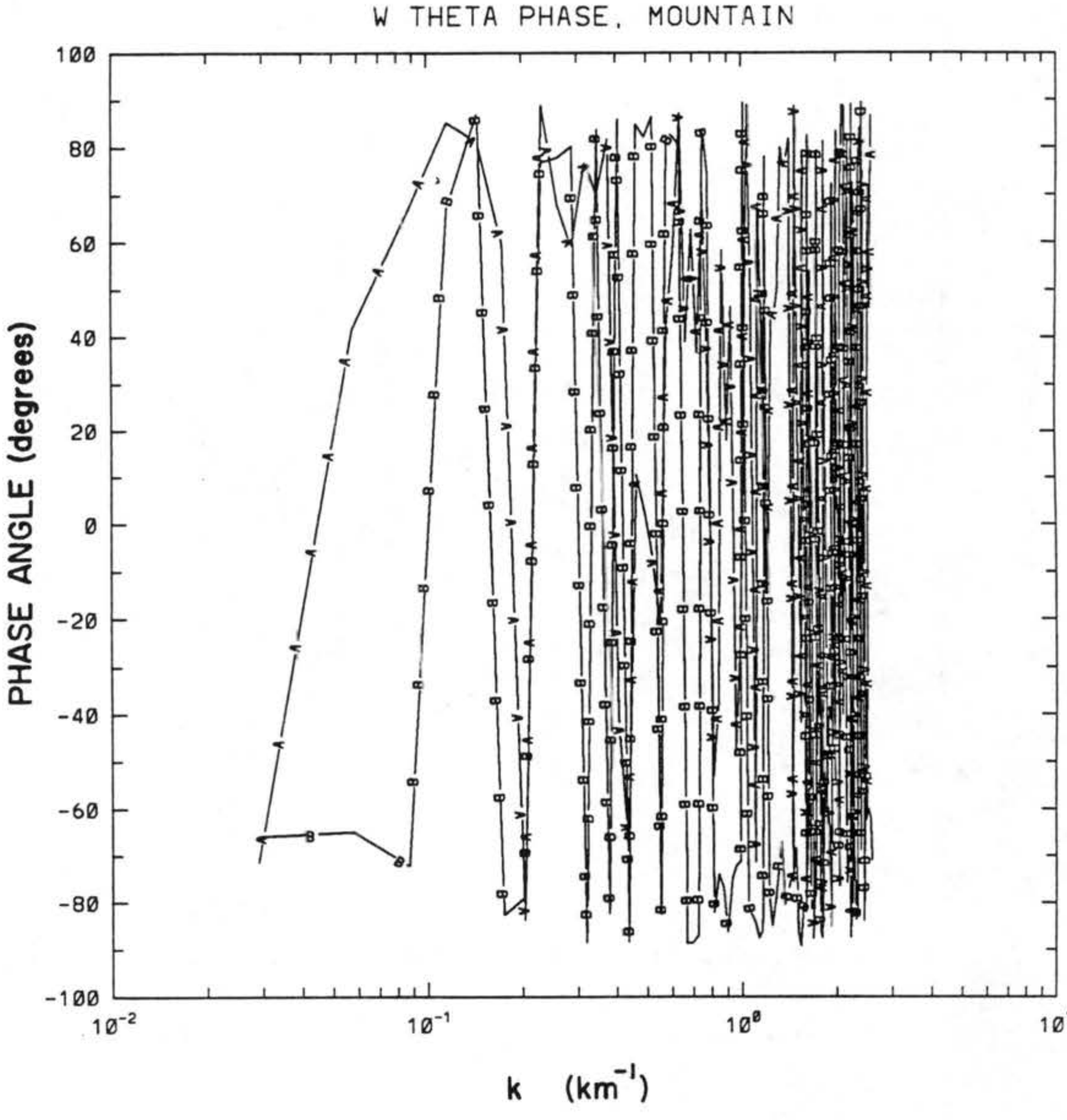


Figure 6.45: Phase angle between w and $\theta$ at two heights above the plains boundary layer. Heights represented by the curves are approximately 4200 m AGL in curve A and 5600 m in curve B.

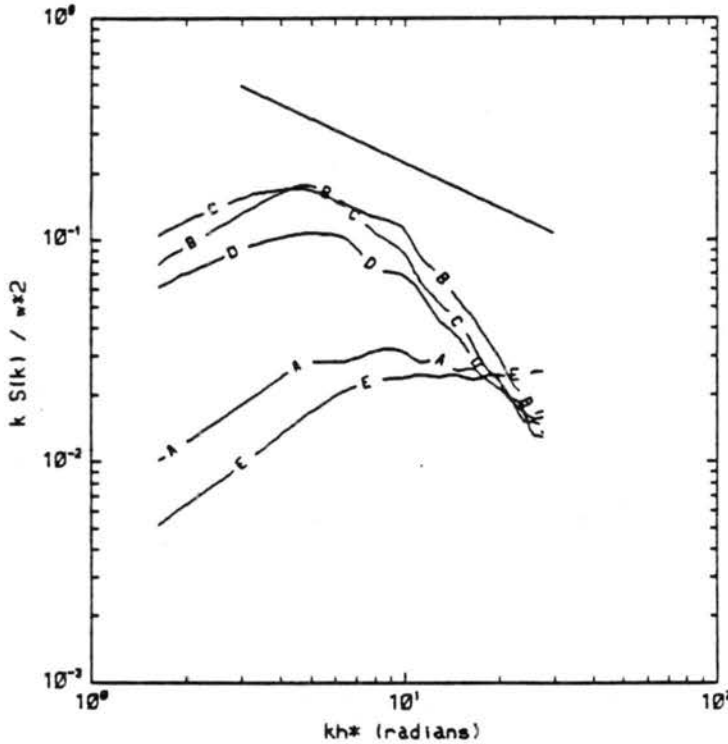


Figure 6.46: Horizontal power spectra of w from Hadfield's horizontally homogeneous LES plotted against dimensionless wavenumber $kh_*$. Curve A is at dimensionless height $0.05h_*$, curve B is at $0.25h_*$, curve C is at $0.50h_*$, curve D is at $0.75h_*$, and curve E is at $1.00h_*$. The straight solid lines have inertial subrange slope of $-\frac{2}{3}$. From Hadfield (1988).

## Chapter 7

# CONCLUDING REMARKS

## 7.1 Summary

This study departs from the traditional use of the LES that investigates the horizontally homogeneous, convective boundary layer and instead uses LES in a new application. The RAMS model is used to nest a LES within larger grids to model the horizontally non-homogeneous, convective, and sheared boundary layer. The LES applied in this manner has been used for a 'case study' of an observed atmospheric boundary layer on the Colorado High Plains, east of the Front Range of the Rocky Mountains. This 'case study' is intended to reproduce the atmospheric boundary layer on 22 June 1984, a day of observation during the Phoenix II experiment.

To verify the ability of the nested grid LES to realistically simulate this day, comparisons are made between the nested grid LES and Phoenix II radar and aircraft observations. Although the model is not expected to simulate each realization of the large eddies, its representation of their ensemble average is generally good. The model captures the evolution of the atmospheric boundary layer reasonably well. The expected warming and growth of the boundary layer due to heating from the surface and the presence of the large eddies and their structure are captured.

More importantly, the model is able to reproduce the influences of the mountain barrier to the west of the Phoenix II study area. The thermally-induced mountain-plains circulation contributes to the vertical shear of the horizontal winds. As a result of this wind shear, the boundary layer which develops over the elevated terrain advects eastward over the separate plains boundary layer. It is significant that the plains boundary layer of the nested grid LES has a poorly defined capping inversion, as found in the observations, having a relatively weak temperature gradient and variable depth in the horizontal. The model is also able to predict gravity waves due to the presence of the mountain obstacle and due to the convection that develops in the mountain boundary layer.

There are some noteworthy differences between the nested grid LES results and the Phoenix II radar observations. The profiles of turbulence statistics for the nested grid LES are more uniform through the afternoon while the profiles from radar observations are more variable. This is because the LES has a larger averaging area and better approximates an ensemble mean. At the same time, the LES has a deeper domain that can capture the influences of the mountains above the plains boundary layer. Other differences, related to the v-component of the wind, arise due to the lack of realistic topography in the model's y-direction and the inability of the model to capture synoptic scale atmospheric influences.

The results of the nested grid LES are also compared to typical LES of the horizontally homogeneous, convective boundary layer in order to assess the influence of the above phenomena associated with the mountain barrier on the turbulence statistics. The mesoscale circulation maintains strong vertical wind shear due to the presence of strong westerlies aloft and a vigorous easterly upslope flow. The prominence of the simulated vertical shear of the horizontal winds is manifested in the unusually strong maximum of the u-velocity variance near the top of the plains boundary layer. And the negative momentum flux through the depth of the plains boundary layer transports the higher momentum air downward.

The effects of the advection of the mountain boundary layer and the elevated, nearly neutral layer above the top of the plains boundary layer can be seen in the vertical profiles of many of the turbulence statistics. There is a second local minimum in heat flux at the top of this layer, which in some averaging periods is even more negative than at the top of the plains boundary layer. The horizontal velocity variances have second local maxima associated with the elevated neutral layer while vertical velocity variances are higher than are found in typical stable layers above horizontally homogeneous boundary layers. The skewness profiles also have unexpected relative maxima in this layer.

The weak and poorly defined capping inversion over the plains boundary layer leads to easier penetration of thermals into the stable layer. As a result, the vertical velocity variance profiles for the Phoenix II observations and the nested grid LES differ in an important way from the profiles of horizontally homogeneous boundary layers. Vertical velocity variance on 22 June does not decrease toward zero at the top of the plains boundary layer, without a strongly stable layer capping it. Also, entrainment produces relatively less negative heat flux at that height and it is not surprising that the most negative heat flux is associated with the much stronger inversion higher in the atmosphere on 22 June. The variance of potential temperature in horizontally homogeneous boundary layers is known to be large at the boundary layer top, especially if the capping inversion is strong. In the present case, the maximum in potential temperature variance is associated with the stronger inversion over the mountain boundary layer, with a smaller local maximum at the plains boundary layer top.

The presence of gravity waves on 22 June 1984 also makes this day different from the purely convective boundary layer. The spectral analysis shows the effect of gravity waves most effectively. In the layers above the plains boundary layer, the gravity waves lead to peak energy at longer wavelengths than expected from the horizontally homogeneous boundary layer. These wavelengths are typical of gravity waves and are longer than the characteristic scale of the large eddies. Spectra within the plains boundary layer have their peaks at the size of the large turbulent eddies but have increased energy at gravity wave wavelengths compared to spectra for horizontally homogeneous boundary layers. The cross spectral analysis shows that the phase angle difference between $w'$ and $\theta'$ is consistent with gravity waves and confirms the increasing influence of gravity waves with height.

## 7.2 Conclusions

The following conclusions can be drawn from this study:

- The use of the Large Eddy Simulation (LES) has successfully been extended to perform a case study by nesting a LES grid within larger grids that can model mesoscale circulations.

- The nested grid LES reasonably recreates the Phoenix II radar and aircraft observations for 22 June 1984. The model produces results in three spatial dimensions and time, which aircraft data cannot give, and can investigate larger horizontal and vertical extents of the atmosphere than the radar can observe. Thus the model can contribute insights to the observational study.
- This study has shown that atmospheric boundary layer east of the Colorado Rockies in the area of the Phoenix II experiment on 22 June 1984 is quite different from a horizontally homogeneous convective boundary layer. The proximity of a mountain barrier has been shown to influence the boundary layer of the Colorado High Plains.
- The flow over the Rocky Mountains and the thermally-driven slope flow are found to influence the atmospheric boundary layer over the Colorado High Plains by contributing to the vertical shear of the horizontal winds.
- As a consequence of the wind shear, the boundary layer that develops over the mountains is advected eastward over the top of the plains boundary layer. This layer is marked by a mixture of gravity waves and turbulence and is atypical of a purely convective boundary layer.
- While the mountain boundary layer advects eastward above the plains boundary layer, the capping inversion just below it and at the top of the plains boundary layer is weak and poorly defined compared to the inversions capping previously studied purely convective boundary layers.
- Gravity waves, triggered by the flow over the Rocky Mountain barrier and by convection in the mountain boundary layer, also influence the atmosphere above the Colorado High Plains.
- The vertical shear of the horizontal winds leads to increased u-velocity variance near the top of the plains boundary layer and negative momentum flux through the depth of the plains boundary layer.

- An additional local minimum in heat flux and second local maxima in the horizontal velocity variances and the skewness profiles are found in the nearly neutral layer above the plains boundary layer, and are related to the advection of the mountain boundary layer.

- The lack of a strong capping inversion allows larger vertical velocity variances than expected from a purely convective boundary layer at the top of the plains boundary layer. A second, and sometimes stronger, local minimum in heat flux is found at the base of the strong inversion that caps the mountain boundary layer.

- The energy spectra for the atmosphere above the Colorado High Plains is found to be influenced by the gravity waves associated with the mountain barrier and the convection within the mountain boundary layer. Greater energy is found at longer wavelengths compared to the horizontally homogeneous boundary layer, particularly at the heights of the plains boundary layer top and above. The phase spectrum for $w'$ and $\theta'$ also shows the important influence of the gravity waves that increases with height.

### 7.3 Suggestions for Further Research

Because this study is the first to use a LES nested within larger grids that can simulate mesoscale scale flows, there are many possibilities for continued application of this method of research. If computer resources allow it, a good first step would be to enlarge the extent of the domain in the y-direction. The number of y-direction grid points in the present study, in retrospect, is large enough to allow the turbulence to be three dimensional but is barely large enough to contain one or two of the large eddies. It would be better to be able to capture a number of eddies in the north-south extent of the domain. With a significantly larger domain in the y-direction, the cyclic boundary conditions will no longer be needed and realistic topography can be used in that direction as well. This should facilitate a better representation of the v-component of the winds.

This study has shown that the atmospheric boundary layer over the Colorado High Plains is distinctly affected by the Rocky Mountains to the west. It seems logical that other areas in proximity to mountain barriers and other topographic inhomogeneities (such as coastlines where sea breezes develop) will also experience the same sorts of phenomena. Further case studies could confirm this hypothesis.

The current case study investigated one particular day near the summer solstice when there was strong solar heating and wind shear. The influences of the mountain barrier are the result of this solar heating and wind shear and may be reduced under conditions where solar heating is reduced or wind shear is reduced or reversed. This may explain why other observational studies in this area and reported in Young (1988) and Lenschow (1970) did not find significant differences from the horizontally homogeneous boundary layer. Phoenix I data studied by Young (1988) were collected in September and aircraft data investigated by Lenschow (1970) were collected in April. A series of simulations investigating the role of the mountain barrier in different seasons would be enlightening.

Other sensitivity runs can also be made to study areas upwind of the mountain barrier. Many different possibilities exist to test the influence of surface characteristics. Surface characteristics, such as albedo, soil temperature, and soil moisture, will affect the thermally-induced mountain-plains circulation and may change the extent of the influence of the mountain barrier.

Finally, the results of this study and any of the research suggested in this section can be used to improve the understanding and prediction of the atmospheric boundary layer. Two applications come to mind. The first is that the results of this study can be used to improve parameterizations of the atmospheric boundary layer in larger scale models that include areas in proximity to mountains. At the least the results can be used to recognize the conditions under which the current parameterizations, that assume a horizontally homogeneous boundary layer, have deficiencies.

The second application is in the area of dispersion prediction. The results of the current study can be combined with a dispersion model to investigate the transport and diffusion properties over the Colorado High Plains on 22 June 1984. Some studies have already used LES for dispersion prediction. Use of the nested grids for areas affected by mountain barriers will allow for further case studies and contribute to more realistic predictions for those areas.

## REFERENCES


Abbs, D. J. and R. A. Pielke, 1986: Thermally forced surface flow and convergence patterns over northeast colorado. *Mon. Wea. Rev.*, **114**, 2281—2296.

Arritt, R. W., 1985: *Numerical studies of thermally and mechanically forced circulations over complex terrain.* PhD thesis, Colorado State University, Fort Collins, CO 80523, 193.

Arritt, R. W. and G. S. Young, 1990: Elevated stable layers generated by mesoscale boundary-layer dynamics over complex terrain. In *Preprints of the Fifth Conference on Mountain Meteorology*, June, American Meteorological Society, American Meteorological Society, Boulder, CO, 114—117.

Banta, R. M., 1984: Daytime boundary-layer evolution over mountainous terrain. part i: Observations of the dry circulations. *Mon. Wea. Rev.*, **112**, 340—356.

Banta, R. M. and W. R. Cotton, 1981: An analysis of the structure of local wind systems in a broad mountain basin. *J. Appl. Meteor.*, **20**, 1255—1266.

Bossert, J. E., 1990: *Regional-scale flows in complex terrain: An observational and numerical investigation.* PhD thesis, Colorado State University, Fort Collins, CO, 254.

Businger, J. A., J. C. Wyngaard, Y. Izumi, and E. F. Bradley, 1971: Flux-profile relationships in the atmospheric surface layer. *J. Atmos. Sci.*, **28**, 181—189.

Caughey, S. J., 1982: Observed characteristics of the atmospheric boundary layer. In *Atmospheric Turbulence and Air Pollution Modeling*, Nieuwstadt, F. T. M. and H. van Dop, Editors, Reidel, Dordrecht, 107—158.

Caughey, S. J. and S. G. Palmer, 1979: Some aspects of turbulence structure through the depth of the convective boundary layer. *Quart. J. Roy. Meteor. Soc.*, **105**, 811—827.

Chen, C. and W. R. Cotton, 1983: A one-dimensional simulation of the stratocumulus-capped mixed layer. *Boundary-Layer Meteor.*, **25**, 289—321.

Clark, R. H., A. J. Dyer, R. P. Brook, D. G. Reid, and A. J. Troup, 1971: The wangara experiment: Boundary layer data. Tech. Pap. 19, Dir, Meteor. Phys., CSIRO, Australia, 316.

Clark, T. L., 1977: A small-scale dynamic model using a terrain-following coordinate transformation. *J. Comput. Phys.*, **24**, 186—215.

Clark, T. L. and R. D. Farley, 1984: Severe downslope windstorm calculations in two and three spatial dimensions using anelastic interactive grid nesting: A possible mechanism for gustiness. *J. Atmos. Sci.*, **41**, 329—350.

Clark, T. L., T. Hauf, and J. P. Kuettner, 1986: Convectively forced internal gravity waves: Results from two- dimensional numerical experiments. *Quart. J. Roy. Meteor. Soc.*, **112**, 899—925.

Cotton, W. R. and R. A. Anthes, 1990: *Storm and Cloud Dynamics*, volume 44 of *International Geophysics Series*. Academic Press, San Diego, 883.

Cotton, W. R., R. L. George, and K. R. Knupp, 1982: An intense, quasi-steady thunderstorm over mountainous terrain. part i: Evolution of the storm-initiating mesoscale circulation. *J. Atmos. Sci.*, **39**, 328—342.

Cram, J. M., R. A. Pielke, and W. R. Cotton, 1992: Numerical simulation and analysis of a prefrontal squall line. part i: Observations and basic simulation results. *J. Atmos. Sci.*, **49**, 189—208.

Deardorff, J. W., 1970: Convective velocity and temperature scales for the unstable planetary boundary layer and for rayleigh convection. *J. Atmos. Sci.*, **27**, 1211—1213.

Deardorff, J. W., 1972: Numerical investigation of neutral and unstable planetary boundary layers. *J. Atmos. Sci.*, **29**, 91—115.

Deardorff, J. W., 1974a: Three-dimensional numerical study of the height and mean structure of a heated planetary boundary layer. *Boundary-Layer Meteor.*, **7**, 81—106.

Deardorff, J. W., 1974b: Three-dimensional numerical study of turbulence in an entraining mixed layer. *Boundary-Layer Meteor.*, **7**, 199—226.

Deardorff, J. W., 1980: Stratocumulus-capped mixed layers derived from a three-dimensional model. *Boundary-Layer Meteor.*, **18**, 495—527.

Deardorff, J. W. and G. E. Willis, 1985: Further results from a laboratory model of the convective planetary boundary layer. *Boundary-Layer Meteor.*, **32**, 205—236.

Deardorff, J. W., G. E. Willis, and D. K. Lilly, 1969: Laboratory investigation of non-steady penetrative convection. *J. Fluid Mech.*, **35**, 7—31.

Dirks, R., 1969: *A theoretical investigation of convective patterns in the lee of the Colorado Rockies.* PhD thesis, Colorado State University, Fort Collins, CO, 122.

Droegemeier, K. K. and R. B. Wilhelmson, 1985: Three dimensional numerical modeling of convection produced by interacting thunderstorm outflows. part i: Control simulation and low-level moisture variations. *J. Atmos. Sci.*, **42**, 2381—2403.

Grant, A. L. M. and P. J. Mason, 1990: Observations of boundary-layer structure over complex terrain. *Quart. J. Roy. Meteor. Soc.*, **116**, 159—186.

Hadfield, M. G., 1988: *The response of the Atmospheric convective boundary layer to surface inhomgeneities.* PhD thesis, Colorado State University, Fort Collins, CO, 401.

Hadfield, M. G., W. R. Cotton, and R. A. Pielke, 1991: Large-eddy simulations of thermally forced circulations in the convective boundary layer. part i: A small-scale circulation with zero wind. *Boundary-Layer Meteor.*, **57**, 79—114.

Hadfield, M. G., W. R. Cotton, and R. A. Pielke, 1992: Large-eddy simulations of thermally forced circulations in the convective boundary layer. part ii: The effect of changes in wavelength and wind speed. *Boundary-Layer Meteor.*, **58**, 307—327.

Hechtel, L. M. and R. B. Moeng, C. H. ans Stull, 1990: The effects of nonhomogeneous surface fluxes on the convective boundary layer: A case study using large-eddy simulation. *J. Atmos. Sci.*, **47**, 1721—1741.

Helfand, H. M. and J. C. Labraga, 1988: Design of a nonsingular level 2.5 second-order closure model for the prediction of atmospheric turbulence. *J. Atmos. Sci.*, **45**, 113—132.

Kaimal, J. C., R. A. Eversole, D. H. Lenschow, B. B. Stankov, P. H. Kahn, and J. A. Businger, 1982: Spectral characteristics of the convective boundary layer over uneven terrain. *J. Atmos. Sci.*, **39**, 1098—1114.

Kaimal, J. C., J. C. Wyngaard, D. A. Haugen, O. R. Cote, and Y. Izumi, 1976: Turbulence structure in the convective boundary layer. *J. Atmos. Sci.*, **33**, 2152—2169.

Krettenauer, K. and U. Schumann, 1992: Numerical simulation of turbulent convection over wavy terrain. *J. Fluid Mech.*, **237**, 261—299.

Kuettner, J. P., P. A. Hildebrand, and T. L. Clark, 1987: Convection waves: Observations of gravity wave systems over convectively active boundary-layers. *Quart. J. Roy. Meteor. Soc.*, **113**, 445—468.

LeMone, M. A., 1990: Some observations of vertical velocity skewness in the convective boundary layer. *J. Atmos. Sci.*, **47**, 1163—1169.

Lenschow, D. H., 1970: Airplane measurements of planetary boundary layer structure. *J. Appl. Meteor.*, **9**, 874—884.

Lenschow, D. H., 1974: Model of the height variation of the turbulence kinetic energy budget in the unstable planetary boundary layer. *J. Atmos. Sci.*, **31**, 465—474.

Lenschow, D. H., J. C. Wyngaard, and W. T. Pennell, 1980: Mean-field and second-moment budgets in a baroclinic, convective boundary layer. *J. Atmos. Sci.*, **37**, 1313—1326.

Lilly, D. K. and P. J. Mason, 1990: A numerical simulation of an observed heated and sheared boundary layer with mesoscale forcing. In *Preprints of Symposium on Atmospheric Turbulence and Diffusion*, April, American Meteorological Society, American Meteorological Society, Roskilde, Denmark, 258—261.

Lilly, D. K. and J. M. Schneider, 1990: Dual doppler measurement of momentum flux: Results from the phoenix ii study of the convective boundary layer. In *Preprints of Ninth Symposium on Turbulence and Diffusion*, April, American Meteorological Society, American Meteorological Society, Roskilde, Denmark, 98—101.

Lin, J.-J., 1988: Spectral and energy budget analysis of the phoenix ii aircraft data. Master's thesis, University of Oklahoma, Norman, OK, 59.

Louis, J. F., 1979: A parametric model of vertical eddy fluxes in the atmosphere. *Boundary-Layer Meteor.*, **17**, 187—202.

Mahrer, Y. and R. A. Pielke, 1977: A numerical study of airflow over irregular terrain. *Beitr. Phys. Atmos.*, **50**, 98—113.

Mason, P. J., 1989: Large-eddy simulation of the convective atmospheric boundary layer. *J. Atmos. Sci.*, **46**, 1492—1516.

Mason, P. J., 1992: Large-eddy simulation of dispersion in convective boundary layers with wind shear. *Atmos. Environ.*, **26A**, 1561—1571.

McBean, G. A., K. Bernhardt, S. Bodin, Z. Litynska, A. P. Van Ulden, and J. C. Wyngaard, 1979: The planetary boundary layer. Technical Note 165, World Meteorological Organization, Geneva, Switzerland, 79.

McNider, R. H., 1981: *Investigation of the impact of topographic circulations on the transport and dispersion of air pollutants.* PhD thesis, University of Virginia, Charlottesville, VA, 210.

Mellor, G. L. and T. Yamada, 1982: Development of a turbulence closure model for geophysical fluid problems. *Rev. Geophys. Space Phys.*, **20**, 851—875.

Moeng, C. H., 1984: A large-eddy-simulation model for the study of planetary boundary-layer turbulence. *J. Atmos. Sci.*, 41, 2052—2062.

Moeng, C. H. and R. Rotunno, 1990: Vertical-velocity skewness in the buoyancy-driven boundary layer. *J. Atmos. Sci.*, **47**, 1149—1162.

Moeng, C. H. and J. C. Wyngaard, 1984: Statistics of conservative scalars in the convective boundary layer. *J. Atmos. Sci.*, **41**, 3161—3169.

Moeng, C. H. and J. C. Wyngaard, 1988: Spectral analysis of large-eddy simulations of the convective boundary layer. *J. Atmos. Sci.*, **45**, 3573—3587.

Moeng, C. H. and J. C. Wyngaard, 1989: Evaluation of turbulent transport and dissipation closures in second-order modeling. *J. Atmos. Sci.*, **46**, 2311—2330.

Nieuwstadt, F. T. M. and R. A. Brost, 1986: The decay of convective turbulence. *J. Atmos. Sci.*, **43**, 532—546.

Nieuwstadt, F. T. M. and J. P. J. M. M. de Valk, 1987: A large-eddy simulation of bouyant and non-bouyant plume dispersion in the atmospheric boundary layer. *Atmos. Environ.*, **21**, 2573—2587.

Nieuwstadt, F. T. M., P. J. Mason, C. H. Moeng, and U. Schumann, 1991: Large-eddy simulation of the convective boundary layer: A comparison of four computer codes. In *Selected papers from the 8th Symposium on Turbulent Shear Flows*, Springer-Verlag.

Pielke, R. A., W. R. Cotton, R. L. Walko, C. J. Tremback, M. E. Nicholls, M. D. Moran, D. A. Wesley, T. J. Lee, and J. H. Copeland, 1992: A comprehensive meteorological modeling system – rams. *Meteor. Atmos. Phys.* (accepted).

Schmidt, H. and U. Schumann, 1989: Coherent structure of the convective boundary layer derived from large-eddy simulations. *J. Fluid Mech.*, **200**, 511—562.

Schneider, J. M., 1991: *Dual doppler measurement of a sheared, convective boundary layer.* PhD thesis, The University of Oklahoma, Norman, OK, 134.

Schneider, J. M., A. Lunsford, T. Gal-Chen, and D. K. Lilly, 1984: Phoenix ii - 1984 definitive atmospheric boundary layer program. University of Oklahoma, Norman OK.

Schumann, U., 1989: Large-eddy simulation of the convective slope layer. In *International conference on mountain meteorology and alpex*, June, German Aerospace research establishment, Oberpfaffenhofen, FRG, 125—126.

Schumann, U., 1990: Large-eddy simulation of the up-slope boundary layer. *Quart. J. Roy. Meteor. Soc.*, **116**, 637—670.

Schumann, U., T. Hauf, H. Holler, H. Schmidt, and H. Volkert, 1987: A mesoscale model for the simulation of turbulence, clouds and flow over mountains: Formulation and validation examples. *Beitr. Phys. Atmos.*, **60**, 413—446.

Stull, R. B., 1988: *An Introduction to Boundary Layer Meteorology.* Kluwer Academic Publishers, Boston, MA, 666.

Stull, R. B. and E. W. Eloranta, 1984: Boundary layer experiment 1983. *Bull. Amer. Meteor. Soc.*, **65**, 450—456.

Sykes, R. I. and D. S. Henn, 1989: Large-eddy simulation of turublent sheared convection. *J. Atmos. Sci.*, **46**, 1106—1118.

Telford, J. W. and J. Warner, 1964: Fluxes of heat and vapor in the lower atmosphere derived from aircraft observations. *J. Atmos. Sci.*, **21**, 539—548.

Toth, J. J. and R. H. Johnson, 1985: Summer surface flow characteristics over northeast colorado. *Mon. Wea. Rev.*, **113**, 1458—1469.

Tremback, C. J., 1990: *Numerical simulation of a mesoscale convective complex:Model developme Model development and numerical results.* PhD thesis, Colorado State University, Fort Collins, CO, 247.

Tremback, C. J. and R. Kessler, 1985: A surface temperature and moisture parameterization for use in mesoscale numerical models. In *Preprints, 7th Conference on Numerical Weather Prediction*, June, American Meteorological Society, American Meteorological Society, Montreal, 355—358.

Tripoli, G. J., 1986: *A numerical investigation of an orogenic mesoscale convective system.* PhD thesis, Colorado State University, Fort Collins, CO, 290.

Tripoli, G. J. and W. R. Cotton, 1980: A numerical investigation of several factors contributing to the observed variable intensity of deep convection over south florida. *J. Appl. Meteor.*, **19**, 1037—1063.

Tripoli, G. J. and W. R. Cotton, 1982: The colorado state university three-dimensional cloud/mesoscale model-1982. part i: General theoretical framework and sensitivity experiments. *J. Rech. Atmos.*, **16**, 185—220.

Tripoli, G. J. and W. R. Cotton, 1989: A numerical study of an observed orogenic mesoscale convective system. part i: Simulated genesis and comparison with observations. *Mon. Wea. Rev.*, **117**, 273—304.

Van Haren, L. and F. T. M. Nieuwstadt, 1989: The behavior of passive and buoyant plumes in a convective boundary layer, as simulated with a large-eddy model. *J. Appl. Meteor.*, **28**, 818—832.

Walko, R. L., W. R. Cotton, and R. A. Pielke, 1992: Large-eddy simulations of the effects of hilly terrain on the convective boundary layer. *Boundary-Layer Meteor.*, **58**, 133—150.

Wilczak, J. M. and T. W. Christian, 1990: case study of an orographically induced mesoscale vortex (denver cyclone). *Mon. Wea. Rev.*, **118**, 1082—1102.

Willis, G. E. and J. W. Deardorff, 1974: A laboratory model of the unstable planetary boundary layer. *J. Atmos. Sci.*, **31**, 1297—1307.

Wolyn, P. G., 1992: *Modeling and observational study of the daytime evolution east of the crest of the Colorado Rockies.* PhD thesis, Colorado State University, Fort Collins, CO, 255.

Wolyn, P. G. and T. B. McKee, 1990: A modeling and observational study of the diurnal evolution of the atmosphere east of a large mountain barrier. In *Preprints of the Fifth Conference on Mountain Meteorology*, June, American Meteorological Society, American Meteorological Society, Boulder, CO, 50—52.

Wyngaard, J. C., O. R. Cote, and Y. Izumi, 1971: Local free convection, similarity, and the budgets of shear stress and heat flux. *J. Atmos. Sci.*, **28**, 1171—1182.

Young, G. S., 1988: Turbulence structure of the convective boundary layer. part ii: Phoenix 78 aircraft observations of thermals and their environment. *J. Atmos. Sci.*, **45**, 727—735.

Young, S., 1986: *The dynamics of thermals and their contribution to mixed layer processes.* PhD thesis, Colorado State University, Fort Collins, CO, 292.